

Independent University, Bangladesh

The Use and Optimization of Plasmonic Nanostructures on Different Thin-Film Solar Cells for Enhancing Their Opto-electronic Performance- A Comparative Study

An undergraduate thesis submitted by

Rashid Ahmed Rifat

in consideration of the partial fulfillment for the requirements of the degree of

BACHELOR OF SCIENCE

in

ELECTRICAL AND ELECTRONIC ENGINEERING

Department of Electrical and Electronic Engineering

Summer 2019

DECLARATION

I do hereby solemnly declare that the research work presented in this undergraduate thesis has been carried out by me and has not been previously submitted to any other University/Institute/Organization for an academic qualification/certificate/diploma or degree.

_____

Rashid Ahmed Rifat

Student ID: 1520112

Date: 29 August 2019

APPROVAL

The project work report titled "**The Use of Plasmonic Nanostructures on Different Types of Thin-Film Solar Cells for Enhancing Their Opto-electronic Performance- A Comparative Study**" has been submitted by Rashid Ahmed Rifat (ID # 1520112) of Electrical and Electronic Engineering (BSc. in EEE), to the Department of Electrical & Electronic Engineering at Independent University Bangladesh, for the fulfillment of the requirements for the Degree of Bachelor of Science.

Dr. Mustafa Habib Chowdhury

Thesis Supervisor & Assistant Professor

Department of Electrical & Electronic Engineering

Independent University, Bangladesh.

ACKNOWLEDGEMENTS

"[All] praise is [due] to Allah, to whom belongs whatever is in the heavens and whatever is in the earth, and to Him belongs [all] praise in the Hereafter. And He is the Wise, the Acquainted."- [Al-Qur'an – Surah 34: 1]

All praises to the Almighty for the fruitful accomplishment of this thesis and making a dream come true for the author. Adding to that, thanks are also due to the following persons for their continuous support for the completion of the research and the thesis report.

Firstly, the author would like to express his thankfulness to his supervisor Dr. Mustafa Habib Chowdhury, Assistant Professor, Department of Electrical & Electronic Engineering, Independent University, Bangladesh, for his wisdom, patience, support, and for providing the opportunity to learn and work under his supervision as his research assistant for more three years. His supervision and support were the most vital possessions that led the accomplishment of this thesis. More importantly, his inspiration towards finding the truth about science has lead the author to conduct this research study in a more satisfying way.

Special thanks has to be extended to Dr. Khosru M. Salim, Professor, Department of Electrical and Electronic Engineering, Independent University, Bangladesh and Dr. M Abdur Razzak, Associate Professor, Department of Electrical and Electronic Engineering, Independent University, Bangladesh for their encouragement, lively discussions and for funding the author's research assistant salary without any hesitations. The author cannot express his gratitude enough in this regard.

The author would also like to thank the members of IUB Photonics Simulation Laboratory for their constant support and cooperation throughout the research.

Finally, the author proudly and fully acknowledges the great sacrifices, good wishes, moral support, mental support, fruitful advice, inspirations and encouragements from his family members, friends, faculty members-seniors and juniors of IUB during the research.

The Author

August 2019

Dhaka, Bangladesh

ABSTRACT

This study compares the response of thin-film silicon, gallium arsenide, cadmium telluride-cadmium sulfide and organic solar cells (OSCs) to the use of plasmonic metal nanoparticles for modifying their respective opto-electronic behavior and performance. Square arrays of silver nanoparticles were deposited at different inter-particle distances on top of the thin film solar cell substrates. The absorption of incident sunlight inside each solar cell form is investigated, and they were compared to the short circuit current density, open circuit voltage, the output power generated from each solar cell type and the fill factor calculations owing to the influence of the plasmonic nanoparticles. It is found that gallium-arsenide and cadmium telluride-cadmium sulfide show higher values than Silicon in the short circuit current generated, open circuit voltage, the fill-factor and the output power generated. Also, the optical absorption enhancement in the OSC was quite significant which gives further scope for research with such solar cell. These results show the influence of plasmonic metal nanoparticles to escalate the opto-electronic performance of thin-film solar cells is not restricted only to silicon substrates but extends to other commonly used semiconductor and organic substrates.

TABLE OF CONTENTS

Declaration ii

Approval iii

Acknowledgements iv

Abstract v

List of Figures ix

List of Tables xi

1. Chapter 1 Introduction 1

1.1 Background 1

1.2 Problem Statement 5

1.3 Objectives 7

1.4 Research Flowchart 8

1.5 Organization of this Report 9

2. Chapter 2 Literature Review 10

2.1 Solar Energy 10

2.2 The Greenhouse Effect 10

2.3 Properties of sunlight and its effects 13

2.4 Semiconductor Materials 19

2.5 Generation and Recombination of electron –holes pairs 24

2.6 Solar Cell Structures and Operation 30

2.7 Solar Cell Parameters 32

2.8 Photovoltaic Technologies 38

2.9 Nanostructured Solar Cells 45

2.10 Plasmonic Thin Film Solar Cells 47

2.11 Finite-Difference-Time-Domain (FDTD) Algorithm and Methodology 49

2.12 FDTD Solutions and DEVICE 51

3. Chapter 3 Fdtd Algorithm 52

3.1 History 52

3.2 Theory 53

3.3 Strengths of FDTD Algorithm 66

3.4 Weaknesses of FDTD Algorithm 67

4. Chapter 4 Research Methodology 69

4.1 Simulation Setup 69

4.2 Plasmonic Resonance for Silver (Ag) 70

4.3 Optical Absorption Enhancement 73

4.4 Short Circuit Current Density (J_{sc}) 75

4.5 Open Circuit Voltage (V_{OC}) 76

4.6 Output Power (P) 77

4.7 Fill Factor (FF) 77

4.8 Near Field Enhancement 77

5. Chapter 5 Results And Discussion 79

5.1 Optical Absorption Enhancement Analysis 79

5.2 Short Circuit Current Density (JSC) Analysis 86

5.3 Open Circuit Voltage (V_{OC}) Analysis 89

5.4 Output Power (P) Analysis 91

5.5 Efficiency Calculation 93

5.6 Fill Factor (FF) Analysis 94

5.7 Optical Near-Field Enhancement Analysis 96

6. Chapter 6 Conclusion & Future Work **100**

References **103**

LIST OF FIGURES

Figure 1. 1 Research Flowchart. 8
Figure 2. 1 Relationship of the rise in atmospheric carbon dioxide concentration 11
Figure 2. 2 Average surface temperature of the earth. 12
Figure 2. 3 The electromagnetic spectrum. 13
Figure 2. 4 Solar radiation at the surface of Earth. 15
Figure 2. 5 Absorption and scattering of incident sunlight in clear sky. 16
Figure 2. 6 The air mass. 17
Figure 2. 7 An easy method to determine the air mass is from the shadow of a vertical pole. 17
Figure 2. 8 Air Mass- AM0 and AM1.5. 18
Figure 2. 9 A section of the periodic table. 19
Figure 2. 10 Schematic illustration of covalent bonds in a silicon crystal lattice. 20
Figure 2. 11 Band gap diagram. 22
Figure 2. 12 Schematic of a silicon crystal lattice. 23
Figure 2. 13 The absorption coefficient, α, in a variety of semiconductor materials. 25
Figure 2. 14 Drawing of the photogeneration process. 28
Figure 2. 15 Scheme of the main recombination processes. 29
Figure 2. 16 An overview of the mechanism p-n junction. 30
Figure 2. 17 Cross-section of a typical solar cell. 31
Figure 2. 18 I-V curve of a solar cell showing the short-circuit current. 33
Figure 2. 19 I-V curve of a solar cell showing the open-circuit voltage. 34
Figure 2. 20 Graph of cell output current. 36
Figure 2. 21 Current voltage (IV) cure of a solar cell. 37
Figure 2. 22 Diagram of apparatus described by Becquerel (1839). 38
Figure 2. 23 Sample geometry used by Adams and Day (1876). 39
Figure 2. 24 Thin-film selenium demonstrated by Fritts in 1883. 39
Figure 2. 25 Early Grondahl-Geiger copper-cuprous oxide photovoltaic cell (circa 1927). 40
Figure 2. 26 Structure of the most efficient photovoltaic devices. 40
Figure 2. 27 Early silicon solar cell structure. 40
Figure 2. 28 Representation of a typical CdTe superstrate thin-film PV device. In this design, the layers of the device are put onto a glass “superstrate” that permits sunlight to go in. The sunlight passes through the glass and produces electrical current. 42

Figure 2. 29 Representation of a typical CIGS substrate thin-film photovoltaic device. 42
Figure 2. 30 Structure of a GaAs cell. 43
Figure 2. 31 Amorphous silicon (a-Si) is the non-crystalline form of silicon. 44
Figure 2. 32 Nanostructured solar cells. 46
Figure 2. 33 Different shapes of plasmonic nanostructures analyzed. 46
Figure 2. 34 Surface plasmon polariton generation. 47
Figure 2. 35 Interoperability of FDTD Solutions and DEVICE. 51
Figure 3. 1 Yee's unit space lattice cell. 54
Figure 3. 2 According to Yee algorithm E and H field components are separated. 55
Figure 3. 3 Assuming that field values can only vary in the z-direction. 57
Figure 3. 4 1-D FDTD Algorithm Flow Chart. 59
Figure 3. 5 Diagram of absolute boundary condition. 65
Figure 3. 6 PML Region. 66
Figure 4. 1 Plasmonic resonance analysis setup. 70
Figure 4. 2 Absorption, scattering and extinction spectra. 72
Figure 4. 4 Organic solar cell structure. 74
Figure 4. 3 Simulation Setup for the optical absorption enhancement analysis. 74
Figure 4. 5 Simulation setup for Jsc calculation (in silicon substrate). 76
Figure 4. 6 Setup for near-field enhancement analysis. 78
Figure 5. 1 Excel plot for Total Absorption Enhancement Factor. 80
Figure 5. 2 Wavelength-resolved optical absorption enhancement. 81
Figure 5. 3 Wavelength (um)-resolved optical absorption. 82
Figure 5. 4 Wavelength (nm)-resolved optical absorption enhancement. 83
Figure 5. 5 Wavelength (nm)-resolved optical absorption enhancement. 84
Figure 5. 6 Excel plot for the Jsc results. 88
Figure 5. 7 Excel lot for the Voc results. 90
Figure 5. 8 Excel plot for the output power results. 92
Figure 5. 9 Excel plot for the fill factor results. 94
Figure 5. 10 Near-field images at λ=460nm 96
Figure 5. 11 Near-field raw(unenhanced) images at λ=460nm. 97
Figure 5. 12 Near-field enhancement images λ=460nm, Pitch length 120nm. 99
Figure 5. 13 Near-field enhancement images λ=460nm, Pitch length 80nm 99

LIST OF TABLES

Table 2. 1 Properties of semiconductor types in silicon _____ 24

Table 5. 1 Total Optical absorption enhancement Factor _____ 79
Table 5.2 J_{SC} of the Ag nanoparticle array based solar cells for the entire solar spectrum __ 87
Table 5. 3 Open Circuit Voltage (V_{OC}) _____ 89
Table 5. 4 Output Power _____ 91
Table 5. 5 Efficiency Calculation _____ 93
Table 5. 6 Fill Factor _____ 94

CHAPTER 1
INTRODUCTION

1.1 Background

Energy demand is at its peak due to the exponential increase in the global population which was estimated to have reached more than 7 billion as of April 2019 [1]. According to International Energy Agency data from 1990 to 2008, the average energy consumption per person increased 10% while world population increased 27% [2]. With this rapid growth of population and the advancement of technology, the demand for energy is more than ever in the history of mankind. To a certain extent, the use of fossil fuels such as petroleum oil, coals and natural gases have come to the rescue in this regard and have allowed coping with the situation. However, the dependency on fossil fuels is now questionable due to certain factors. Firstly, these finite resources are constantly depleting with the exponential rise in demand and there are no prompt solutions to replenish them. Secondly, the extraction and the usage of fossil fuels have caused the adverse effects toward climate change around the globe which includes the immense rise of temperature of Earth known as global warming, the systematic degradation of the different ecosystems of the world and many more. That being said, it is high time that alternative energy resources be found to replace fossil fuels.

The need for sustainable and renewable “green” energy sources which are economically feasible to replace fossil fuels have never been greater. To achieve the goal, few “green” energy sources have already been discovered and worked on, among them– wind, thermal, water and solar are the most notable ones. It is to be noted that the abundant solar energy coming from the sunlight is the largest natural source of energy in the solar system. The technology used to harness this immense energy from the sun is known as solar cells or photovoltaic (PVs) cells [3]–[5]. PVs cell transforms solar energy harnessed from the largest star in the solar system into electrical energy. During the last decades, PVs cell has become one of the most promising renewable energy technologies because of its potential, with capacity of installation of PV panels approaching to 100 GW in 2018 and is probable that it will go on rising [6].

As the demand of energy is growing day by day, photovoltaic has a vital role to play in solving the climate change problem replacing the fossil fuels. But to compete with the fossil fuel technologies, the photovoltaic devices need to be efficient and feasible in terms of cost, energy, manufacturing and installation. Currently, crystalline silicon wafers based solar cells with thickness of 200-300 μm are dominating the solar cell market. On the other hand, materials and processing of the silicon wafers cost a large portion of the expenses. Around 40% of the total module cost is accounted for the crystalline silicon solar cells. Because of this drawback, over the past decade there has been a great deal of research on thin-film solar cells which have a mere thickness of 1-2 μm. Thin-film solar cells have developed as a means to lessen the price of material. They are made from a variety of semiconductors including amorphous and polycrystalline silicon, gallium arsenide, copper indium diselenide, cadmium telluride, hybrid lead halide perovskites, as well as multi-layered and heterojunction organic semiconductors. However, as the thickness of the semiconductor is decreased, their absorbance of near-band gap light is ineffective and reduces near the band gap region. This means that the efficiency of the thin-film solar cells is lower than that of the conventional silicon solar cells. For this purpose, the compromise has to be made for the absorbance of solar energy and the narrower band gap semiconductor. Therefore, novel designs for structuring thin-film solar cells so that much of the light is trapped inside, in order to increase the absorption, are really important.

Earlier studies have investigated few light trapping techniques which include pyramidal surface texture [7] etched into the surface. However, for thin-film solar cells surface texturing with these dimensions is not suitable. In addition to that, it is possible to achieve light to be trapped by forming a wavelength-scale texture surface on the substrate and then putting the thin-film solar cell on top, in this way a significant increase in current generation have been achieved [8], [9] But then again, a rough semiconductor surface results increased surface recombination due to the larger surface area. With all these limitations in mind, research has always been focused on developing novel materials and nanostructures with unique properties of which would be beneficial in enhancing the optical and electrical activities of the PV cell. Recently, the use of Raman scattering from noble metal nanoparticles excited at their surface plasmons (SPs) resonance [10] has been regarded as an efficient way to allow light to be trapped into the active layer of a thin-film solar cell and has drawn significant amount of attention in the scientific community. Metals, therefore, have been, and are currently studied extensively as a part of that research to identify and optimize properties that

would assist in that goal [4], [11]–[14].

Plasmonic resonance is a phenomenon of plasmonic metals (mentioned earlier) which is used by the plasmonic solar cells to increase the optical absorption of thin film solar cells. The focus of this thesis is on plasmonic thin-film solar cells made of amorphous silicon as well other substrates like gallium arsenide, cadmium telluride- cadmium sulfide and OSC. A group of researchers from IUB Photonics Simulation Laboratory studied and had done extensive research on the effect of plasmonic nanoparticles on solar cells with numerous configurations [15]–[24]. Thorough research and studies have been done by previous researchers in the initial work using plasmonic structures to improve the absorption of light of photovoltaic devices with Au or Ag nanoparticles [15], [25], [26] and nanograting [27] have been introduced into the front side of the solar cells [25], [26], [28]. Adding to that, recently it has also been investigated to enhance the light trapping efficiency by using different shapes of nanoparticles [19], different rows and columns of nanopheres [18], nanoparticles embedded within the substrate [20] , hybrid nanoparticles [23], special bow-tie structures [22], and core shell structures. Moreover, different combinations of embedded metal nanostructures to trap more light into thin-film solar cell has been comprehensively explored, e.g., with nucleated silver nanoparticles embedded at back side of amorphous silicon cells [29], using gold paired-strips [30] and combination of surface texture with embedded metal nanoparticles was also designed to trap light [31].

While the use of plasmonic nanostructures has been produced and analyzed over the course of the last decade or so, none of these studies have proceeded comprehensively beyond the initial stages of the analysis, namely the design, fabrication and the manipulation of the plasmonic characteristics of the aforementioned nanostructures. This thesis, however, aims to provide a systematic analysis of the use of plasmonic metal nanoparticles, namely silver (Ag), arranged periodically over thin-film solar cells made with substrates of amorphous silicon (Si), gallium arsenide (GaAs), cadmium telluride-cadmium sulfide (CdTe-CdS) and OSC (P3HT:PCBM) substrates. This thesis explores how the physical parameters of the nanoparticles can be optimized to induce optical and electrical enhancements generated from the different types of solar cells. Through this thesis, the relationship between the physical parameters of the metal nanoparticles and the opto-electronic performance of the different photovoltaic substrates will be compared. One of the goals of this thesis is to investigate whether silicon is the only semiconductor substrate that is affected by the plasmonic metal nanoparticles or whether this effect can be replicated in other commonly used semiconductor

substrates such as GaAs and CdTe-CdS as well OSCs. An extensive correlation between the optical and electrical parameters will be demonstrated in this thesis, and then the extent to which the optical enhancement translates into electrical energy conversion within the cell will be provided with detailed analysis. The research methodology has been explained in the upcoming sections.

1.2 Problem Statement

Although being one of the most convenient renewable energy technologies, several factors affect a solar cell's conversion efficiency value, including its:

- reflectance efficiency,
- thermodynamic efficiency,
- charge-carrier separation efficiency,
- charge-carrier collection efficiency and
- conduction efficiency values. [32]

In physics, the term Shockley–Queisser limit, also known as the detailed balance limit, Shockley Queisser Efficiency Limit or SQ Limit, denotes to the maximum theoretical efficiency of a single p-n junction solar cell which uses to gather power from the cell. This limit was first calculated by William Shockley and Hans-Joachim Queisser at Shockley Semiconductor in 1961, giving a maximum efficiency of 30% at 1.1 eV [33].

With the aim to mitigate the problem of the efficiency, the parameters of the solar cells needed to be optimized. Over the last decade, research has been focused on thin-film solar cells to find ways to optimize the parameters to achieve the goal. However, the reduced materials of the thin-film solar cells also mean that less amount of semiconductor material is exposed to the incident light from the sun, and along with reflections from the surface and bottom boundaries, these results in a lower optical absorption of the radiation as well as low opto-electronic current. As mentioned earlier, plasmonic nanoparticles coupled with thin-film PV cells have been demonstrated to enhance this absorption significantly. The plasmonic resonance characteristics of certain metals such as silver, gold and aluminum allow the incident radiation to be focused around and towards the cell itself at certain resonant frequencies, and these results in the aforementioned enhancement.

On the other hand, previously there has not been any extensive study made on how variations in the physical properties of the nanoparticles spread periodically over different types of substrates of PV cells affect the opto-electronic enhancement and how these variations can be manipulated to identify which exact parameters provide the most optimal

enhancement of the cell in terms of optical and electrical parameters.

So as to achieve these results, this study analyzes the correlation of several physical parameters, namely diameter of nanoparticles, pitch (side-side period length) of the nanoparticles, and the different types of substrates from which the solar cells are made of. Through this study, the correlation will demonstrate which parameters provide the most optimum optical absorption enhancement, and a translation of this enhancement into electrical energy generated by the modified solar cells will also be shown.

1.3 Objectives

The motive of this thesis is to provide a systematic analysis of the optimization of few physical parameters of plasmonic nanoparticles deposited periodically over different types of thin-film PV cell namely- silicon(Si), gallium arsenide (GaAs) and cadmium telluride-cadmium sulfide (CdTe-CdS) and organic solar cells (OSC), to enhance the energy conversion efficiency of the cell, and also to make a comparison between the different types of solar cells in terms of their optical and electrical enhancement. The entire analysis will be done using the solvers FDTD Solutions and DEVICE (CHARGE Solver).

The main objectives of the thesis are summarized below:

- To identify which type of solar cell substrates give significant improvement in the opto-electronic performance due to the effect of plasmonic nanoparticles placed on top of the solar cell substrates.
- To analyze the improvement in optical absorption with respect to periodically placed silver (Ag) nanoparticles with different pitch length (side to side distance between each nanoparticle).
- To analyze the extent to which this optical optical absorption enhancement translates to improvement in electrical energy generated within the cell.
- To understand the variation in electrical enhancement with respect to the length of period of the nanoparticles through different electrical parameters.
- To prove that the effect of plasmonic particle is not limited only to conventional silicon substrate solar cell but its effect also applies to other semiconductor and OSCs.
- To establish and clarify the conclusions reached with optical optical near-field enhancement images.

1.4 Research Flowchart

The processes implemented to perform this thesis are demonstrated step-by-step in the flowchart illustrated below in Figure 1.1.

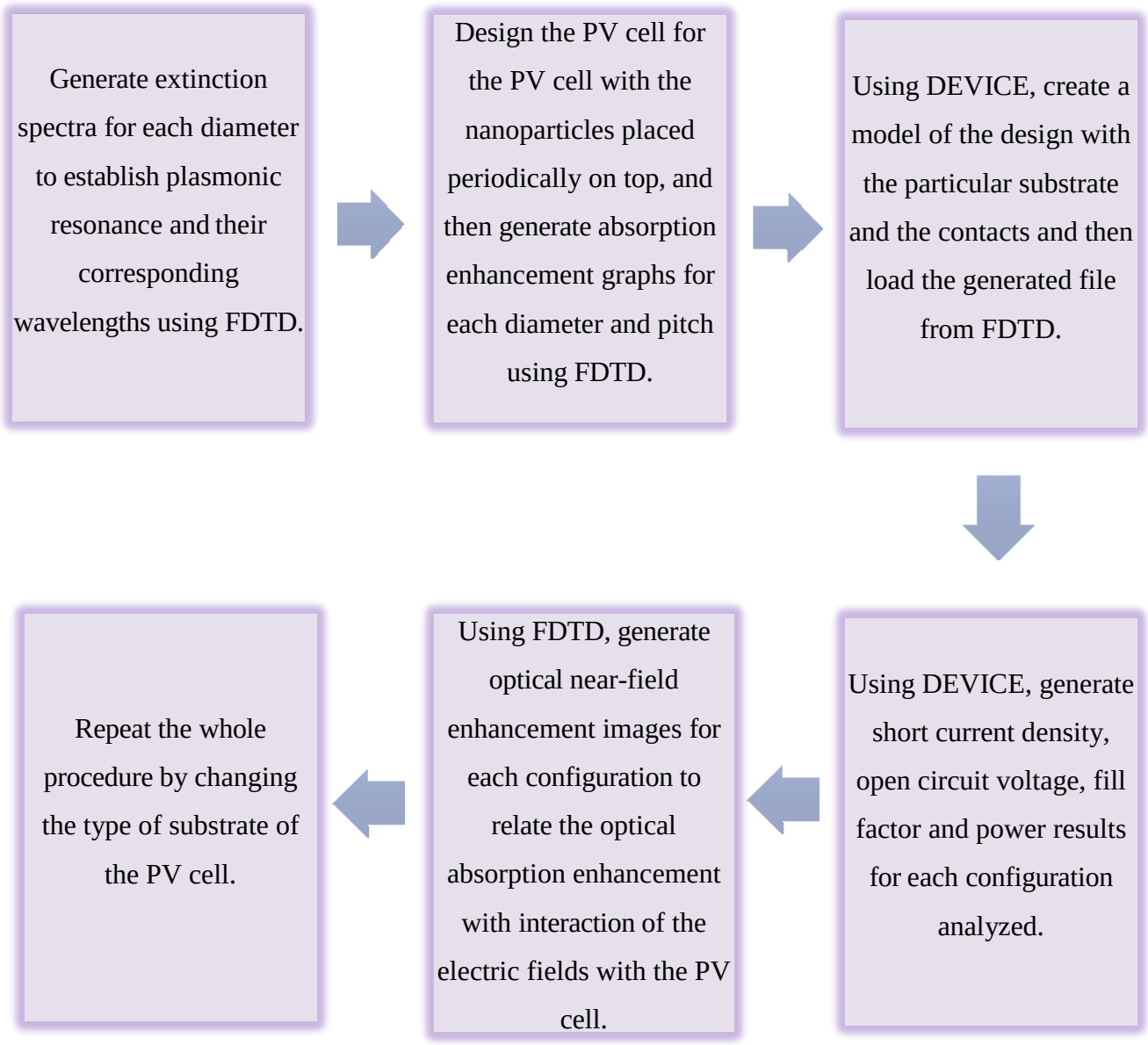

Figure 1. 1 Research Flowchart

1.5 Organization of this Report

The thesis consists of five chapters. A short explanation is introduced here:

- Chapter 1: Introduction

This chapter discusses about the issue relating to the background of the thesis objectives, flowchart and research structure.

- Chapter 2: Literature Review

This chapter discusses mainly about solar cells in general, basic principles of solar cell, thin-film amorphous silicon solar cells, nanostructured solar cells, plasmon resonance phenomena and the finite- difference-time-domain methodology. Some literature regarding this thesis topic is also included in this chapter.

- Chapter 3: FDTD Algorithm

This chapter will give an understanding of the FDTD Algorithm which is the basis for the simulations and data collected from the software by Lumerical Inc. It includes Maxwell's equations as well as the flow chart of the algorithm developed by different scientists.

- Chapter 4: Research Methodology

This chapter will discuss the process of extracting and finding different parameters studied for this research in detail. The process of simulation setup, plasmonic resonance of silver, optical optical absorption enhancement, short circuit current density (J_{SC}), open circuit voltage (V_{OC}), output power (P), fill factor (FF), and near field enhancement images.

- Chapter 5: Result and Discussion

The results of the simulation will be exhibited and critically analyzed to understand any trends or correlations that may be present with the data.

- Chapter 6: Conclusion & Future Work

Finally, a conclusion on the obtained results is presented. This also includes the originalities within the thesis, and suggestions for future work.

CHAPTER 2

LITERATURE REVIEW

2.1 Solar Energy

Solar energy in one form or another is the source of almost all energy on the earth. Like all other animals and plants and species, humans depend on the energy from sun for food and warmth. However, people also harness the sun's energy in numerous other dissimilar ways. For instance, plant matter from a past geological age (fossil fuels), is used for transportation and electricity generation and is basically just stored solar energy from millions of years earlier in the past. Similarly, biomass transforms the sun's energy into a fuel, which can then be utilized for heat, transport or electricity. Wind energy, used for hundreds of years to deliver mechanical energy or for transportation, uses air currents that are formed by solar heated air and the revolution of the earth. Nowadays wind turbines transform wind power into electricity along with its traditional uses. Adding to the fact, even hydroelectricity is derived from the energy from the sun. Hydroelectricity depends on the evaporation of water by the sun, and its following return to the Earth as rain to provide water in dams. Photovoltaic (often abbreviated as PV) is a simple and smart technique of harnessing the energy from the sun. PV devices (solar cells) are unique in that they directly transform the incoming solar radiation into electricity, with no pollution or moving parts, no sound pollution, making them robust, reliable and durable. Solar cells are built on the similar principles and materials behind the communications and computer revolutions, and this section covers the process, use and applications of photovoltaic devices and systems as well as thin-film solar cells and plasmonic solar cells.

2.2 The Greenhouse Effect

Even though the majority of photovoltaic devices used nowadays are for purely practical and economic causes, a potential advantage of photovoltaic is that it is one of the most environmentally friendly techniques of harnessing energy and generating electricity. The ecofriendly impact of power generation, predominantly the greenhouse effect, supplements a

vital motive for investigating photovoltaic. A short summary of the greenhouse effect is discussed below.

The temperature of the Earth is an outcome of an equilibrium established between the incoming radiation from the sun and the energy radiated into space by the Earth. The outgoing radiation emitted by the Earth is intensely affected by the existence and configuration of the atmosphere. If this planet had no atmosphere, as on the moon, the average temperature on the Earth's surface would be about -18°C. However, a natural background level of 270 ppm carbon dioxide (CO_2) in the atmosphere absorbs outgoing radiation, in that way retaining this energy in the atmosphere and warming up the Earth. For this reason, the atmosphere causes the Earth's temperature to be about 15°C on average which is 33°C above the moon. Carbon dioxide absorbs intensely in the 13-19 μm wavelength band and water vapor, one more atmospheric gas, absorbs strongly in the 4-7 μm wavelength band. Most outgoing radiation around 70% escapes in the range between 7-13 μm.

Human activities are gradually releasing "anthropogenic gases" into the atmosphere, which absorb in the 7-13 μm wavelength range, particularly carbon dioxide, ozone, nitrous oxides, methane, and chlorofluorocarbons (CFC's). These gases inhibit the usual escape of energy and potentially will lead to a rise in earthly temperature. Current indication suggests "effective" CO_2 levels will twice over by 2030, causing global warming of 1~4°C. This would lead to changes in rainfall and wind patterns and thus it may cause the interior of continents to dry out and cause the Earth's oceans to rise. Further rises in the release of anthropogenic gases would, of course, cause more drastic effects.

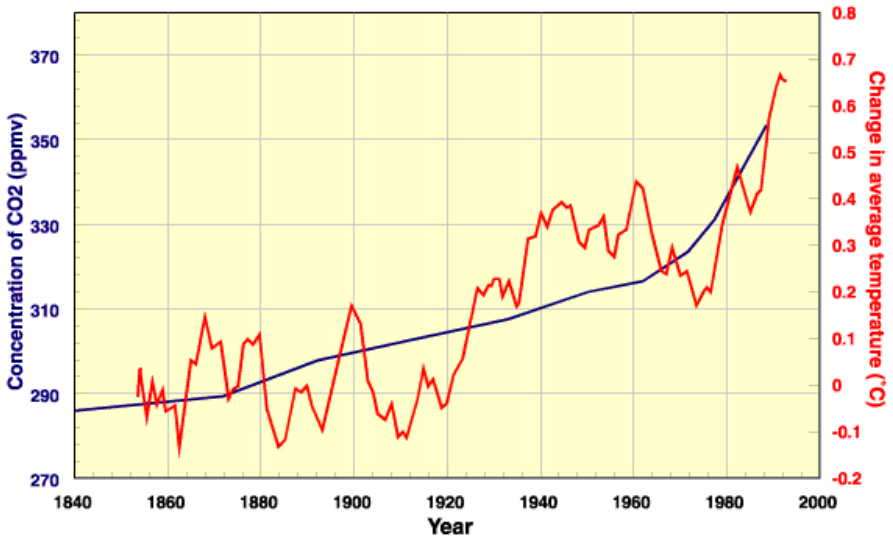

Figure 2. 1 Relationship of the rise in atmospheric carbon dioxide concentration (blue line) with the rise in average temperature (red line)

The graph [34] above only goes to the mid-90s since that was the time writing of PVCDROM started. At the time there was substantial debate about whether the warming was a trend or a statistical fluctuation. By seeing the trend, there was some hope that the average temperatures would decrease again to the level of the statistical average. Unfortunately, in the prevailing years the temperature of the earth has sustained to rise as shown in the graph [35] below.

Evidently, human activities have now reached a scale where they are causing considerable impact on the planet's environment and its appeal to humans. The side-effects could be devastating and technologies with less environmental impact and no "greenhouse gas" emissions are expected to be of increasing importance over the upcoming years. Since the energy sector is the main producer of "greenhouse gases" through the burning of fossil fuels, technologies such as photovoltaic, which can substitute for fossil fuels, must gradually be used [36].

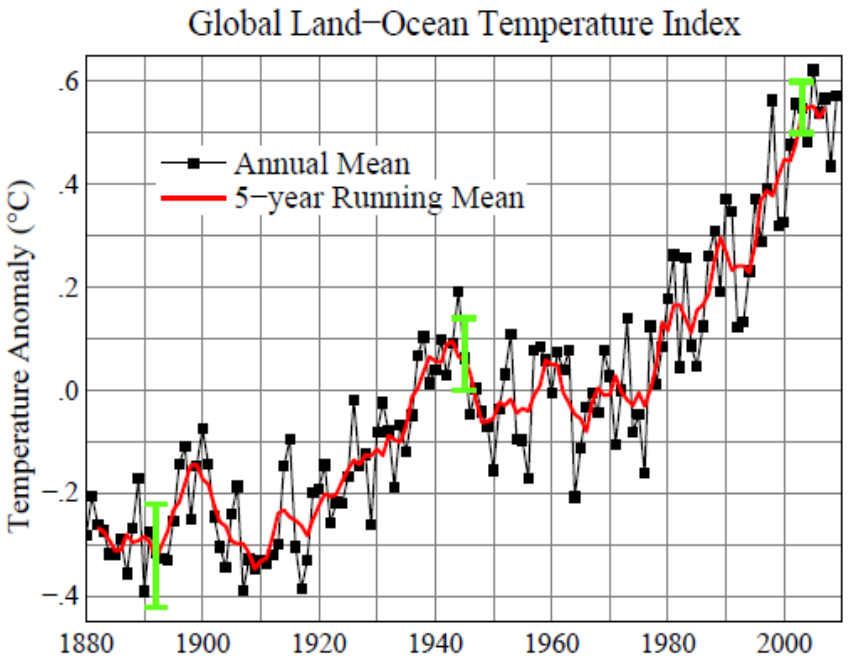

Figure 2. 2 Average surface temperature of the earth. Temperatures are continuing their upward rise.NASA2010

2.3 Properties of sunlight and its effects

The light that is seen daily is only a portion of the total energy emitted by the sun's incident on the earth. Sunlight is a form of "electromagnetic radiation" and the visible light that is seen is a small subdivision of the electromagnetic spectrum shown at the right [37].

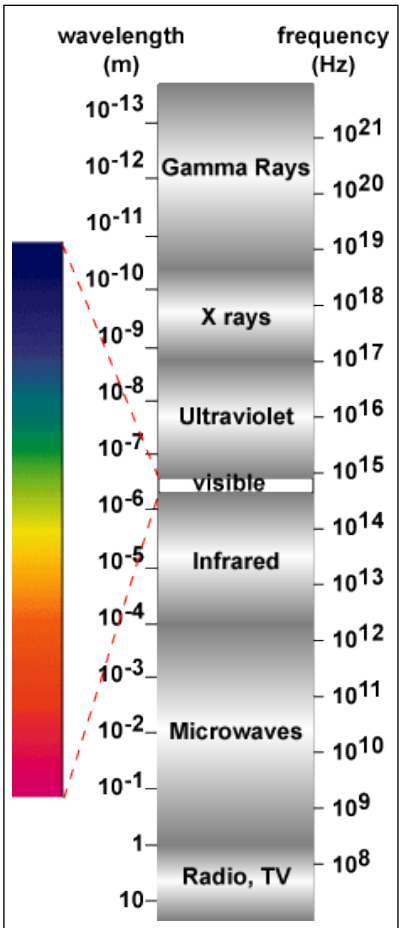

Figure 2. 3 The electromagnetic spectrum.

The electromagnetic spectrum refers to light as a wave which has a particular wavelength. The explanation of light as a wave first gained recognition in the early 1800's when experiments by Thomas Young, François Arago, and Augustin Jean Fresnel exhibited interference effects in light rays, signifying that light is made of waves. By the late 1860's light was regarded as part of the electromagnetic spectrum. On the other hand, in the late 1800's a problem with the wave-based opinion of light became obvious when experiments measuring the spectrum of wavelengths from heated objects could not be clarified by means of the wave-based equations of light. This disagreement was fixed by the works of M. Planck [38] in 1900, and Einstein [39] in 1905.

Planck suggested that the total energy of light consists of vague energy elements, or a quanta of energy. Einstein, while investigating the photoelectric effect (the discharge of electrons from certain metals and semiconductors when hit by light), appropriately distinguished the values of these quantum energy elements. For their work in this field of study, Planck and Einstein won the Nobel Prize for physics in 1918 and 1921, respectively and based upon on this work, light may be regarded as consisting of "packets" or particles of energy, called photons [40].

At present, quantum-mechanics give details about both the observations of the wave nature and the particle nature of light. In quantum mechanics, a photon, like all other quantum-mechanical particles such as electrons, protons etc., is most precisely visualized as a "wave-packet". A wave packet is defined as a group of waves which may interact in such a system that the wave-packet may either seem to be spatially localized (in a similar fashion as a square wave which results from the addition of an infinite number of sine waves), or may

interchangeably appear simply as a wave. In the circumstances where the wave-packet is spatially localized, it acts as a particle. Hence, depending on the condition, a photon may appear as either a wave or as a particle and this idea is called "wave-particle duality"[41]–[43].

A complete physical account of the properties of light needs a quantum-mechanical analysis of light, since light is a type of quantum-mechanical particle called a photon. For photovoltaic applications, this detailed description is occasionally required and for that reason only a few sentences on the quantum nature of light are mentioned here. Nevertheless, in some situations (fortunately, rare in PV systems), light may act in a way which seems to disobey common sense, based on the simple details given here. The term "common sense" refers to this observation and cannot be dependent on to observe the quantum-mechanical effects because these happen under situations outside the range of human observation.

There are quite a few key characteristics of the incident solar energy which are crucial in defining how the incident sunlight interacts with a photovoltaic converter or any other object. The significant characteristics of the incident solar energy are:

- the spectral content of the incident light;
- the radiant power density from the sun;
- the angle at which the incident solar radiation strikes a photovoltaic unit; and
- the radiant energy from the sun throughout a year or day for a particular surface.

2.3.1 Energy of Photon

A photon is characterized by either a wavelength, symbolized by λ or equivalently energy, symbolized by E. There is an inverse relationship among the energy of a photon (E) and the wavelength of the light (λ) given by the equation [44]:

$$E = {}^{hc}/_{\lambda} \tag{2.1}$$

where h is Planck's constant and c is the speed of light,

$h = 6.626 \times 10^{-34}$ Joule·s

$c = 2.998 \times 10^{8}$ m/s

The inverse relationship means that light consisting of high energy photons (such as blue light) has a short wavelength whereas, light consisting of low energy photons (such as red light) has a long wavelength.

When dealing with particles such as electrons or photons, a commonly used unit of energy is the electron-volt (eV) rather than the joule (J). An electron-volt is the energy essential to raise an electron through 1 volt, thus a photon with an energy of 1 eV = 1.602×10^{-19} J.

2.3.2 Solar Radiation at Earth's Surface

The solar radiation incident on the atmosphere of the Earth is relatively constant, but the radiation at its surface differs broadly due to:

- atmospheric effects, including absorption and scattering;
- local variations in the atmosphere, such as water vapor, clouds, and pollution;
- latitude of the location; and
- the season of the year and the time of the day.

The above properties have numerous influences on the solar radiation received at the surface of the Earth. These changes comprise differences in the total power received, the spectral content of the light and the angle from which light is incident on a particular surface. Additionally, an important alteration is that the variability of the solar radiation at a particular place rises intensely. The inconsistency is because of both local effects such as clouds and seasonal variations, along with other effects such as the length of the day at a specific latitude. Desert areas seem to have lesser variations because of local atmospheric phenomena, for instance- clouds. Equatorial regions have low variability between seasons. A picture is shown below [37].



Figure 2. 4 Solar radiation at the surface of Earth differs from the solar radiation incident on the atmosphere of Earth. Air pollution, latitude of a location, cloud cover and the time of the year can all cause differences in solar radiance at the surface of the Earth.

The quantity of energy from sun getting into the Earth's surface every hour is more than the

amount of energy consumed by the population of Earth over an entire year [45].

2.3.3 Atmospheric Effects

The effects of atmosphere have numerous influences on the solar radiation at the surface of the Earth. The picture below illustrates the features which effect the PV applications [37]. The main features which effect the photovoltaic applications are:

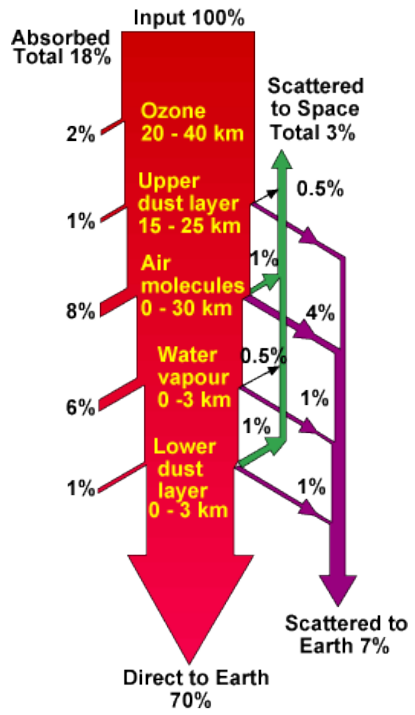

Figure 2. 5 Absorption and scattering of incident sunlight in clear sky

- a decrease in the power of the solar radiation caused by absorption, scattering and reflection in the atmosphere;
- an alteration in the spectral content of the solar radiation because of more absorption or scattering of various wavelengths;
- the presence of a diffuse or unintended component into the solar radiation; and
- local variations in the atmosphere (such as pollution and clouds, water vapor) which have added effects on the incoming power, directionality and spectrum.

2.3.4 Air Mass

The term air mass is the length of the path which light takes through the atmosphere normal to the shortest possible path length (i.e., when the sun is directly overhead). The Air Mass measures the decrease in the power of light as it goes through the atmosphere and is absorbed by air and dust. The Air Mass can be defined by the following equation [37]:

$$AM = \frac{1}{cos\ \theta} \tag{2.2}$$

where θ is the angle from the vertical (zenith angle). Air Mass is value is 1when the sun is directly overhead as shown in the figure [37].

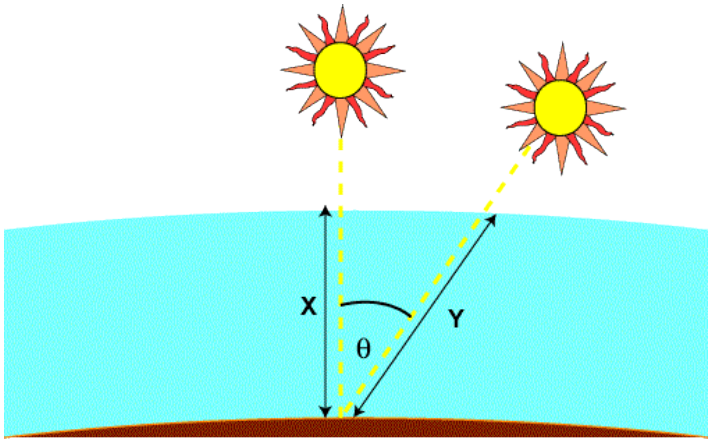

Figure 2. 6 The air mass signifies the percentage of atmosphere that the light has to pass through before striking the Earth in relation to its overhead path length, and is equal to Y/X.

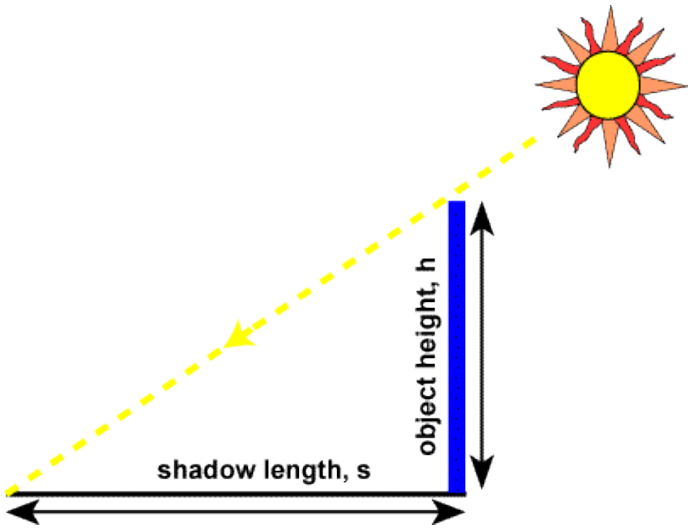

Figure 2. 7 An easy method to determine the air mass is from the shadow of a vertical pole.

Air mass can also be defined as the length of the hypotenuse divided by the object height h as shown in the figure [37], and from Pythagoras's theorem the formula is:

$$AM = \sqrt{1 + \left(\frac{s}{h}\right)^2} \tag{2.3}$$

The calculation for air mass which is shown above assumes that the atmosphere is a plane horizontal layer, but due to the curvature of the atmosphere, the air mass to a certain extent is not equal to the atmospheric path length when the sun is near to the horizon. The air mass becomes infinite when the angle of the sun from the vertical position is 90° (at sunrise), whereas the path length clearly is not. An equation which includes the curvature of the earth is [46]:

$$AM = \frac{1}{\cos\theta \ + 0.5072(96.07995 - \ \theta)^{-1.6364}} \tag{2.4}$$

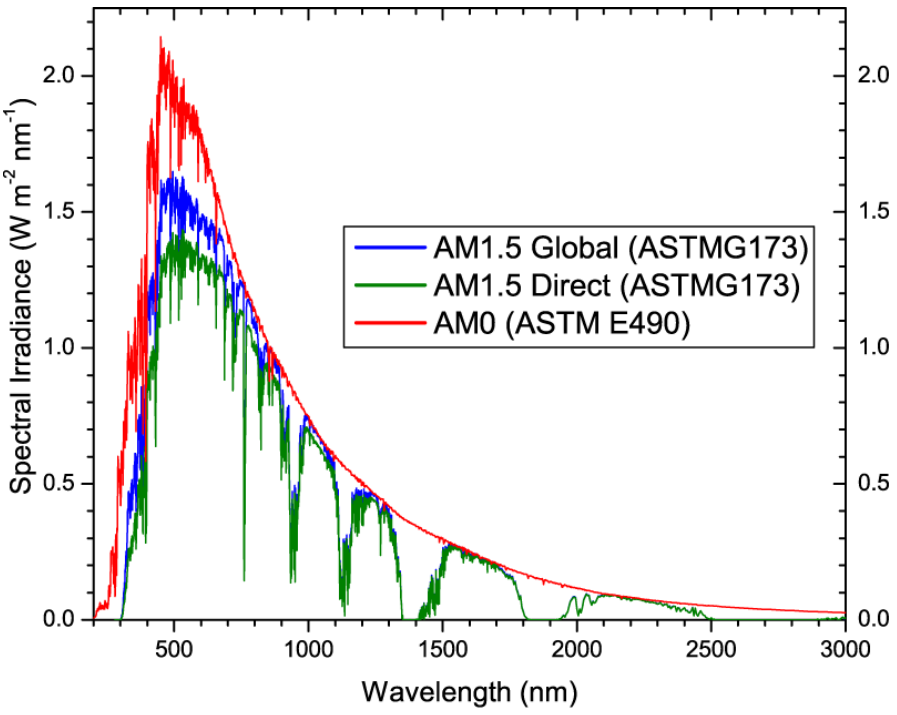

Figure 2. 8 Air Mass- AM0 and AM1.5

2.3.4.1 *ASTM E-490*

The standard space application spectrum is referred to as AM0. It has a 1366.1 W/m^2 built-in power.

2.3.4.2 *ASTM G-173-03 (International Standard ISO 9845-1, 1992)*

For ASTM G-173, two standards are well-defined for terrestrial use. The AM1.5 Global spectrum is designed for plane plate components and has an integrated power of 1000 W/m^2 (100 mW/cm^2). The AM1.5 Direct (+circumsolar) spectrum is defined for work related to solar concentrator. It includes the direct sunbeam from the sun plus the circumsolar component in a disk 2.5 degree around the sun. The AM1.5 Direct (+circumsolar) spectrum has an integrated power density of 900 W/m^2. For generating the standard spectra, SMARTS (Simple Model of the Atmospheric Radiative Transfer of Sunshine) program is used and can also be used to generate other spectra as required [37].

2.4 Semiconductor Materials

Although semiconductor materials in the periodic table originate from different groups, they have certain characteristics. The features of the semiconductor material relate to their nuclear features and vary from group to group. To enhance the design and select the ideal material for a PV implementation, researchers and developers take advantage of such variations.

The atoms in a semiconductor are substances either from group IV of the periodic table, or

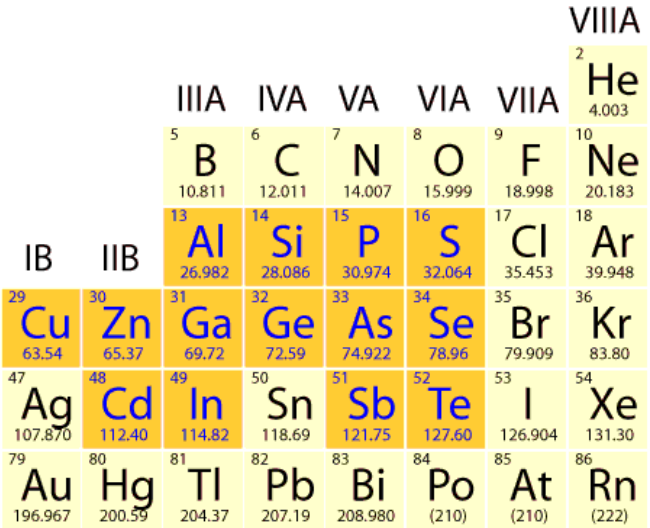

Figure 2. 9 A section of the periodic table. Blue shows more common semiconductor materials

from group III and V (called III-V semiconductors), or from group II and VI systems (called II-VI semiconductors) [47]. Because in the periodic table, different semiconductors consist of components from distinct groups, characteristics differ from one semiconductor to another. As the basis for integrated circuit (IC) chips, silicon, which is a group IV element, is the most widely used semiconductor material and is the most mature technology, and most solar cells are also built on silicon. A section of the periodic table is shown below [37].

2.4.1 Structures of Semiconductors

Semiconductors such as Silicon (Si) consist of individual atoms linked together in a regular, periodic structure to create an arrangement whereby 8 electrons surround each atom. An atom is made up of a nucleus with a core of protons (positively charged particles) and neutrons (particles having no charge) bounded by negatively charged electrons. In a neutral atom the number of protons and electrons is equal, so it means that the atom has electrically no charge. In a semiconductor, the electrons surrounding each atom are part of a covalent bond. A covalent bond is made up of two atoms that share a pair of electrons. Each atom is made up of four covalent bonds with the four neighboring atoms. Thus, 8 electrons are shared between each atom and its four neighboring atoms [48], [49]. A semiconductor's structure is displayed in the figure below [37].

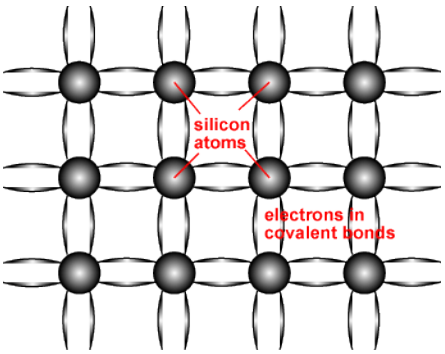

Figure 2. 10 Schematic illustration of covalent bonds in a silicon crystal lattice. Every line attaching the atoms signifies an electron being shared amongst the two. Two electrons being shared form the covalent bond.

2.4.2 Conduction in Semiconductors

A semiconductor's bond structure determines its material characteristics. The energy levels that the electrons can occupy and how they move around the crystal lattice are one of the main effects. Covalent bond holds the electrons which are created between each of the atoms in the lattice structure and therefore the electrons are located in the region containing the atom. These bonded electrons are not capable of moving or changing energy and are therefore not considered free and cannot take part in current flow, absorption or any other physical processes of involvement in solar cells. Nevertheless, all electrons in this "stuck"

bonded structure, are only at complete zero temperature. Electrons can obtain enough energy to escape from their bonds at higher temperatures, particularly at the temperatures where solar cells function. The atoms are free to move around the crystal lattice and engage in conduction when this happens. That being said, a semiconductor has sufficient free electrons at room temperature to permit the flow of electricity whereas a semiconductor acts like an insulator at or near absolute zero [50]–[52].

When an electron receives sufficient energy to engage in conduction (i.e. "free to move"), it is at a higher energy level. The electron is at a low energy state when the electron is bound and therefore cannot engage in the conduction. The existence of the bond between the two atoms therefore creates two separate energy states for the electrons. The electron is unable to achieve intermediate energy values to these two levels; either it is in the bond's lower energy state, or it has gained sufficient energy to break loose and thus has a certain amount of energy. For a semiconductor, this certain amount of energy is called its band gap. The amount and energy of these free electrons which are involved in conduction, is fundamental to the functioning of electronic systems.

The space which is left behind by the electrons enables a covalent bond to shift from one electron to another, making it look like a positive charge moving through the crystal lattice. This empty space is frequently referred to as a hole, comparable to an electron, but with a positive charge [52].

The most significant parameters for solar cell activity of a semiconductor material are:

- the band gap;
- the number of free carriers (electrons or holes) available for conduction; and
- the generation and recombination of free carriers (electrons or holes) in response to light shining on the material.

2.4.3 Band Gap in Semiconductors

A semiconductor's band gap is the minimum energy needed to excite an electron that is stuck in its covalent bond into a free state where it can take part in the conduction. Its band structure provides the electrons' energy on the y-axis and is termed as band diagram [37]. A semiconductor's lower energy level is called the valence band (E_V) and the energy level at which an electron can be called free is known as the conduction band (E_C). The band gap (EG) is the energy gap between the bound state and the free state, between the band of valence and the band of conduction. The band gap is therefore the minimum energy change needed to excite the electron to be able to take part in the conduction.

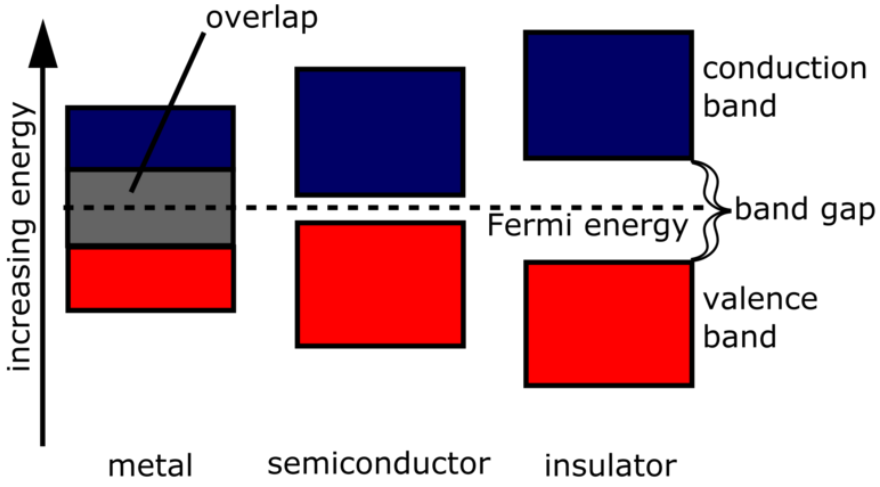

Figure 2. 11 Band gap diagram displaying the various dimensions of conductors, semiconductor and insulator band gaps

Once the electron is pushed into the conduction band, it is able to move freely around the semiconductor and engage in the conduction. In the meantime, an electron's excitation to the conduction band, will also allow for an additional conduction process. An electron's excitation to the conduction band allows an electron to get an empty space. An electron can move into this empty space from a nearby atom. It puts behind another space when this electron passes. The continuous motion of an electron's space, called a hole, can be illustrated as the motion of a positively charged particle through the crystalline structure. As result, the excitation of an electron into the conduction band outcomes not only an electron in the conduction band, but also a hole in the valence band. The electron and the hole therefore, can participate in the conduction and are known as carriers.

The idea of a moving hole is similar to that of a liquid bubble. Even though it is effectively

the liquid that flows, the movement of the bubble moving in the reverse direction is simpler to define [52].

2.4.4 Doping

By doping, it is possible to change the balance of electrons and holes in a silicon crystal lattice. For the production of *n*-type semiconductor material, atoms with one more valence electron than silicon are used. These *n*-type materials are in the periodic table under group V elements, and therefore their atoms have 5 valence electrons which can form covalent bonds with the 4 valence electrons that silicon atoms have. Because only 4 valence electrons of each atom (silicon and *n*-type) are required to form the covalent bonds around the silicon atoms, the additional valence electron is free to engage in the conduction (because *n*-type products have 5 valence electrons) when the two atoms are bonded. As a result, more electrons are introduced to the conduction band and thus increases the amount of electrons present.

P-type material results in atoms with one less valence electron. In the periodic table, these *p*-type materials are elements of group III. Thus, *p*-type material only has 3 valence electrons to bond with the atoms of silicon. The net result is a hole because there are not enough electrons to form the four covalent bonds that surround the atoms. The amount of electrons trapped in bonds in *p*-type material is greater, thereby increasing the amount of holes effectively. There is always more than one sort of carrier in doped material than the other and the type of carrier with the higher concentration is called a majority carrier, whereas the lower concentration carrier is known as minority carrier [51], [52]. A schematic is shown in

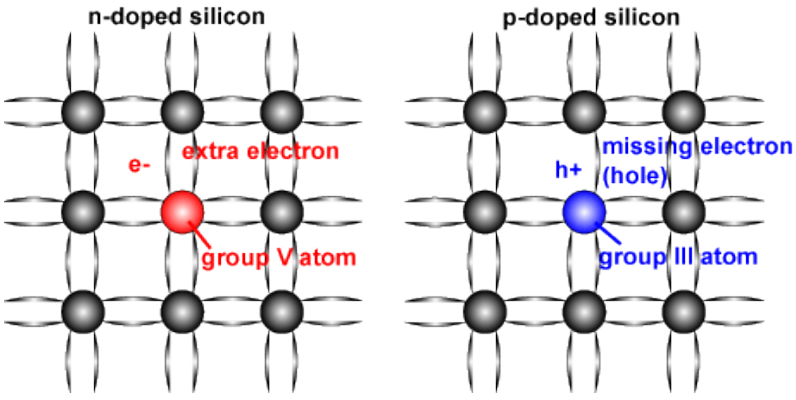

Figure 2. 12 Schematic of a silicon crystal lattice doped with impurities to form n-type and p-type semiconductor material.

the figure below [37].

The table below summarizes the characteristics of semiconductor types in silicon.

Table 2. 1 Properties of semiconductor types in silicon

	N-type (negative)	P-type (positive)
Dopant	Group V (e.g. Phosphorous)	Group III (e.g. Boron)
Bonds	Excess Electrons	Missing Electrons (Holes)
Majority Carriers	Electrons	Hole
Minority Carriers	Holes	Electrons

2.5 Generation and Recombination of electron –holes pairs

The method by which electrons, producing an electron-hole pair, are excited from the valence band to the conduction band is called generation. The reverse process is called recombination, which involves relaxation of free electrons from the CB into a vacancy (hole) in the VB, resulting the destruction of an electron-hole pair. Generation and Recombination happen at the same rate within the cell under thermal equilibrium to maintain the electrons and holes populations.

If the process of generation requires input energy from photons, phonons (vibrational energy of the lattice), or kinetic energy from other particles, recombination is a process of relaxation in which energy is released by the same mechanisms. The following subsections provide a more comprehensive description [52].

2.5.1 Generation

To operate a solar cell, the absorption of light and the generation of an electron hole pair are fundamental. The coefficient of absorption defines how far light of a specific wavelength can pass into a material before it is absorbed. Light is poorly absorbed in a material with lower absorption coefficient, and if the material is too thin, the material will look as if it is transparent to that wavelength. The coefficient of absorption relies on the material as well as the wavelength of light that is being absorbed. Semiconductor materials have a sharp edge in their coefficient of absorption, because the light that has energy just below the band gap does not have enough energy to energize an electron from the valence band into the

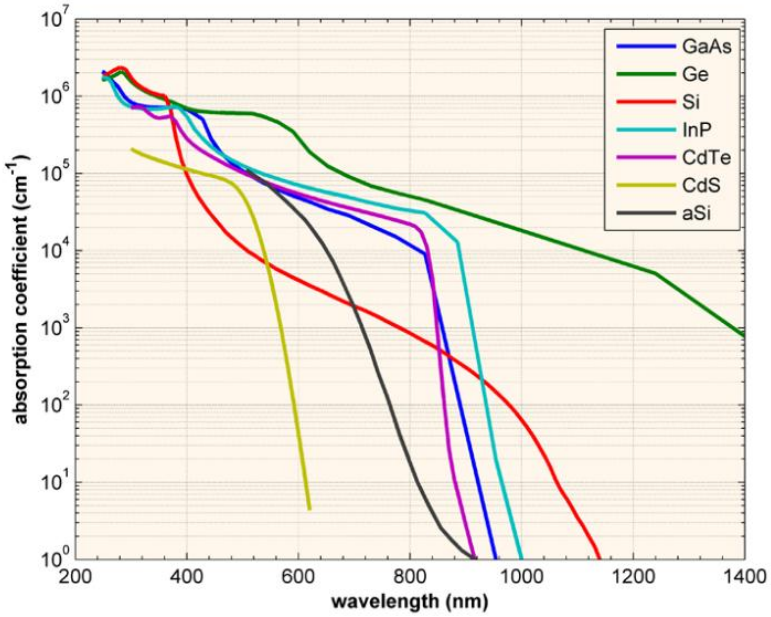

Figure 2. 13 The absorption coefficient, α, in a variety of semiconductor materials at 300K as a function of the vacuum wavelength of light.

conduction band [52]. This light therefore is not absorbed. The absorption coefficient for a number of semiconductor materials is shown in the figure [37]. The key points of the generation process is mentioned in the following:

- If the photon's energy is equal to or greater than the material's band gap, the photon is absorbed by the material and stimulates the electron into the conduction band.
- When a photon is absorbed, both minority and majority carrier are generated.
- The generation of photon charge carriers is the cornerstone for the creation of photovoltaic electricity.
- Different substrates of semiconductors have distinct absorption coefficients.
- Higher absorption coefficient materials more easily absorb photons that stimulate electrons into the conduction band.
- Knowing material absorption coefficients helps engineers to determine which materials to use in their models for solar cells.
- The absorption depth is provided by the reverse of the coefficient of absorption and explains how intensely light penetrates into a semiconductor before being absorbed.

- Higher energy light has a smaller wavelength and a smaller absorption range than lower energy light, which will not be absorbed as easily and has a higher absorption depth.
- Absorption depth influences features of the design of solar cells, like the thickness of the material of the semiconductor.
- The generation of an electron-hole pair can be determined for the complete standard solar spectrum, at any position within the solar cell or at any wavelength of light.
- Generation is the largest on the material surface where most of the light is absorbed.
- Since the light used in photovoltaic applications includes many distinct wavelengths, the design of a solar cell requires consideration of many different generation rate.

2.5.2 Recombination

The opposite of generation is the recombination process. An electron recombines with a hole and produces either heat or light by giving up the energy. It is also called a light emitting diode (LED) a device where the recombination is designed specifically to give off light.

Any electron in the conduction band is in a semi-stable state and will ultimately settle in the valence band to a lower energy state. It has to shift into an empty valence band state when this happens. Therefore, if the electron returns to the valence band, it effectively eliminates a hole as well. And this process is known as recombination. In the majority of a single crystal semiconductor, there are three basic types of recombination. These are:

- Radiative recombination;
- Auger recombination; and
- Shockley-Read-Hall recombination.

The lifetime of the minority carrier and the diffusion length parameters are heavily dependent on the type and magnitude of the semiconductor recombination processes. SRH recombination is the prevalent mechanism of recombination for numerous types solar cells made out of silicon. The recombination rate will rely on the amount of faults in the material, as doping increases the number of defects in the solar cells. Also, the rate of SRH recombination is increased by doping. Moreover, since Auger recombination will be more expected to exist in heavily doped and excited material, as doping increases, the recombination process itself is enhanced. The technique used to manufacture and process the semiconductor wafer also has a significant effect on the length of the diffusion [52].

The key points of the recombination process is mentioned in the following:

- Eventually, electrons, recombining with a hole, lose energy and settle back to the valence band.
- Three recombination types exist: Radiative, Shockley-Read-Hall and Auger.
- In silicon-based solar cells, SRH recombination from Auger recombination dominates.
- Recombination, among other variables is connected with the lifetime of the material, and hence of the solar cell.

- A semiconductor's lifespan depends on the rate of recombination, which depends on the concentration of minority carriers.
- The material's lifespan takes into consideration the different recombination types.
- Lifetime is an indication of the solar cell's efficiency and is therefore a main factor in the selection of solar cell materials.
- The average length that a carrier moves between generation and recombination is known as the diffusion length.
- Highly doped semiconductor materials have higher rates of recombination and therefore have shorter diffusion length.
- Higher diffusion lengths are reflective of longer lifetime of materials and thus an important attribute with semiconductor materials to be considered.
- Recombination is quite high in areas of deformities, such as on the surface of solar cells where the lattice is interrupted.
- In solar cells, surface recombination is high, but can be constrained.
- Understanding the effects and the methods of limiting surface recombination results in better and more robust models of solar cells.

The pictures below [37] show the illustration of the photo generation and recombination process.

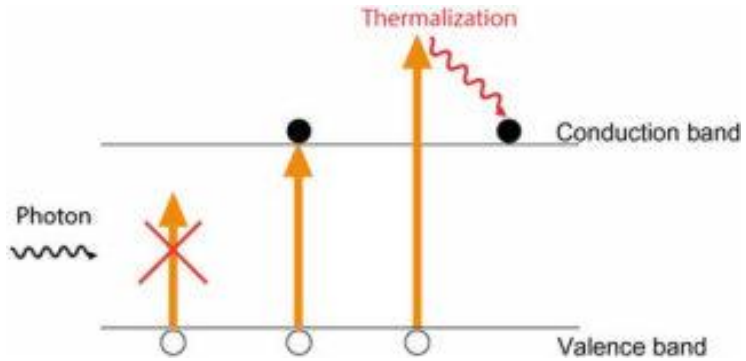

Figure 2. 14 Drawing of the photogeneration process, portraying (left) transparency loss mechanism, (center) photogeneration, (right) thermalization loss.

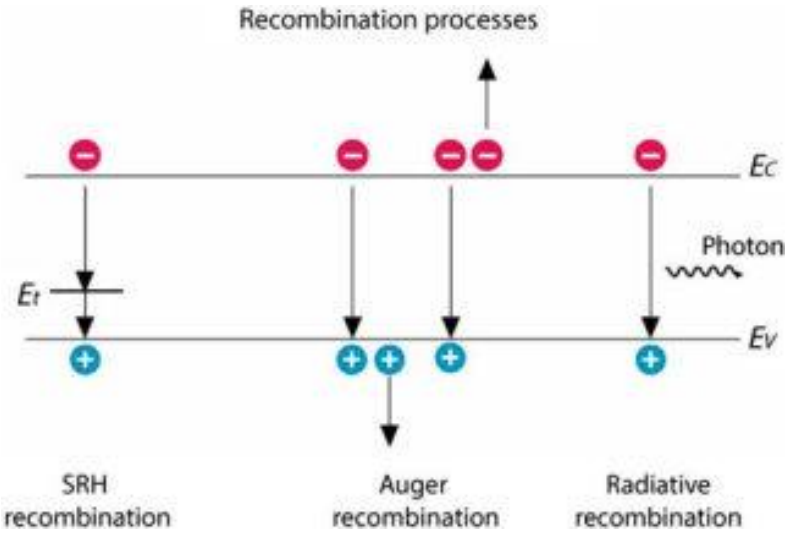

Figure 2. 15 Scheme of the main recombination processes

2.6 Solar Cell Structures and Operation

2.6.1 P-n junction

As shown below, p-n junctions are formed by fitting together materials of the n-type and p-type semiconductor. Since the region of n-type has a high concentration of electrons and the p-type has a high concentration of hole, electrons diffuse from the side of n-type to the side of p-type. Likewise, the holes flow from the p-type side to the n-type side by diffusion. If the electrons and holes were not charged, this process of diffusion would proceed until there was the same concentration of electrons and holes on both sides as if two gases were in contact with one another. Even so, when the electrons and holes migrate to the other side of the p-n junction, they leave behind uncovered charges on dopant atom locations that are fixed in the crystal lattice and therefore unable to move. Positive ion cores are exposed on the n-type side whereas negative ion cores are exposed on the p-type side. Between the positive ion cores in the n-type material and negative ion cores in the p-type material, an electric field is formed. This region is known as the depletion region, as the electric field sweeps free carriers quickly, which is why the region is depleted from free carriers. Due to the electric field, a built-in potential Vbi is formed at the junction [52]. The picture below [37] shows the

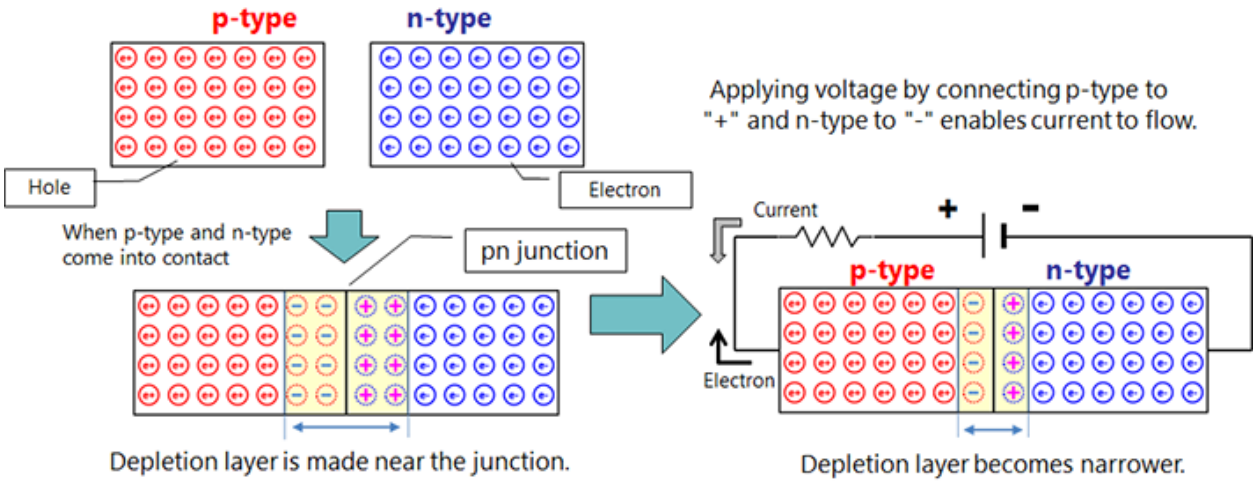

Figure 2. 16 An overview of the mechanism p-n junction

overview of the mechanism of p-n junction.

2.6.2 Solar Cell Structure

A solar cell is an electronic device that transforms sunlight directly into electricity. Light falling on the solar cell generates a current as well as a voltage to produce electricity. First, this method involves a material in which the absorption of light lifts an electron to a higher energy state, and second, moving this high energy electron from the solar cell to an external circuit. In the external circuit, the electron then dissipates its energy and returns back to the solar cell [37]. The requirements for photovoltaic energy conversion may be met by a variety of materials and processes, but in reality almost all photovoltaic energy transformation uses semiconductor materials in the manner of a p-n junction [52].

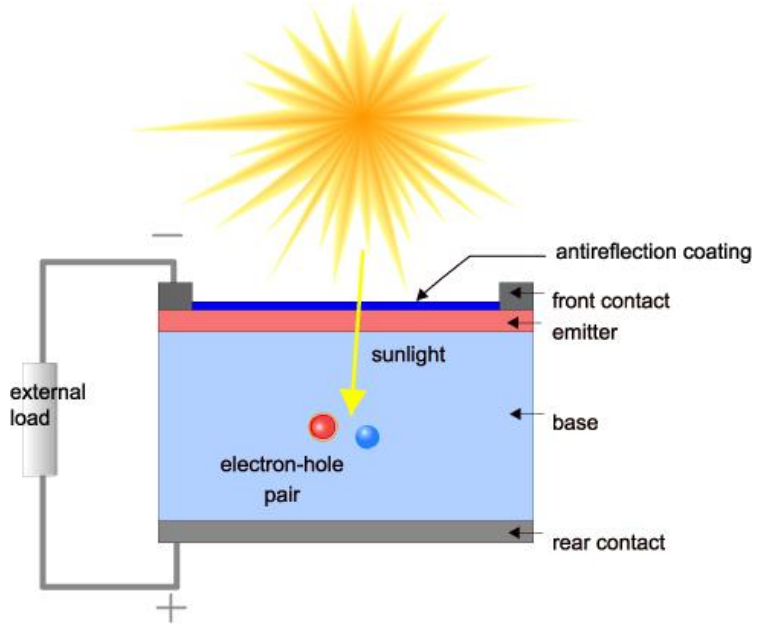

Figure 2. 17 Cross-section of a typical solar cell

2.6.3 Solar Cell Operation

The fundamental steps in a solar cell's operation are:

- the generation of light-generated carriers;
- the collection of the light-generated carriers to generate a current;
- the generation of a large voltage across the solar cell; and
- the dissipation of power in the load and in resistances.

There are two main procedures involved in generating current in a solar cell, recognized as the light-generated current. The first method is to absorb incident photons in order to create pairs of electron-holes. In the solar cell, electron-hole pairs will be generated as long as the incident photon has more energy than the band gap. But then again, electrons (in the material of the p-type) and holes (in the material of the n-type) are meta-stable and will only exist, on average, for a length equal to the lifetime of the minority carrier before recombining. If the carrier recombines, the light-generated electron-hole pair will be lost and therefore no current or power will be generated.

A second method which involves the collection of these carriers by the p-n junction, prevents this recombination by using a p-n junction to distinguish the electron from the hole temporally. The carriers are isolated at the p-n junction by the action of the electric field. If the light-generated minority carrier hits the p-n junction, at the intersection, where it is now a majority carrier, it is swept across the junction by the electric field. The light-generated carriers flow through the external circuit if the base and emitter of the solar cell are linked together (that is if the solar cell is short-circuited).

Quantum Efficiency (QE) is the ratio of the amount of electrons that the solar cell collects to the amount of photons incident on the solar cell of a specified energy. The quantum efficiency can be provided either as a wavelength feature or as an energy function. If all photons of a particular wavelength are absorbed and the resulting minority carriers are gathered, then the value of the quantum efficiency at that particular wavelength will be unity [52].

2.7 Solar Cell Parameters

2.7.1 Short Circuit Current

The short-circuit current is the current through the solar cell when the voltage across the solar cell is zero (i.e., when the solar cell is short circuited). Usually written as ISC, the short-circuit current is shown on the IV curve below [37].

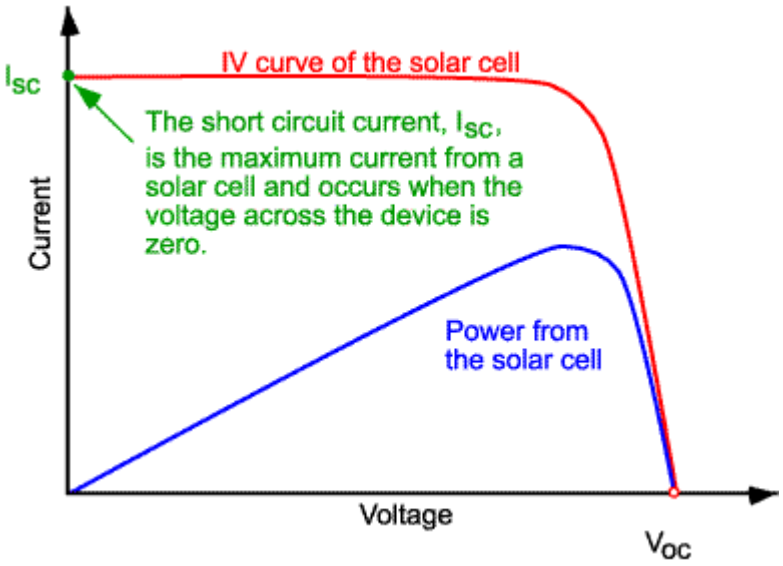

Figure 2. 18 I-V curve of a solar cell showing the short-circuit current.

The short-circuit current is due to the generation and collection of light-generated carriers. For an ideal solar cell at most moderate resistive loss mechanisms, the short-circuit current and the light-generated current are identical. Therefore, the short-circuit current is the largest current which may be drawn from the solar cell.

The short-circuit current depends on a number of factors which are described below:

- the area of the solar cell. To remove the dependence of the solar cell area, it is more common to list the short-circuit current density (Jsc in mA/cm2) rather than the short-circuit current;
- the number of photons (i.e., the power of the incident light source). Isc from a solar cell is directly dependent on the light intensity;
- the spectrum of the incident light. For most solar cell measurement, the spectrum is standardized to the AM1.5 spectrum;
- the optical properties (absorption and reflection) of the solar cell; and
- the collection probability of the solar cell, which depends chiefly on the surface passivation and the minority carrier lifetime in the base.

When comparing solar cells of the same material type, the most critical material parameter is the diffusion length and surface passivation. In a cell with perfectly passivized surface and

uniform generation, the equation for the short-circuit current can be approximated as [37]:

$$Jsc = qG(L_n + L_p) \tag{2.5}$$

where G is the generation rate, and L_n and L_p are the electron and hole diffusion lengths respectively. Although this equation makes several assumptions which are not true for the conditions encountered in most solar cells, the above equation nevertheless indicates that the short-circuit current depends strongly on the generation rate and the diffusion length.

Silicon solar cells under an AM1.5 spectrum have a maximum possible current of 46 mA/cm^2. Laboratory devices have measured short-circuit currents of over 42 mA/cm^2, and commercial solar cell have short-circuit currents between about 28 mA/cm^2 and 35 mA/cm^2 [37].

2.7.2 Open Circuit Voltage (V_{OC})

The open-circuit voltage, VOC, is the maximum voltage available from a solar cell, and this occurs at zero current. The open-circuit voltage corresponds to the amount of forward bias on the solar cell due to the bias of the solar cell junction with the light-generated current. The open-circuit voltage is shown on the IV curve below [37].

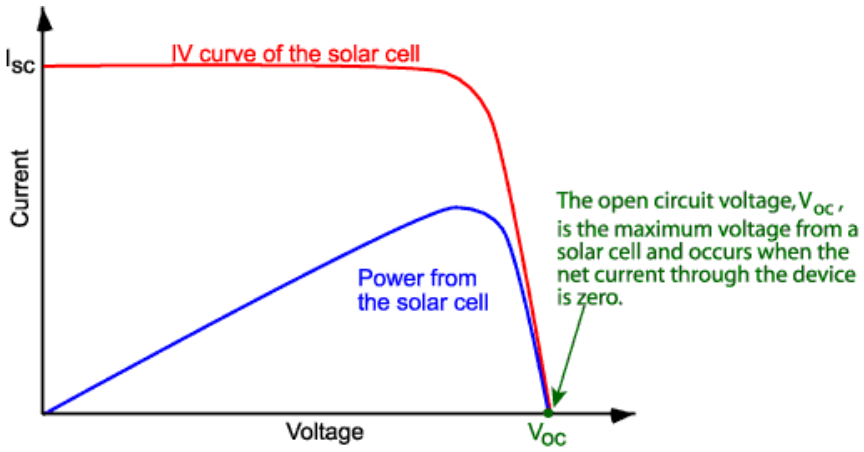

Figure 2. 19 I-V curve of a solar cell showing the open-circuit voltage.

An equation for V_{OC} is found by setting the net current equal to zero in the solar cell equation to give [37]:

$$V_{OC} = \frac{nkT}{q} ln\left(\frac{I_L}{I_0} + 1\right) \tag{2.6}$$

A casual inspection of the above equation might indicate that V_{OC} goes up linearly with temperature. However, this is not the case as I_0 increases rapidly with temperature primarily due to changes in the intrinsic carrier concentration ni. The effect of temperature is complicated and varies with cell technology. V_{OC} decreases with temperature. If temperature changes, I_0 also changes.

The above equation shows that Voc depends on the saturation current of the solar cell and the light-generated current. While Isc typically has a small variation, the key effect is the saturation current, since this may vary by orders of magnitude. The saturation current, I0 depends on recombination in the solar cell. Open-circuit voltage is then a measure of the amount of recombination in the device. Silicon solar cells on high quality single crystalline material have open-circuit voltages of up to 764 mV under one sun and AM1.5 conditions [53], while commercial devices on multi-crystalline silicon typically have open-circuit voltages around 600 mV.

The VOC can also be determined from the carrier concentration [54]:

$$V_{OC} = \frac{kT}{q} ln\left[\frac{(N_A + \Delta n)\,\Delta n}{n_i^2}\right] \tag{2.7}$$

where kT/q is the thermal voltage, NA is the doping concentration, An is the excess carrier concentration and ni is the intrinsic carrier concentration. The determination of V_{OC} from the carrier concentration is also termed Implied V_{OC} [37], [52].

2.7.3 Fill Factor

The short-circuit current and the open-circuit voltage are the maximum current and voltage respectively from a solar cell. However, at both of these operating points, the power from the solar cell is zero. The "fill factor", more commonly known by its abbreviation "FF", is a parameter which, in conjunction with Voc and Isc, determines the maximum power from a solar cell. The FF is defined as the ratio of the maximum power from the solar cell to the product of Voc and Isc so that [37]:

$$FF = \frac{V_{MP}\, I_{MP}}{V_{oc} I_{oc}} \tag{2.8}$$

Graphically, the FF is a measure of the "squareness" of the solar cell and is also the area of the largest rectangle which will fit in the IV curve. The FF is illustrated below [37].

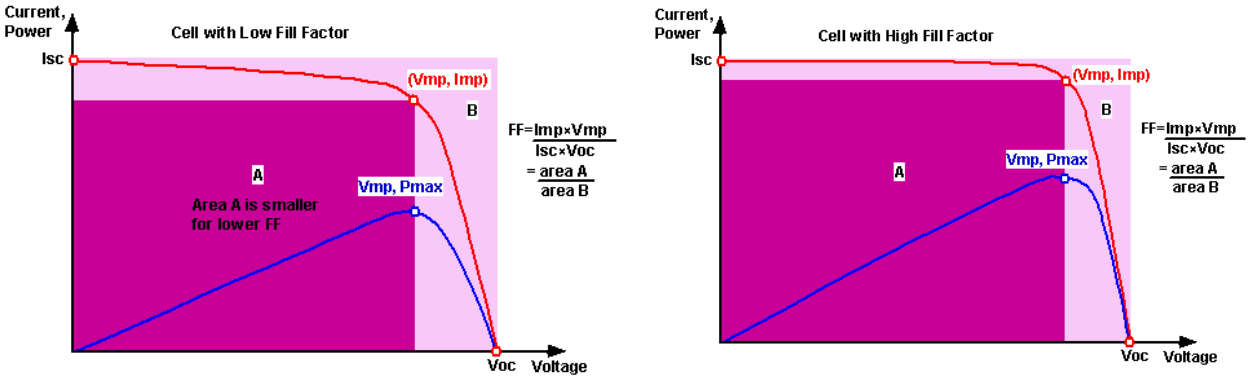

Figure 2. 20 Graph of cell output current (red line) and power (blue line) as a function of voltage. Also shown are the cell short-circuit current (Isc) and open-circuit voltage (VOC) points, as well as the maximum power point (Vmp, Imp).

2.7.4 I-V Curve

The IV curve [37] of a solar cell is the superposition of the IV curve of the solar cell diode in the dark with the light-generated current. The light has the effect of shifting the IV curve down into the fourth quadrant where power can be extracted from the diode. Illuminating a cell adds to the normal "dark" currents in the diode so that the diode law becomes [55]:

$$I = I_O \left[exp\left(\frac{qV}{nkT}\right) - 1 \right] - I_L \qquad (2.9)$$

where I_L = light generated current.

The power curve has a maximum denoted as P_{MP} where the solar cell should be operated to give the maximum power output. It is also denoted as P_{MAX} or maximum power point (MPP) and occurs at a voltage of V_{MP} and a current of I_{MP}.

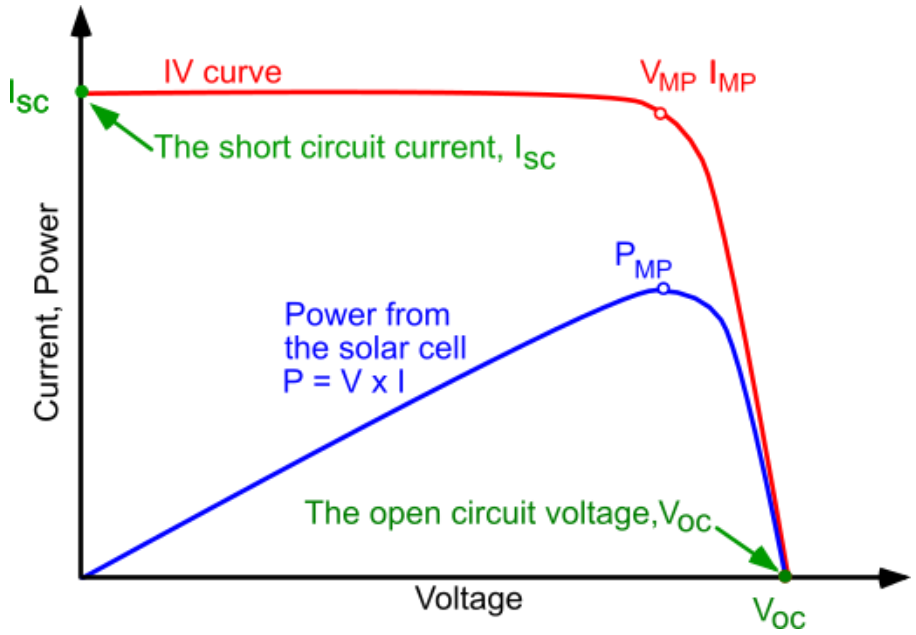

Figure 2. 21 Current voltage (IV) cure of a solar cell. To get the maximum power output of a solar cell it needs to operate at the maximum power point, P_{MP}.

2.7.5 Solar Cell Efficiency

The efficiency is the most commonly used parameter to compare the performance of one solar cell to another. Efficiency is defined as the ratio of energy output from the solar cell to input energy from the sun. In addition to reflecting the performance of the solar cell itself, the efficiency depends on the spectrum and intensity of the incident sunlight and the temperature of the solar cell. Therefore, conditions under which efficiency is measured must be carefully controlled in order to compare the performance of one device to another. Terrestrial solar cells are measured under AM1.5 conditions and at a temperature of 25°C. Solar cells intended for space use are measured under AM0 conditions.

The efficiency of a solar cell is determined as the fraction of incident power which is converted to electricity and is defined as [37]:

$$P_{max} = V_{OC} I_{SC} FF \tag{2.10}$$

$$\eta = \frac{V_{OC} I_{SC} FF}{P_{in}} \tag{2.11}$$

Where:

V_{oc} is the open-circuit voltage;

I_{sc} is the short-circuit current; FF is the fill factor and

η is the efficiency.

The input power for efficiency calculations is 1 kW/m^2 or 100 mW/cm^2. Thus the input power for a 100 × 100 mm^2 cell is 10 W and for a 156 × 156 mm^2 cell is 24.3 W [37].

2.8 Photovoltaic Technologies

Edmond Becquerel appears to have been the first to demonstrate the photovoltaic effect. Working in his father's laboratory as a nineteen year old, he generated electricity by illuminating an electrode with different types of light, including sunlight (see the figure below [56]). Best results were obtained with blue or ultraviolet light and when electrodes were coated with light sensitive material such as AgCl or AgBr. Although he usually used platinum electrodes, he also observed some response with silver electrodes. He subsequently found a use for the photovoltaic effect by developing an "actinograph" which was used to record the temperature of heated bodies by measuring the emitted light intensity [56].

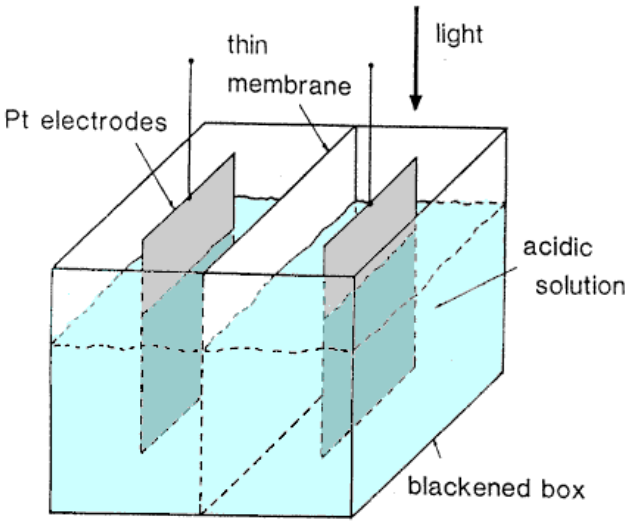

Figure 2. 22 Diagram of apparatus described by Becquerel (1839)

2.8.1 Early Photovoltaic Technologies

Few of the early photovoltaic developments are shown with pictures [57]–[63]:

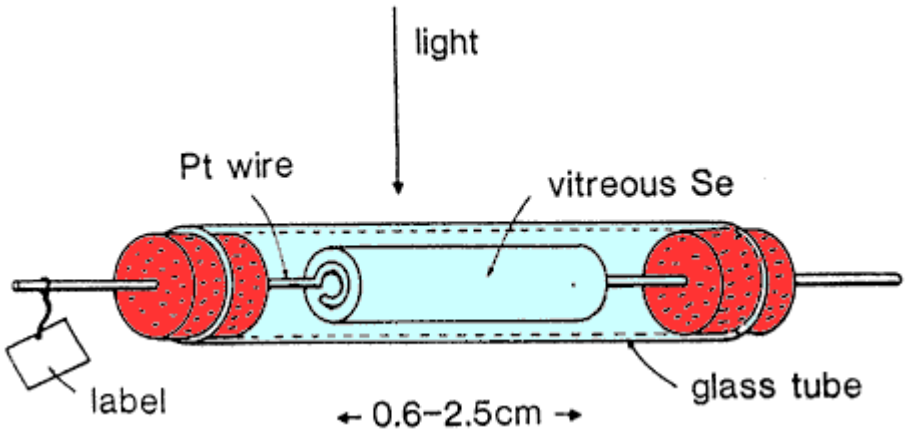

Figure 2. 23 Sample geometry used by Adams and Day (1876) for the investigation of the photoelectric effects in selenium.

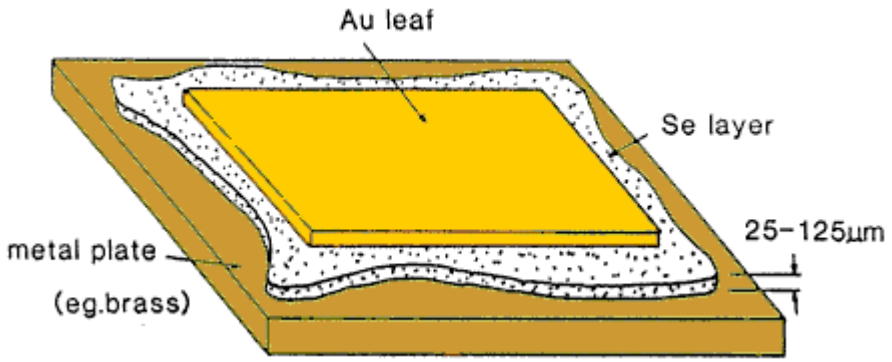

Figure 2. 24 Thin-film selenium demonstrated by Fritts in 1883.

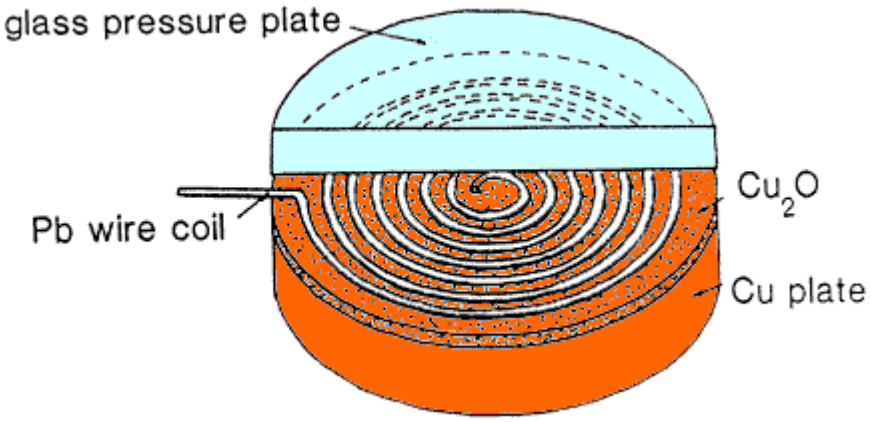

Figure 2. 25 Early Grondahl-Geiger copper-cuprous oxide photovoltaic cell (circa 1927)

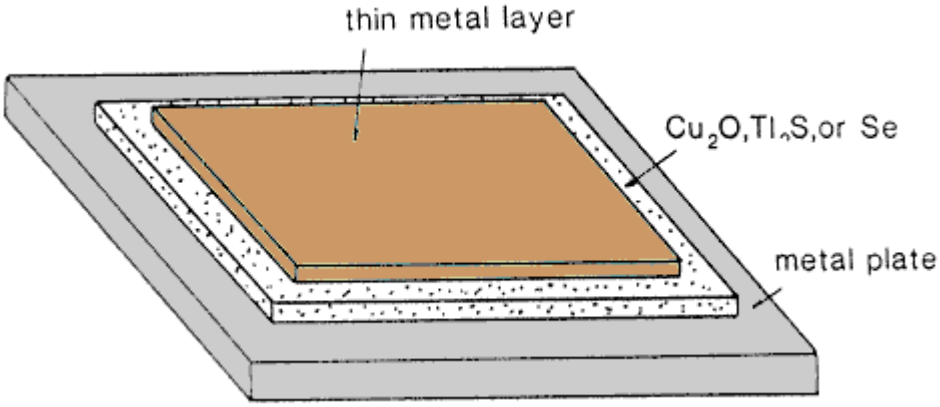

Figure 2. 26 Structure of the most efficient photovoltaic devices developed during the 1930's.

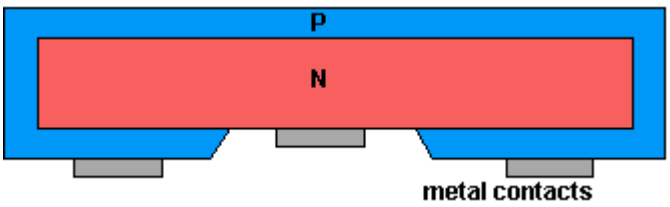

Figure 2. 27 Early silicon solar cell structure.

2.8.2 First Practical Silicon Solar Cells

In the early 1950s Physicists at Bell Laboratories discovered that silicon is more efficient than selenium, creating the first practical solar cell — now 6% efficient [61]. This discovery led to solar cells capable of powering electrical equipment. In 1956, Western Electric began selling commercial licenses for its silicon PV technologies, but the prohibitive costs of silicon solar cells keep them from widespread market saturation.

2.8.3 Generations of Solar Cells

There are three generations of solar cells. The first generation cells are based on mono- and poly-crystalline silicon which are the most widely available commercially, and demonstrate an efficiency of around 15% to 26% [64]. The second generation cells are made from more hybrid material such as amorphous silicon, copper indium gallium selenide (CIGS) and cadmium telluride (CdTe), and typically require less material in their production; however, they have efficiencies of around 10% to 15% [64], [65]. The third and final generation of cells are made from organic materials such as polymers like polyphenylene vinylene and small molecule compounds like copper phthalocyanine (an organic pigment) [66]. This last generation can reach energy conversion efficiencies of up to 20%, but are expensive to manufacture, and thus not effectively scalable for mass production.

2.8.4 Thin Film Solar Cells

Thin film solar cells are the second generations of solar cells. Thin film solar cells are used in several technologies, including cadmium telluride (CdTe), copper indium gallium diselenide (CIGS), and amorphous thin-film silicon (a-Si, TF-Si). Its thickness varies from few nanometers to tens of micrometers which is much thinner than that of crystalline solar cells. This allows thin film cells to be flexible, and lower in weight. This technology has always been cheaper but less efficient than conventional crystalline silicon solar cells. However, research has been done over the years to increase its efficiency. This technology continued to improve so that in the early 21st century the global thin film photovoltaic market was growing at an unprecedented rate. Several types of thin film solar cells are widely used because of their relatively low cost and their efficiency.

2.8.4.1 *Types of Thin Film Solar Cells*

Cadmium telluride thin-film solar cells are the most common type available. They are

less expensive than the more standard silicon thin-film cells. Cadmium telluride thin-films have a peak recorded efficiency of more than 18 percent (the percentage of photons hitting the surface of the cell that are transformed into an electric current). By 2014 cadmium telluride thin-film technologies had the smallest carbon footprint and quickest payback time

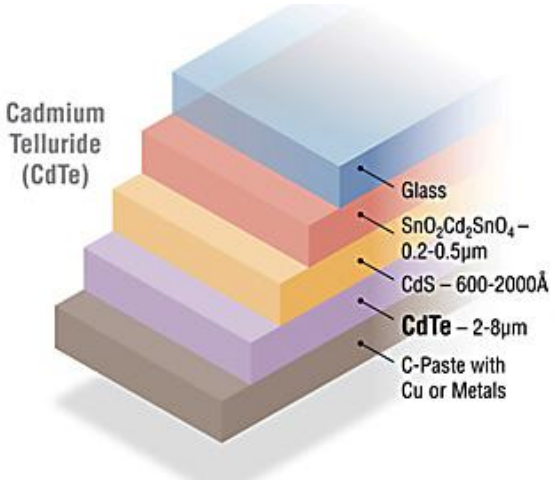

Figure 2. 28 Representation of a typical CdTe superstrate thin-film PV device. In this design, the layers of the device are put onto a glass "superstrate" that permits sunlight to go in. The sunlight passes through the glass and produces electrical current and voltage in the lower layers. PV, Photovoltaic. Diagram reprinted with permission from The National Renewable Energy Laboratory (NREL).

of any thin-film solar cell technology on the market (payback time being the time it takes for the solar panel's electricity generation to cover the cost of purchase and installation) [56]. A model of the CdTe solar cell has been shown above [67].

Copper indium gallium selenide (CIGS) is another type of semiconductor used to manuf acture thin-film solar cells. CIGS thin-film solar cells h ave

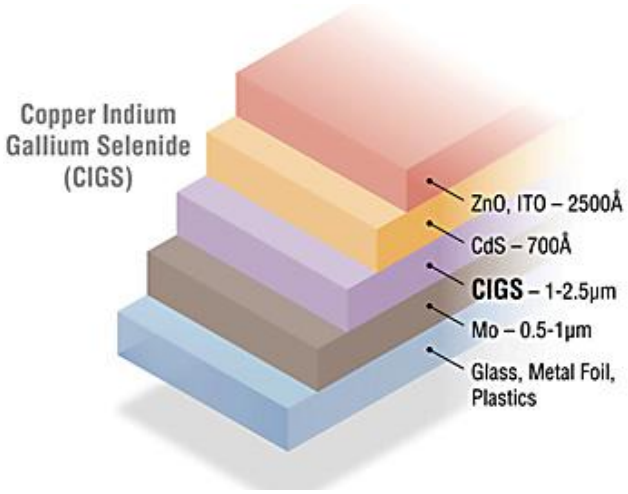

Figure 2. 29 Representation of a typical CIGS substrate thin-film photovoltaic device. In this design, the layers of the device are put onto a glass, metal, or polymer substrate. Sunlight go in through the top layer of the device (the transparent conducting oxide) and produces electrical current and voltage in the lower layers.

reached 20 percent efficiency in laboratory settings and 14 percent efficiency in the field, making CIGS a leader among alternative cell materials and a promising semiconducting material in thin-film technologies. CIGS cells traditionally have been more costly than other types of cells on the market, and for that reason they are not widely used. A diagram has been shown above [67].

Gallium arsenide (GaAs) thin-film solar cells have reached nearly 30 percent efficiency in laboratory environments, but they are very expensive to manufacture. Cost has been a major factor in limiting the market for GaAs solar cells; their main use has been for spacecraft and satellites. The structure of a GaAs cell has been shown below [68].

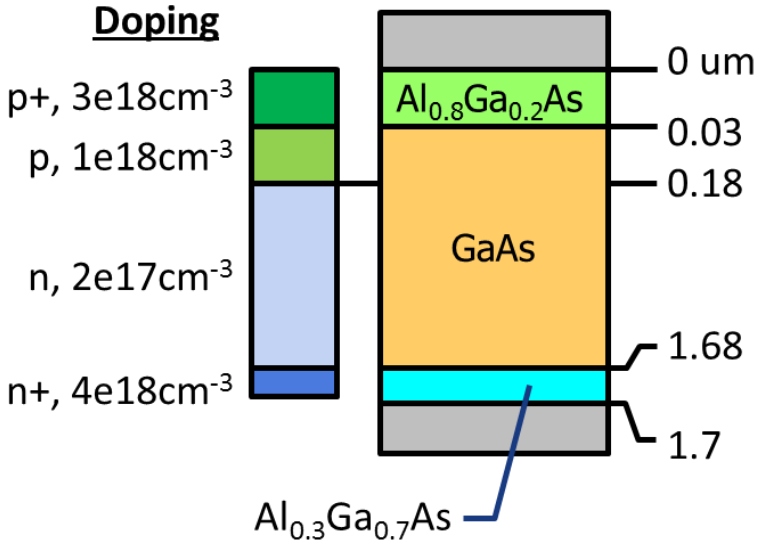

Figure 2. 30 Structure of a GaAs cell. Diagram reproduced with permission from IEEE J. Photovoltaics (X. Wang, et al.).

Amorphous silicon thin-film cells are the oldest and most mature type of thin-film. They are made of monocrystalline silicon, unlike typical solar-cell wafers. Amorphous silicon is cheaper to manufacture than crystalline silicon and most other semiconducting materials. Amorphous silicon is also popular because it is abundant, nontoxic, and relatively inexpensive. However, the average efficiency is very low, 10 percent. The picture below shows the amorphous silicon solar cell [69].

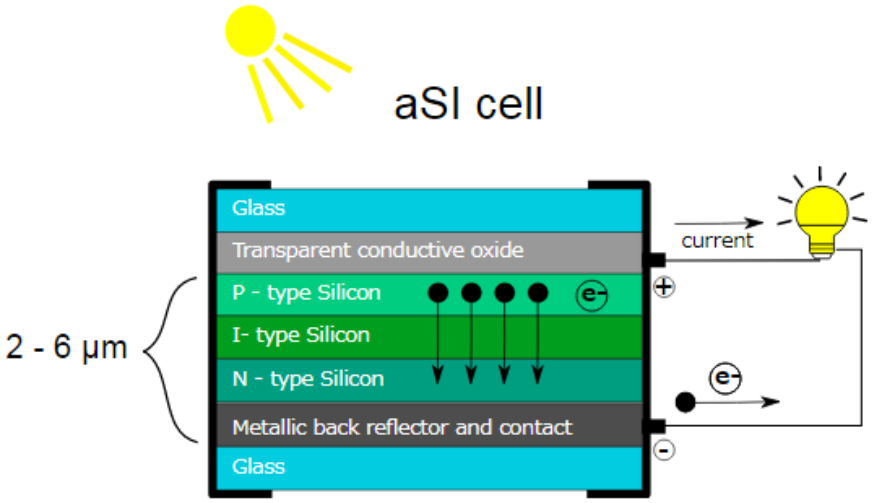

Figure 2. 31 Amorphous silicon (a-Si) is the non-crystalline form of silicon.

2.9 Nanostructured Solar Cells

To improve light-coupling efficiency, patterned nanostructures are designed and implemented in tandem with PV cells. These structures can be made of different materials depending on their optical properties, and are designed to enhance the light coupling efficiency of the solar cell. The nanoscale dimensions of these structures mean that they have a high surface area-to-volume ratio, which complements their overall purpose. The usage of nanostructures provides a significantly cost-effective method to improve cell efficiency, and simultaneously improve efficiency beyond theoretical limits (Shockley- Queisser limit) [70].

Examples of nanostructured solar cells include:

a) Nanowire solar cells, with nanopillars placed periodically on top of the Si substrate

b) Quantum dot solar cells

c) Plasmonic solar cells

d) Mesoscopic solar cells

Nanostructures, in many cases, implement principles that are adhered to in other fields to enhance optical and electrical efficiency of solar cells. For example, moth-eye anti-reflective coatings (ARC) are inspired by the structure of the cornea of nocturnal moths which they utilize to have better vision in the dark [71]. Mesoscopic solar cells couple photo-sensitive pigment within the PV cell itself to provide a cheap thin-film solar cell that in recent studies have proved to be flexible in nature, allowing them to be coated on other machineries and equipment [65], [72]. OSCs utilize materials synthesized from organic substances or polymers that are optically and electronically active, facilitating them to be used as an environmentally friendly source of electrical energy [5].

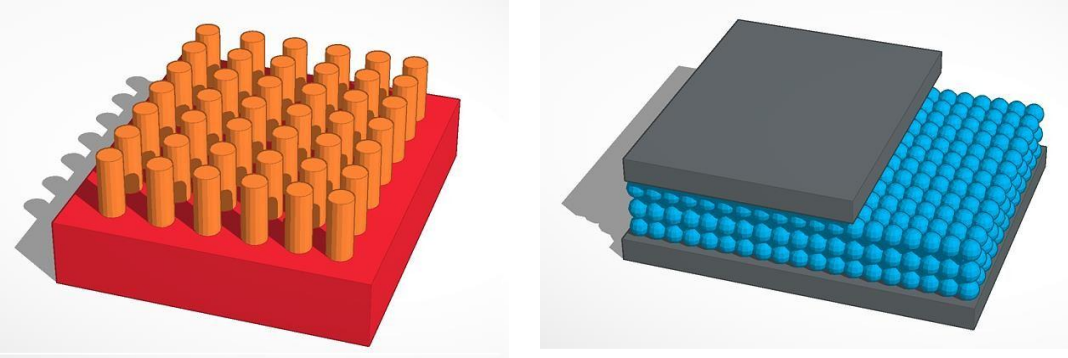

Figure 2. 32 Nanostructured solar cells (A) nanowire solar cells, and (B) quantum dot solar cells

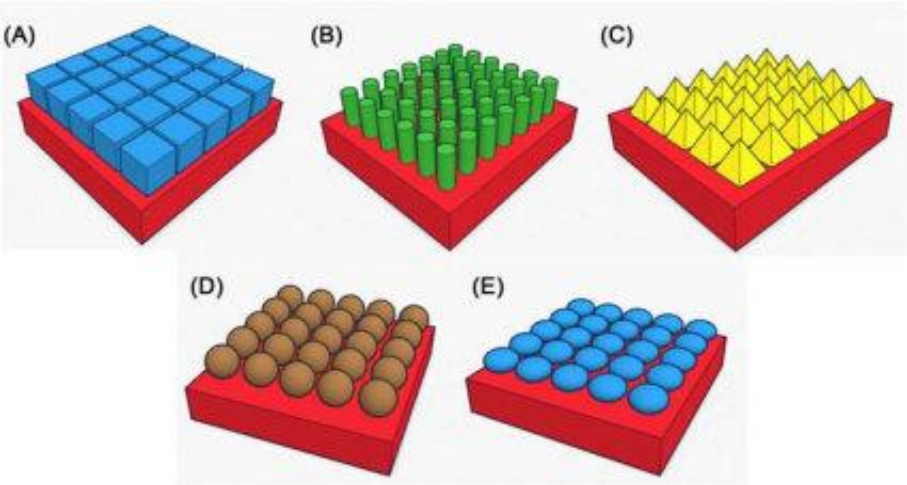

Figure 2. 33 Different shapes of plasmonic nanostructures analyzed—(A) cube, (B) cylinder, (C) pyramid, (D) sphere, and (E) spheroid

2.10 Plasmonic Thin Film Solar Cells

The use of plasmonic in a variety of applications have led to significant research and development in this field over the past three decades. Surface plasmon polaritons (SPP) are generated by electromagnetic fields due to the oscillation of electrons on a metal-dielectric interface [73]. The use of these SPPs in improving PV efficiency has garnered great interest and research [70], [71], [73]–[78]. Studies conducted recently demonstrated the optical absorption and photocurrent generation in semiconductor photodiodes induced by scattering from SPP resonances in metallic nanoparticles deposited on the photodiode surface. Furthermore, they have been coupled with amorphous thin-film Si cells as well [79]–[81]. In order to properly optimize the usage of SPPs, detailed analysis of the dependence of the improvement of PV efficiency on the physical parameters of plasmonic nanostructures must be performed. This thesis will provide a brief analysis of this optimization as an example of how plasmonic nanostructures can improve the optical and electrical efficiencies of solar cells in general, and that this can be achieved by modifying physical parameters of the

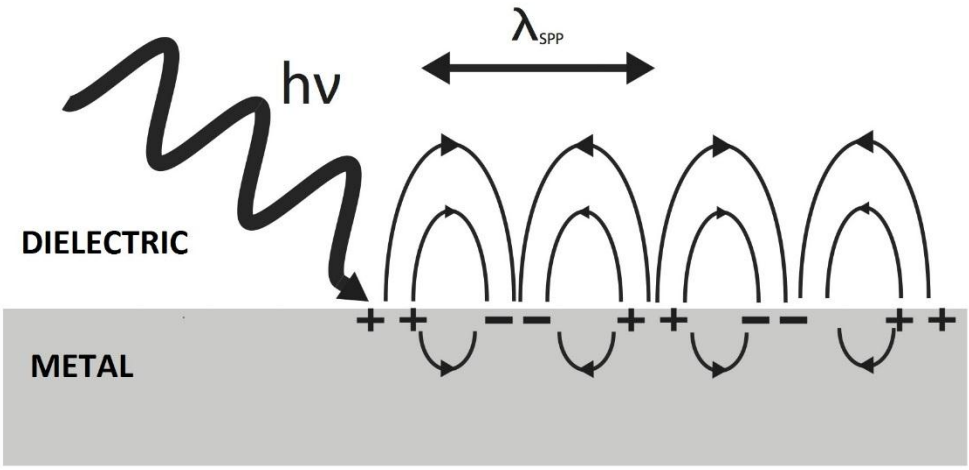

Figure 2. 34 Surface plasmon polariton generation

nanostructures used. The surface plasmon resonance phenomena is illustrated in Figure 2.34 [82].

Plasmonic solar cells allow the thickness of the PV cell to be less than 2µm. Surface plasmon polaritons undergo resonance at certain frequencies, depending on the metal with which the nanostructure is made and the size and shape of the nanostructure [77]. At this state, SPP demonstrate maximum resonance (e.g., scattering and/or absorption) with the incident electromagnetic waves (e.g., sunlight), which can result in greater absorption within

the cell substrate. This phenomenon can be manipulated to improve light coupling efficiency within thin-film solar cells. The metal with which the plasmonic nanoparticles are made is important, as different metals exhibit distinguishable surface plasmon resonances, and thus have varying impacts on the overall optical absorption enhancement [76], [77]. Below are examples of three possible configurations to incorporate plasmonic nanoparticles/nanostructures in thin-film Si solar cells:

- Nanoparticles on the surface the substrate
- Nanoparticles within the substrate
- Nanostructures as/on back contacts

The incorporation of plasmonic metal nanostructures in thin film solar cells could lead to strong light trapping because strong light-matter interaction in plasmonic nanostructures enables large scattering cross sections [76], [77]. Many of these plasmonic photovoltaic designs incorporate metal nanoparticles on the front surface of the cell. This can lead to preferential scattering of the incident light into the semiconductor over an increased angular range, thereby enhancing the optical path length [78]–[81]. While strong enhancements of photocurrent have been reported in such solar cells for near-band edge light, these are often offset by a reduced photocurrent in the blue part of the solar spectrum due to destructive interference [71], [78]. An alternative strategy is to build the scattering nanostructures directly into the back contact of the device. In this geometry, the incident blue light is directly absorbed and does not interact with the back contact scatters, while the red light that is poorly absorbed in a single pass through the cell is strongly scattered [4], [12], [83]–[85]. In our design, these periodically-arranged nanoparticle arrays on top of the amorphous silicon substrate are designed to couple incident light into guided modes supported by the cell with high efficiency in the absorbing semiconductor layer, dramatically reducing the thickness requirements by redirecting the absorption path into the plane of the solar cell. As opposed to cells with structures whose sole purpose is to act as reflectors [65], [66], [72], [86], [87] or nanostructure designs to couple specifically to surface plasmon polariton modes [28], [88], the design presented here takes advantage of the high scattering cross sections of plasmonic nanostructures themselves to couple to waveguide modes. To date most theoretical and experimental studies of plasmonic light trapping structures has dealt extensively on the plasmonic nature of the nanostructures and how these have been successful at providing optical absorption enhancements of the cell [28], [80], [81], [83], [84], [88]–[90]. While this

reference is useful for understanding the role of the structures, it does not provide a comprehensive picture of the plasmonic nanostructures themselves, and the extent to which variations in their physical parameters can be manipulated to provide a more optimum enhancement. This thesis, however, is novel in the fact that it provides a systematic and organized understanding of some of these correlations, and thus can enhance our understanding of how more efficient plasmonic solar cells can be built. Provided that the plasmonic nanostructures are well-designed over the scale of a wavelength of light, we show here that the optical absorption enhancements can occur when compare to structures with bare silicon substrate (with no plasmonic nanostructure coupled with it).

2.11 Finite-Difference-Time-Domain (FDTD) Algorithm and Methodology

The finite-difference time-domain (FDTD) method is arguably the simplest, both conceptually and in terms of implementation, of the full-wave techniques used to solve problems in electromagnetics [91]. It can accurately tackle a wide range of problems. However, as with all numerical methods, it does have its share of artifacts and the accuracy is contingent upon the implementation. The FDTD method can solve complicated problems, but it is generally computationally expensive. Solutions may require a large amount of memory, processing power and computation time. The FDTD method loosely fits into the category of "resonance region" techniques, i.e., ones in which the characteristic dimensions of the domain of interest are somewhere on the order of a wavelength in size. If an object is very small compared to a wavelength, quasi-static approximations generally provide more efficient solutions. Alternatively, if the wavelength is exceedingly small compared to the physical features of interest, ray-based methods or other techniques may provide a much more efficient way to solve the problem. The FDTD method employs finite differences as approximations to both the spatial and temporal derivatives that appear in Maxwell's equations.

The FDTD algorithm was first proposed by Kane Yee in 1966 and employs the algorithm that can be summarized as follows:

1. Replace all the derivatives in Maxwell's equations with finite differences. Discretize space and time so that the electric and magnetic fields are staggered in both space and time.
2. Solve the resulting difference equations to obtain "update equations" that express the

(unknown) future fields in terms of (known) past fields.

3. Evaluate the magnetic fields one time-step into the future so they are now known.

4. Evaluate the electric fields one time-step into the future so they are now known.

5. Repeat the previous two steps until the fields have been obtained over the desired duration.

A detailed explanation of the FDTD algorithm will be discussed in the next chapter.

2.12 FDTD Solutions and DEVICE

The solvers that we have used to simulate our photovoltaic cell systems are called FDTD Solutions and DEVICE, developed by Lumerical Solutions Inc. FDTD Solutions was used to accurately approximate the optical behavior and absorption calculations, while DEVICE has been used to generate the electrical activity i.e. short circuit current density (J_{SC}).

FDTD Solution is a high performance 3D FDTD-method solver for Maxwell's equations. These designs can range from simple planar geometries to very complex patterning, and can include a wide variety of materials such as organics and metals for the design, analysis and optimization of nanophotonic devices, processes and materials.

The result of the optical simulation is the spatial absorption in the substrate region, from which one can calculate the generation rate. Generation rate is defined as the number of electron- hole pairs generated at each point in the device due to the absorption of photons. This generation rate can be used in an electrical simulation in DEVICE to determine the responsivity and the photovoltaic efficiency of the solar cell. The CHARGE solver in DEVICE will account for the distribution of dopants that give rise to the built-in electric fields, the mobility of free carriers and the physical processes that result in the recombination of charge.

The interoperability of FDTD Solutions and DEVICE is illustrated in the following figure.

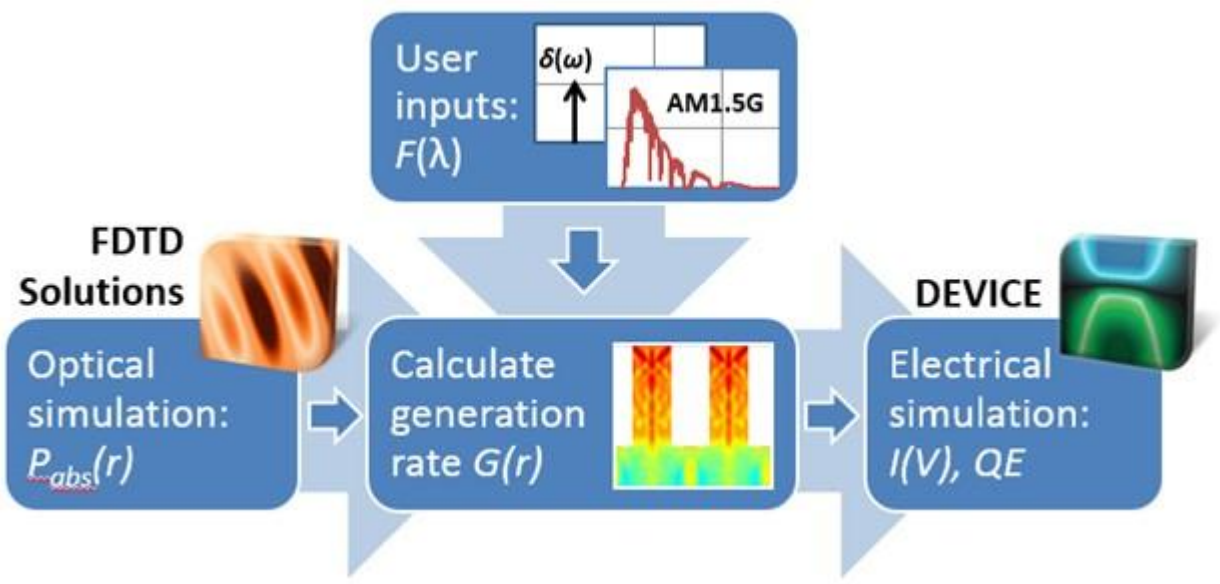

Figure 2. 35 Interoperability of FDTD Solutions and DEVICE

CHAPTER 3

FDTD ALGORITHM

The Finite-Difference Time-Domain (FDTD) method is one of the most common electromagnetic problem solving techniques today. It has been effectively implemented to a broad range of issues, such as scattering metal objects and dielectrics, antennas, micro-strip circuits, and electromagnetic absorption in the radiation exposed to human body. The primary reason for the FDTD method's success lies in the fact that the approach itself is incredibly easy, even for programming a three-dimensional code. The Chinese American applied mathematician Kane S. Yee, born 1934, first proposed the technique in 1966 [92] and then improved in the mid-70s by others.

The FDTD technique (finite difference methods) refers to the overall classification of grid-based differential numerical modeling methods. Using central-difference approximations to space and time partial derivatives, the time-dependent equations of Maxwell (in partial differential form) are discretized. The resulting finite-difference equations are solved in a leapfrog manner either in software or hardware: the components of the electric field vector in a volume of space are solved in time at a given time; then the components of the magnetic field vector in the same spatial volume are solved in time at the next instant; and the process is repeated time and again until the desired transient or steady-state electromagnetic field behavior is reached.

3.1 History

Finite difference schemes for time-dependent partial differential equations (PDEs) have been used in computational fluid dynamics problems for many years, along with the idea of using centered finite differential operators on staggered grids in space and time to achieve second-order precision [93]. The novelty of Kane Yee's FDTD scheme, described in his 1966 seminal paper [92], was to apply in Maxwell's curl equations centered finite difference operators on staggered grids in space and time for each component of the electrical and magnetic vector field. In 1980, Allen Taflove originated the descriptor "Finite-difference time-domain" and its corresponding "FDTD" acronym [94]. FDTD methods have appeared as

the primary tool of computationally design many scientific and engineering issues associated with interactions of electromagnetic waves with material structures since 1990. Current FDTD modeling applications range from near-DC (ultralow-frequency geophysics involving the entire Earth-ionosphere wave guide) to microwaves (radar signature technology, antennas, wireless communications devices, digital interconnections, biomedical imaging / treatment) and visible light (photonic crystals, nanoplasmics, solitons and biophotonics) [95]. An estimated 2,000 publications related to FDTD were published in the literature of science and engineering in 2006.

3.2 Theory

The theory associated on the fundamental of FDTD method is quite simple. In order to solve an electromagnetic problem, the idea is to simply discretize the Maxwell's equations with approximations of central difference, both in time and space. The originality of Yee's concept lies in allocating the components of the electrical and magnetic fields in space and marching in time for the application's evolution. FDTD solves Maxwell's curl equations in non-magnetic materials [96]:

$$\frac{\partial \vec{\boldsymbol{D}}}{\partial t} = \nabla \times \vec{\boldsymbol{H}} \tag{3.1}$$

$$\vec{\boldsymbol{D}}\,(\omega) = \varepsilon_o \varepsilon_r(\omega)\,\vec{\boldsymbol{E}}(\omega) \tag{3.2}$$

$$\frac{\partial \vec{\boldsymbol{H}}}{\partial t} = \frac{1}{\mu_0} \nabla \times \vec{\boldsymbol{E}} \tag{3.3}$$

where H, E, and D are the magnetic, electric, and displacement fields, respectively, while $\varepsilon_r(\omega)$ is the complex relative dielectric constant $\varepsilon_r(\omega) = n^2$, where n is the refractive index).

When Maxwell's differential equations are examined, it can be seen that the change in the E-field in time (the time derivative) is dependent on the change in the H-field across space (the curl). This results in the basic FDTD time-stepping relation that, at any point in space, the updated value of the E-field in time is dependent on the stored value of the E-field and the numerical curl of the local distribution of the H-field in space [92].

The H-field is time-stepped in a similar manner. At any point in space, the updated value

of the H-field in time is dependent on the stored value of the H-field and the numerical curl of the local distribution of the E-field in space. Iterating the E-field and H-field updates results in a marching-in-time process wherein sampled-data analogs of the continuous electromagnetic waves under consideration propagate in a numerical grid stored in the computer memory.

This description holds true for 1-D, 2-D, and 3-D FDTD techniques. When multiple dimensions are considered, calculating the numerical curl can become complicated. Kane Yee's seminal 1966 paper proposed spatially staggering the vector components of the E-field and H-field about rectangular unit cells of a Cartesian computational grid so that each E-field vector component is located midway between a pair of H-field vector components, and conversely [92]. This scheme, now known as a Yee lattice, has proven to be very robust, and remains at the core of many current FDTD software constructs.

The Yee algorithm centers its $\vec{E}$ and $\vec{H}$ field components in three-dimensional space so that every $\vec{E}$ component is surrounded by four circulating $\vec{H}$ components, and every $\vec{H}$ component is surrounded by four circulating $\vec{E}$ components. A diagram has been shown

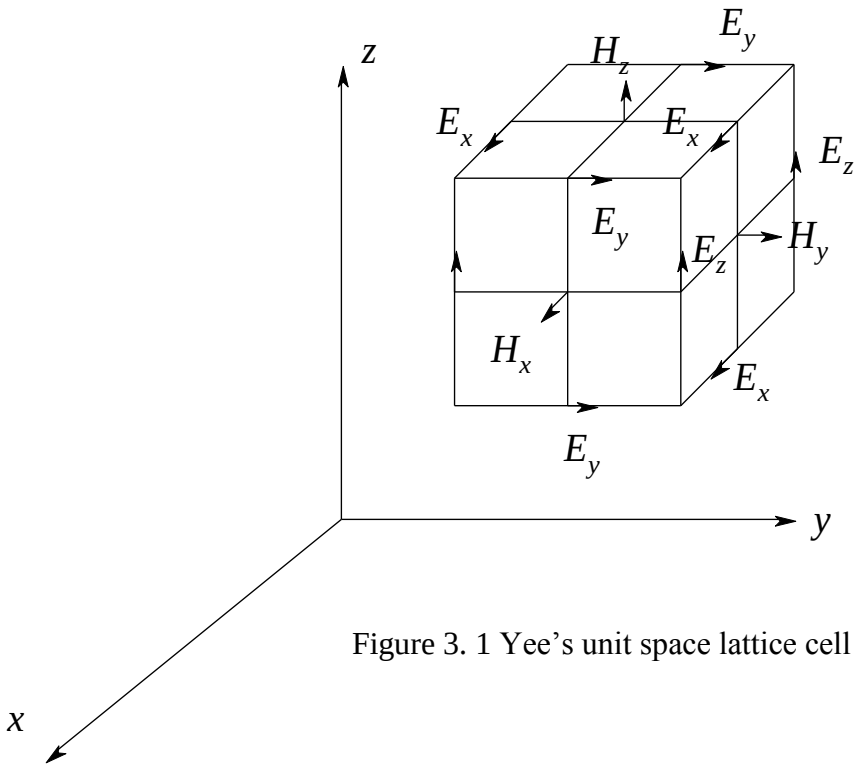

Figure 3. 1 Yee's unit space lattice cell

below [97]. The computational domain is divided into a number of rectangular unit cells.

Furthermore, Yee proposed a leapfrog scheme for marching in time wherein the E-field and H-field updates are staggered so that E-field updates are conducted midway during each time-step between successive H-field updates, and conversely. On the plus side, this explicit time-stepping scheme avoids the need to solve simultaneous equations, and furthermore yields dissipation-free numerical wave propagation. On the minus side, this scheme mandates an upper bound on the time-step to ensure numerical stability [98]. As a result, certain classes

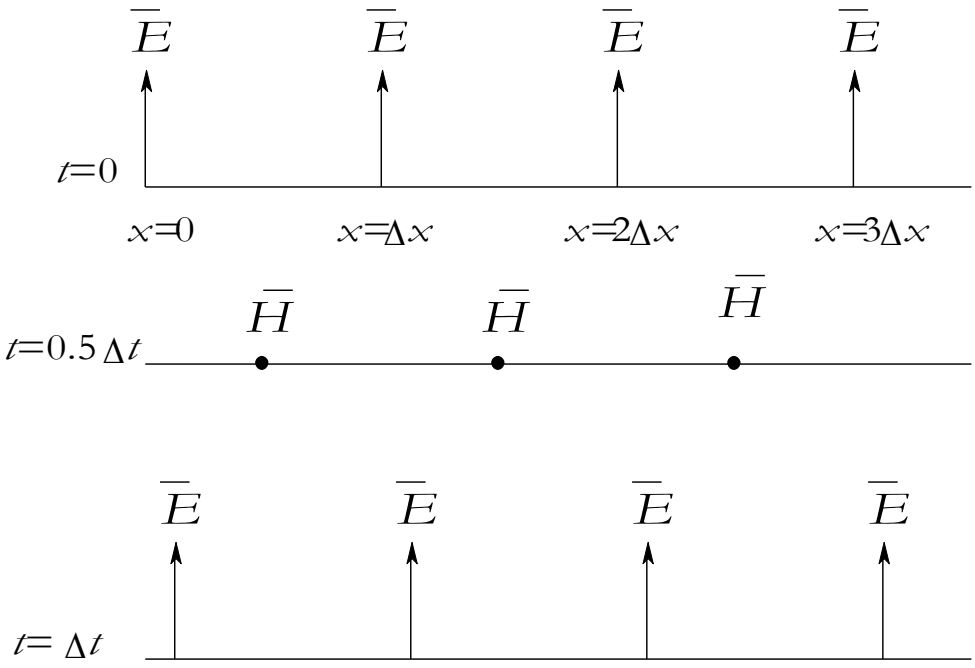

Figure 3. 2 According to Yee algorithm $\vec{E}$ and $\vec{H}$ field components are separated $\frac{\Delta t}{2}$ by in time.

of simulations can require many thousands of time-steps for completion.

As mentioned earlier, in three dimensions, Maxwell equations have six electromagnetic field components: Ex, Ey, Ez and Hx, Hy, and Hz. If it is assumed that the structure is infinite in the z dimension and that the fields are independent of z, specifically that [96]:

$$\varepsilon_r(\omega, x, y, z) = \varepsilon_r(\omega, x, y) \tag{3.4}$$

$$\frac{\partial \vec{E}}{\partial z} = \frac{\partial \vec{H}}{\partial z} = 0 \tag{3.5}$$

then Maxwell's equations split into two independent sets of equations composed of three vector quantities each which can be solved in the x-y plane only. These are termed the TE

(transverse electric), and TM (transverse magnetic) equations. The sets of equations can be solved with the following components:

TE: E_x, E_y, H_z

TM: H_x, H_y, E_z

The six scalar equations, expresses in coordinate systems are [99]:

$$\frac{\partial E_x}{\partial t} = \frac{1}{\varepsilon}\left(\frac{\partial H_z}{\partial y} - \frac{\partial H_y}{\partial z} - \sigma E_x\right) \tag{3.6}$$

$$\frac{\partial E_y}{\partial t} = \frac{1}{\varepsilon}\left(\frac{\partial H_x}{\partial z} - \frac{\partial H_z}{\partial x} - \sigma E_y\right) \tag{3.7}$$

$$\frac{\partial E_z}{\partial t} = \frac{1}{\varepsilon}\left(\frac{\partial H_y}{\partial x} - \frac{\partial H_x}{\partial y} - \sigma E_z\right) \tag{3.8}$$

$$\frac{\partial H_x}{\partial t} = \frac{1}{\mu}\left(\frac{\partial E_y}{\partial z} - \frac{\partial E_z}{\partial y}\right) \tag{3.9}$$

$$\frac{\partial H_y}{\partial t} = \frac{1}{\mu}\left(\frac{\partial E_z}{\partial x} - \frac{\partial E_x}{\partial z}\right) \tag{3.10}$$

$$\frac{\partial H_z}{\partial t} = \frac{1}{\mu}\left(\frac{\partial E_x}{\partial y} - \frac{\partial E_y}{\partial x}\right) \tag{3.11}$$

Now let's go deep into the FDTD algorithm and progress thoroughly from 1D to 3D algorithm.

3.2.1 1-D FDTD Algorithm

To begin with, for 1-D equations assume that all fields are uniform in y and x directions (i.e. d/dy =d/dx= 0)

1D- TE

$$\frac{\partial H_y}{\partial t} = -\frac{1}{\mu}\left(\frac{\partial E_x}{\partial z}\right) \tag{3.12}$$

$$\frac{\partial E_x}{\partial t} = -\frac{1}{\varepsilon}\left(\frac{\partial H_y}{\partial z} + \sigma E_x\right) \tag{3.13}$$

1D- TM

$$\frac{\partial H_x}{\partial t} = \frac{1}{\mu}\left(\frac{\partial E_y}{\partial z}\right) \qquad (3.14)$$

$$\frac{\partial E_y}{\partial t} = \frac{1}{\varepsilon}\left(\frac{\partial H_x}{\partial z} - \sigma E_y\right) \qquad (3.15)$$

Next, assuming that field values can only vary in the z-direction (i.e. all spatial derivatives in x and z direction are zero), Maxwell's Equations reduce to:

$$\frac{\partial H_y}{\partial t} = -\frac{1}{\mu}\left(\frac{\partial E_x}{\partial z}\right) \qquad (3.16)$$

$$\frac{\partial E_x}{\partial t} = -\frac{1}{\varepsilon}\left(\frac{\partial H_y}{\partial z} + \sigma E_x\right) \qquad (3.17)$$

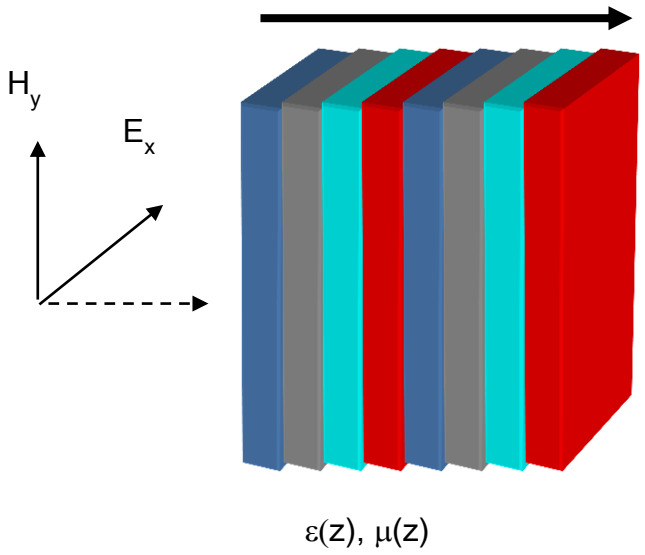

Figure 3. 3 Assuming that field values can only vary in the z-direction (i.e. all spatial derivatives in x and z direction are zero)

After replacing all continuous derivatives with finite differences and substitution of difference equations in above yields [99]:

$$\frac{H_y^{n+1}(i) - H_y^n(i)}{\Delta t} = -\frac{1}{\mu}\left(\frac{E_x^{n+1/2}(i+1/2) - E_x^{n+1/2}(i-1/2)}{\Delta z}\right) \qquad (3.18)$$

	$$\frac{E_x^{n+1/2}(i-1/2)-E_x^{n-1/2}(i-1/2)}{\Delta t}=-\frac{1}{\varepsilon}\left(\frac{H_y^n(i)-H_y^n(i-1)}{\Delta z}+\sigma\frac{E_x^{n+1/2}(i-1/2)+E_x^{n-1/2}(i-1/2)}{2}\right)$$	(3.19)

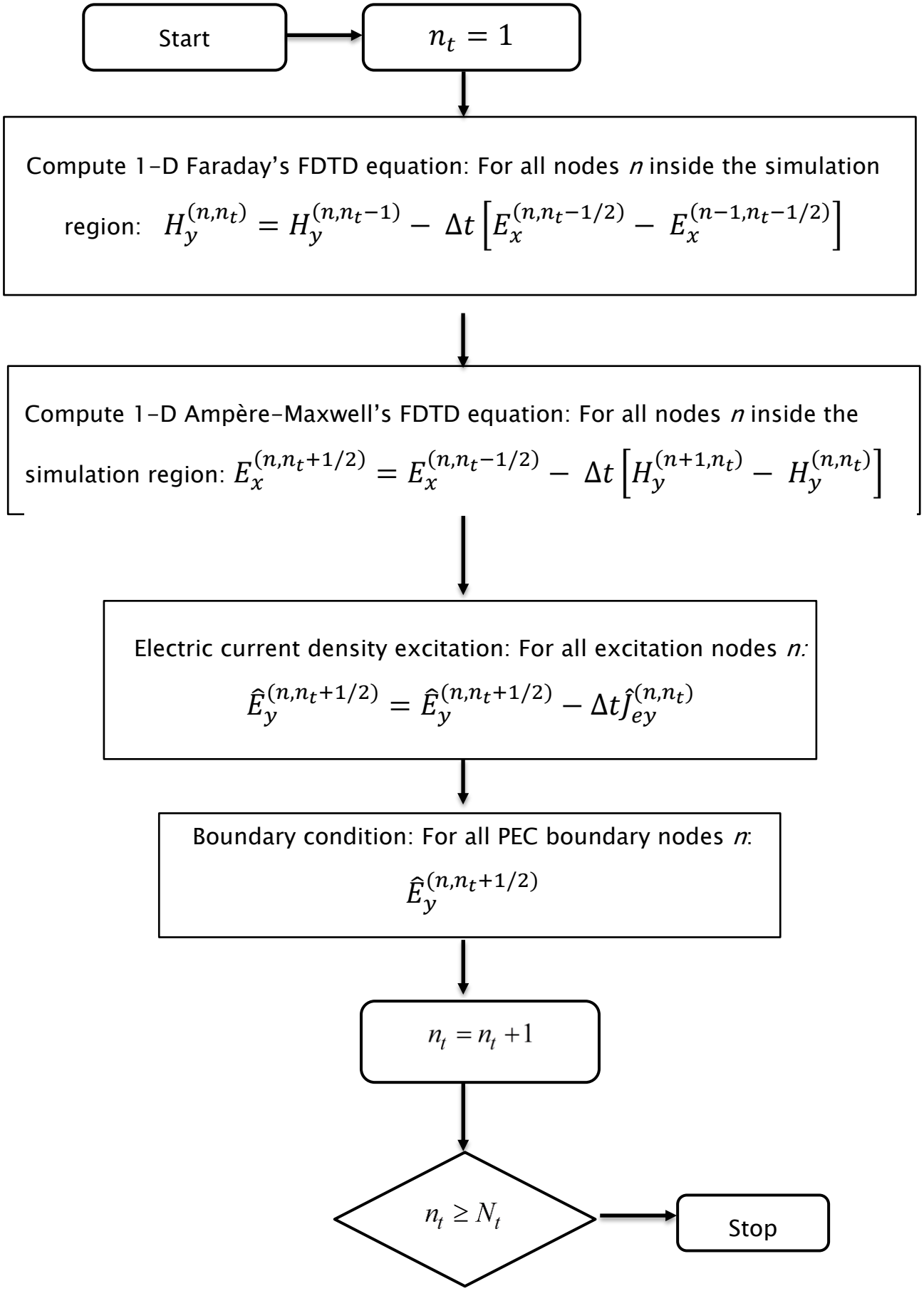

Figure 3. 4 1-D FDTD Algorithm Flow Chart

3.2.2 2-D FDTD Algorithm

Assuming that all fields are uniform in y direction (i.e. d/dy = 0) (all the equations are taken from [99]:

2D- TE

$$\frac{\partial H_y}{\partial t} = \frac{1}{\mu}\left(\frac{\partial E_z}{\partial x} - \frac{\partial E_x}{\partial z}\right) \qquad (3.20)$$

$$\frac{\partial E_x}{\partial t} = -\frac{1}{\varepsilon}\left(\frac{\partial H_y}{\partial z} + \sigma E_x\right) \qquad (3.21)$$

$$\frac{\partial E_z}{\partial t} = -\frac{1}{\varepsilon}\left(\frac{\partial H_y}{\partial x} - \sigma E_z\right) \qquad (3.22)$$

$$\frac{\partial H_x}{\partial t} = \frac{1}{\mu}\left(\frac{\partial E_y}{\partial z}\right) \qquad (3.23)$$

$$\frac{\partial H_z}{\partial t} = -\frac{1}{\mu}\left(\frac{\partial E_y}{\partial x}\right) \qquad (3.24)$$

$$\frac{\partial E_y}{\partial t} = \frac{1}{\varepsilon}\left(\frac{\partial H_x}{\partial z} - \frac{\partial H_z}{\partial x} - \sigma E_y\right) \qquad (3.25)$$

2D- TM

In the formulation of the two-dimensional FDTD, one can assume either TE (electric field is $\perp$ to the plane of incidence, or TM; magnetic field is $\perp$ to the plane of incidence).

This results from the fact that in 2D neither the fields nor the object contain any variations in the z-direction, consequently at $\frac{\partial}{\partial z} \to 0$

So in this context, Maxwell's Equations can be reduced to-

For TE polarization:

$$\nabla \times H = \varepsilon \frac{\partial E}{\partial t} + \varepsilon E \Rightarrow \frac{\partial E_z}{\partial t} = \frac{1}{\varepsilon}\left(\frac{\partial H_y}{\partial x} - \frac{\partial H_x}{\partial y} - \sigma E_z\right) \qquad (3.26)$$

$$\nabla \times E = \mu \frac{\partial H}{\partial t} \qquad (3.27)$$

$$\frac{\partial H_x}{\partial t} = -\frac{1}{\mu}\frac{\partial E_z}{\partial y} \qquad (3.28)$$

$$\frac{\partial H_y}{\partial t} = \frac{1}{\mu}\frac{\partial E_z}{\partial_x} \qquad (3.29)$$

$$\Rightarrow TE \quad polarization, \quad E_z \qquad (3.30)$$

For TM polarization:

$$\frac{\partial}{\partial t}E_x = \frac{1}{\varepsilon}\frac{\partial H_z}{\partial y} \tag{3.31}$$

$$\frac{\partial}{\partial t}E_y = \frac{1}{\varepsilon}\frac{\partial H_z}{\partial x} \tag{3.32}$$

$$\frac{\partial H_z}{\partial t} = \frac{1}{\mu}\left(\frac{\partial E_x}{\partial y} - \frac{\partial E_y}{\partial x}\right) \tag{3.33}$$

$$\Rightarrow TM \quad polarization, \; H_z \quad field \tag{3.34}$$

Applying the central difference expression, for TE mode:

$$H_x^{n+½}\left(i, j+\tfrac{1}{2}\right) = H_x^{n-½}\left(i, j+\tfrac{1}{2}\right) + \tilde{E}_z^n(i, j) - \tilde{E}_z^n(i, j+1) \tag{3.35}$$

$$H_y^{n+½}\left(i+\tfrac{1}{2}, j\right) = H_y^{n-½}\left(i+\tfrac{1}{2}, j\right) + \tilde{E}_z^n(i+1, j) - \tilde{E}_z^n(i, j) \tag{3.36}$$

$$\tilde{E}_z^{n+1}(i, j) = Ca(\mu)\tilde{E}_z^n(i, j) + Cb(\mu)\cdot\begin{bmatrix} H_y^{n+½}\left(i+\tfrac{1}{2}, j\right) - H_y^{n+½}\left(i-\tfrac{1}{2}, j\right) + H_x^{n+½}\left(i, j-\tfrac{1}{2}\right) \\ = H_x^{n+½}\left(i, j+\tfrac{1}{2}\right) \end{bmatrix} \tag{3.37}$$

For the TM case the equations are:

$$H_x^{n+½}\left(i+\tfrac{1}{2}, j+\tfrac{1}{2}\right) = H_x^{n-½}\left(i+\tfrac{1}{2}, j+\tfrac{1}{2}\right) + \tilde{E}_x^n(i+\tfrac{1}{2}, j+1) - \tilde{E}_x^n(i+\tfrac{1}{2}, j) + \tilde{E}_y^n(i, j+\tfrac{1}{2}) - \tilde{E}_y^n(i+1, j+\tfrac{1}{2}) \tag{3.38}$$

$$\tilde{E}_x^{n+1}(i+½, j) = Ca(\mu)\tilde{E}_x^n(i+½, j) + Cb(\mu)\cdot\begin{bmatrix} H_z^{n+½}\left(i+½, j+½\right) - \\ H_z^{n+½}\left(i+½, j-½\right) \end{bmatrix} \tag{3.39}$$

$$\tilde{E}_y^{n+1}(i, j+½) = Ca(\mu)\tilde{E}_y^n(i, j+½) + Cb(\mu)\cdot\begin{bmatrix} H_z^{n+½}\left(i-½, j+½\right) - \\ H_z^{n+½}\left(i+½, j+½\right) \end{bmatrix} \tag{3.40}$$

Numerical Dispersion 2D case. Using same procedure as for the 1D case it can be obtained:

$$\left[\frac{1}{c\Delta t}\sin\left(\frac{\omega\Delta t}{2}\right)\right]^2 = \left[\left(\frac{1}{\Delta x}\right)\sin\left(\frac{\tilde{k}_x\Delta x}{2}\right)\right]^2 + \left[\left(\frac{1}{\Delta y}\right)\sin\left(\frac{\tilde{k}_y\Delta y}{2}\right)\right]^2 \tag{3.41}$$

$$\left[\frac{\Delta s}{c\Delta t}\sin\left(\frac{\omega\Delta t}{2}\right)\right]^2 = \sin^2\left(\frac{\Delta s\cdot\tilde{k}\cdot\cos(\alpha)}{2}\right) + \sin^2\left(\frac{\Delta s\cdot\tilde{k}\cdot\sin(\alpha)}{2}\right) \tag{3.42}$$

$$\tilde{k}_x = \tilde{k}\cdot\cos(\alpha),\quad \tilde{k}_y = \tilde{k}\cdot\sin(\alpha) \tag{3.43}$$

3.2.2.1 *Steps of writing a 2D FDTD Program*

1. Defining physical constants
2. Defining program constants

E_0	magnitude of electric field
Δt	Change in time
Δx	Change in x
N_t	total # of time steps
N_x, N_y	# of nodes in the x, y direction

3. If using a pulse source, define Ez and Hx, or we can implement a hard source.
4. Start time marching nΔt, time value n = 1 : Nt
5. Increment the spatial index

➔First apply the absorbing boundary conditions

➔Apply the ABC along the edges of the computational region

3.2.3 3-D FDTD Algorithm

The 1D formulation involved 2 degrees of freedom (one field quantity E or H and one time variable). In 3D there are 4 degrees of freedom (3 in space and 1 in time). A space point in a uniform rectangular lattice is denoted as:

$$(i,j,k) = (i\Delta x, j\Delta y, k\Delta z) \tag{3.44}$$

Here Δx, Δy and Δz are the lattice space increments in the x, y, and z coordinate directions respectively and i, j, and k are integers. If any scalar function of space and time evaluated at a discrete point in the grid and at a discrete point in time is denoted by u, then;

$$u(i\Delta x, j\Delta y, k\Delta z, n\Delta t) = u^n_{i,j,k} \tag{3.45}$$

Using central, finite difference approximation in space, i.e. w.r.t. x:

$$\frac{\partial u}{\partial x}(i\Delta x, j\Delta y, k\Delta z, n\Delta t) = \frac{u^n_{i+1/2,j,k} - u^n_{i-1/2,j,k}}{\Delta x} + O((\Delta x)^2) \tag{3.46}$$

Using central, finite difference approximation in time:

$$\frac{\partial u}{\partial t}(i\Delta x, j\Delta y, k\Delta z, n\Delta t) = \frac{u^{n+1/2}_{i,j,k} - u^{n-1/2}_{i,j,k}}{\Delta x} + O\left[(\Delta x)^2\right] \tag{3.47}$$

The scalar equations from 3.6-3.11 are discretized as:

$$E^{n+1}_{x(i,j,k)} = \left(1 - \frac{\sigma(i,j,k)\Delta t}{\varepsilon(i,j,k)}\right) E^n_{x(i,j,k)} + \frac{\Delta t}{\varepsilon\Delta y}\left(H^{n+1/2}_{z(i,j+1,k)} - H^{n+1/2}_{z(i,j,k)}\right) - \frac{\Delta t}{\varepsilon\Delta z}\left(H^{n+1/2}_{y(i,j,k+1)} - H^{n+1/2}_{y(i,j,k)}\right) \tag{3.48}$$

$$E^{n+1}_{y(i,j,k)} = \left(1 - \frac{\sigma(i,j,k)\Delta t}{\varepsilon(i,j,k)}\right) E^n_{y(i,j,k)} + \frac{\Delta t}{\varepsilon\Delta z}\left(H^{n+1/2}_{x(i,j,k+1)} - H^{n+1/2}_{x(i,j,k)}\right) - \frac{\Delta t}{\varepsilon\Delta x}\left(H^{n+1/2}_{z(i+1,j,k)} - H^{n+1/2}_{z(i,j,k)}\right) \tag{3.49}$$

$$E^{n+1}_{z(i,j,k)} = \left(1 - \frac{\sigma(i,j,k)\Delta t}{\varepsilon(i,j,k)}\right) E^n_{z(i,j,k)} + \frac{\Delta t}{\varepsilon\Delta x}\left(H^{n+1/2}_{y(i+1,j,k)} - H^{n+1/2}_{y(i,j,k)}\right) - \frac{\Delta t}{\varepsilon\Delta y}\left(H^{n+1/2}_{x(i,j+1,k)} - H^{n+1/2}_{x(i,j,k)}\right) \tag{3.50}$$

$$H^{n+1/2}_{x(i,j,k)} = H^{n-1/2}_{x(i,j,k)} + \frac{\Delta t}{\mu\Delta z}\left(E^n_{y(i,j,k)} - E^n_{y(i,j,k-1)}\right) - \frac{\Delta t}{\mu\Delta y}\left(E^n_{z(i,j,k)} - E^n_{z(i,j-1,k)}\right) \tag{3.51}$$

$$H_{y(i,j,k)}^{n+1/2} = H_{y(i,j,k)}^{n-1/2} + \frac{\Delta t}{\mu \Delta x}\left(E_{z(i,j,k)}^{n} - E_{z(i-1,j,k)}^{n}\right) - \frac{\Delta t}{\mu \Delta z}\left(E_{x(i,j,k)}^{n} - E_{x(i,j,k-1)}^{n}\right) \quad (3.52)$$

$$H_{z(i,j,k)}^{n+1/2} = H_{z(i,j,k)}^{n-1/2} + \frac{\Delta t}{\mu \Delta y}\left(E_{x(i,j,k)}^{n} - E_{x(i,j-1,k)}^{n}\right) - \frac{\Delta t}{\mu \Delta x}\left(E_{y(i,j,k)}^{n} - E_{y(i-1,j,k)}^{n}\right) \quad (3.53)$$

3.2.3.1 *Steps for 3-D FDTD Algorithm*

- Step 1: Initialize the array elements. i. e. initialize $E_x, E_y, E_z, H_x, H_y, H_z$ to zero.
- Step 2: Update E_x, E_y, E_z fields by using the final values of H_x, H_y, H_z fields for the FDTD computational domain. For the 3D case each field component is calculated by using 3 nested loops separately.
- Step 3: Apply ABC's to calculate the field values on boundaries.
- Step 4: Apply the source condition to excite the system.
- Step 5: Update H_x, H_y, H_z fields by using the final values of E_x, E_y, E_z fields for the FDTD computational domain. For the 3D case each field component is calculated by using 3 nested loops separately.
- Step 6: Save field values for some points.
- Step 7: Repeat Step 2-Step 6 for n times. (n: number of time steps).

3.2.4 Basic FDTD Requirements

1. Space Cell Sizes:
    - Determination of the cell sizes and the time step size are very important aspects of the FDTD method. Cell sizes must be small enough to achieve accurate results at the highest frequency of interest and must be large enough to be handled by the computer resources.
    - The cell sizes must be much less than the smallest possible wavelength (which corresponds to the highest frequency of interest) to achieve accurate results.

- Usually the cell sizes are taken to be smaller than. $\lambda/10$

2. Time Step Size

   - The time step size, required for FDTD algorithm, has to be bounded relative to the space sizes. This bound is necessary to prevent numerical instability.

   - For a 3-Dimensional rectangular grid, with v the maximum velocity of propagation in any medium the following stability criterion is used:

$$v\Delta t \leq \frac{1}{\sqrt{\frac{1}{(\Delta x)^2}+\frac{1}{(\Delta y)^2}+\frac{1}{(\Delta z)^2}}} \tag{3.54}$$

3. Excitations

   - At t=0 all fields are assumed to be identically 0 throughout the computational domain.

   - The system can be excited either by using a single frequency excitation (i.e. sine wave) or a wideband frequency excitation (i.e. Gaussian Pulse).

3.2.5 Absolute Boundary Condition

In general EM analysis of scattering structures often requires the solution of "open region" problems. As a result of limited computational resources, it becomes necessary to truncate the computational domain in such a way as to make it appear infinite. This is achieved by enclosing the structure in a suitable output boundary that absorbs all outward traveling waves.

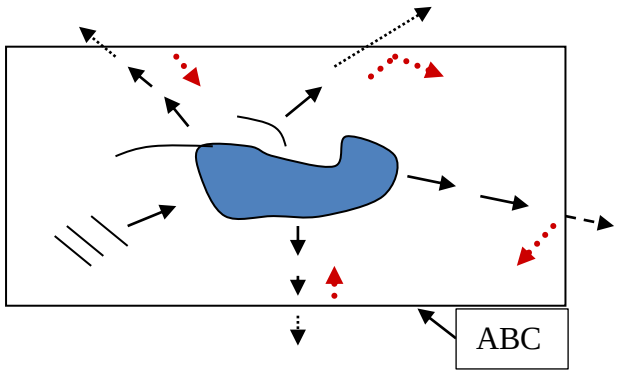

Figure 3. 5 Diagram of absolute boundary condition

3.2.5.1 *PML, Perfectly Matched Layer*

The PML method which was introduced in 1994 by Berenger, represents one of the most significant advances in FDTD development, since its conception in 1966, by Kane Yee.
The PML produces back reflection ~ 10^{-6} - 10^{-8} over a very broad range of incident.

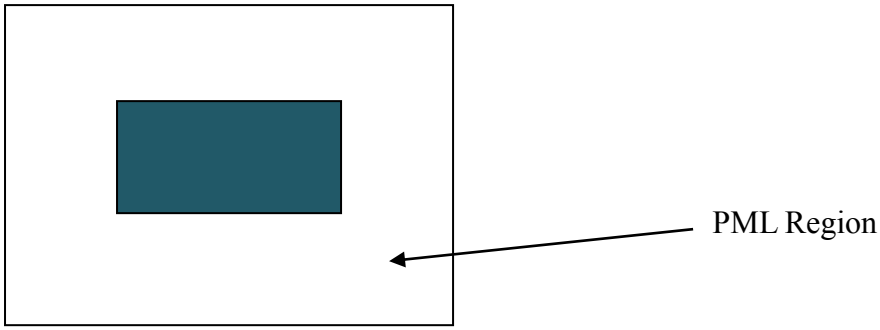

Figure 3. 6 PML Region

3.2.5.2 *Early ABC's*

When Yee first introduced the FDTD method, he used PEC boundary conditions [92]. This technique is not very useful in a general sense. It wasn't until the 70's when several alternative ABC's were introduced. However, these early ABC's suffered from large back reflections, which limited the efficacy of the FDTD method.

3.3 Strengths of FDTD Algorithm

- Every modeling technique has strengths and weaknesses, and the FDTD method is no different.
- FDTD is a versatile modeling technique used to solve Maxwell's equations. It is intuitive, so users can easily understand how to use it and know what to expect from a given model.
- FDTD is a time-domain technique, and when a broadband pulse (such as a Gaussian pulse) is used as the source, then the response of the system over a wide range of frequencies can be obtained with a single simulation. This is useful in applications where resonant frequencies are not exactly known, or anytime that a broadband result is desired.
- Since FDTD calculates the E and H fields everywhere in the computational domain as

they evolve in time, it lends itself to providing animated displays of the electromagnetic field movement through the model. This type of display is useful in understanding what is going on in the model, and to help ensure that the model is working correctly.

- The FDTD technique allows the user to specify the material at all points within the computational domain. A wide variety of linear and nonlinear dielectric and magnetic materials can be naturally and easily modeled.
- FDTD allows the effects of apertures to be determined directly. Shielding effects can be found, and the fields both inside and outside a structure can be found directly or indirectly.
- FDTD uses the E and H fields directly. Since most EMI/EMC modeling applications are interested in the E and H fields, it is convenient that no conversions must be made after the simulation has run to get these values.

3.4 Weaknesses of FDTD Algorithm

- Since FDTD requires that the entire computational domain be gridded, and the grid spatial discretization must be sufficiently fine to resolve both the smallest electromagnetic wavelength and the smallest geometrical feature in the model, very large computational domains can be developed, which results in very long solution times. Models with long, thin features, (like wires) are difficult to model in FDTD because of the excessively large computational domain required. Methods such as Eigenmode Expansion can offer a more efficient alternative as they do not require a fine grid along the z-direction [100].
- There is no way to determine unique values for permittivity and permeability at a material interface.
- Space and time steps must satisfy the CFL condition, or the leapfrog integration used to solve the partial differential equation is likely to become unstable.
- FDTD finds the E/H fields directly everywhere in the computational domain. If the field values at some distance are desired, it is likely that this distance will force the computational domain to be excessively large. Far-field extensions are available for

FDTD, but require some amount of post processing [95].

- Since FDTD simulations calculate the E and H fields at all points within the computational domain, the computational domain must be finite to permit its residence in the computer memory. In many cases this is achieved by inserting artificial boundaries into the simulation space. Care must be taken to minimize errors introduced by such boundaries. There are a number of available highly effective absorbing boundary conditions (ABCs) to simulate an infinite unbounded computational domain [95]. Most modern FDTD implementations instead use a special absorbing "material", called a perfectly matched layer (PML) to implement absorbing boundaries [101], [102].
- Because FDTD is solved by propagating the fields forward in the time domain, the electromagnetic time response of the medium must be modeled explicitly. For an arbitrary response, this involves a computationally expensive time convolution, although in most cases the time response of the medium (or Dispersion (optics)) can be adequately and simply modeled using either the recursive convolution (RC) technique, the auxiliary differential equation (ADE) technique, or the Z-transform technique. An alternative way of solving Maxwell's equations that can treat arbitrary dispersion easily is the Pseudospectral Spatial-Domain method (PSSD), which instead propagates the fields forward in space.

CHAPTER 4
RESEARCH METHODOLOGY

4.1 Simulation Setup

The simulations performed were done using the solvers – (i) FDTD Solutions [103], a commercial-grade simulator that uses the finite-difference time-domain method to perform the calculations, for the optical enhancement analysis and calculation of short circuit current density (Jsc), while (ii) CHARGE (DEVICE) [104], a commercial-grade simulator Eigen mode solver and propagator, was used for the electrical analysis. Both FDTD and DEVICE were developed by Lumerical Inc. The analyses were performed under standard solar conditions of incident radiation intensity of 1000 W/m^2, temperature of 25 °C, and a solar spectral irradiance of AM1.5G [70].

The computer system used to perform the simulations had the following specifications:

- Operating system: Windows 7
- Processor: Intel(R) Core(TM) i7-4770 CPU @ 3.40GHz
- Memory: 8192MB RAM
- GPU: Intel(R) HD Graphics 4600

To improve the efficiency of thin-film solar cells, the essential physical parameters were taken into account. For a sufficient amount of data and to infer an acceptable conclusion, eight different pitches (side-side inter-particle distance between neighboring nanospheres) of 10 nm, 20 nm, 50 nm, 80 nm, 100 nm, 150 nm and 200 nm, respectively, were chosen for each of the substrate. The nanoparticles were placed on top of the solar cells in a periodic array as illustrated in Figure 2.32 and 2.33**.** The substrates were designed with a thickness of 2μm to get the best results. The detailed analyses performed has been broken down and presented in seven major sections: (a) plasmonic resonance analysis of silver (Ag) nanoparticle, (b) optical absorption enhancement analysis of the PV cell, (c) short circuit current density (J_{SC}) analysis, (d) open circuit voltage (V_{OC}), (e) power (P), (f) Fill Factor (F)

and (g) Optical near-field enhancement analysis.

4.2 Plasmonic Resonance for Silver (Ag)

Before the analysis was initiated, it was necessary to identify the physical parameters that were of interest. To that end, Choudhury *at el.* studied the metals silver (Ag), gold (Au) and aluminum (Al). [15]–[17] and they had also analyzed the result. This was done on the basis of studies that have been previously made to analyze the plasmonic properties of all metals, and found these to demonstrate resonance within the solar spectral range. The diameters that were chose were D = 50nm, D = 100nm and D = 200nm as it was deduced that this would provide a sufficient amount of data to reach a proper conclusion regarding the correlation between the variation in diameter of the nanoparticles and the optical absorption enhancement of the photovoltaic cell. Furthermore, two pitches (distance between successive particles, center-center) of 300nm and 220nm were chosen. This was also done so on the basis of the understanding that these pitches would provide a sufficient outlook on the dependence on the pitch of the nanoparticle array's ability to enhance the solar cell efficiency.

The first task was to observe and analyze the plasmon resonance phenomenon of each metal nanoparticle before it was placed over the Si substrate, and identify the wavelength range where the resonance of each nanoparticle occurred. Thus, it was chosen to calculate the extinction, scattering and absorption spectra for each nanoparticle. For that, the metal nanoparticle of interest was placed inside the simulation region, and a total field scattered

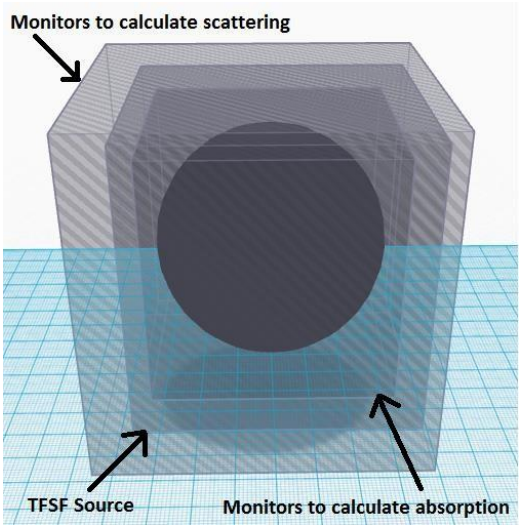

Figure 4. 1 Plasmonic resonance analysis setup

field (TFSF) source was directed towards it from all directions. The TFSF source would take both the complete field of the incident radiation and the scattered field from the metal nanoparticle into account. Field monitors were placed close to the particle to measure absorption, and outside the particle beyond the source to measure scattering. The extinction spectrum was generated by adding these two quantities. This setup is illustrated in Figure 4.1.

Total Field Scattered Field (TFSF) Source

Total-field scattered-field sources are used to separate the computation region into two distinct regions – one contains the total field (i.e. the sum of the incident field and the scattered field), while the second region contains only the scattered field [91]. The incident field is a plane wave with a wave vector normal to injection surface. This source type is particularly useful to study the scattering behavior of objects, as the scattered field can be isolated from the incident field. Thus we have utilized this source to observe and analyze the plasmonic resonance phenomena for each metal nanoparticle of each respective diameter.

For the initial simulation, the extinction spectra of Ag, Au and Al plasmonic metal nanoparticles of diameters D = 50nm, D = 100nm and D = 200nm, respectively, were generated and analyzed. The particles were separately and individually placed inside the simulation region (shown in Figure 3.1), and the absorption, scattering and extinction spectra were obtained using the appropriately placed monitors as has been shown previously in Figure 3.1. The analysis was done across a wide wavelength range of λ = 300nm to 1100nm for Ag and Au nanoparticles, and λ = 200nm to 1100 nm for Al nanoparticles as it is known that Al demonstrates resonance on the bluer region of the spectrum. The resultant spectra for each nanoparticle is analyzed over the course of the next few pages.

It can be seen from the graphs in Figure 3.2 for each respective Ag nanoparticle diameter that there is clearly a resonance peak occurring within a particular wavelength range. While the extinction spectra peak value remains almost the same for increasing the diameters (with

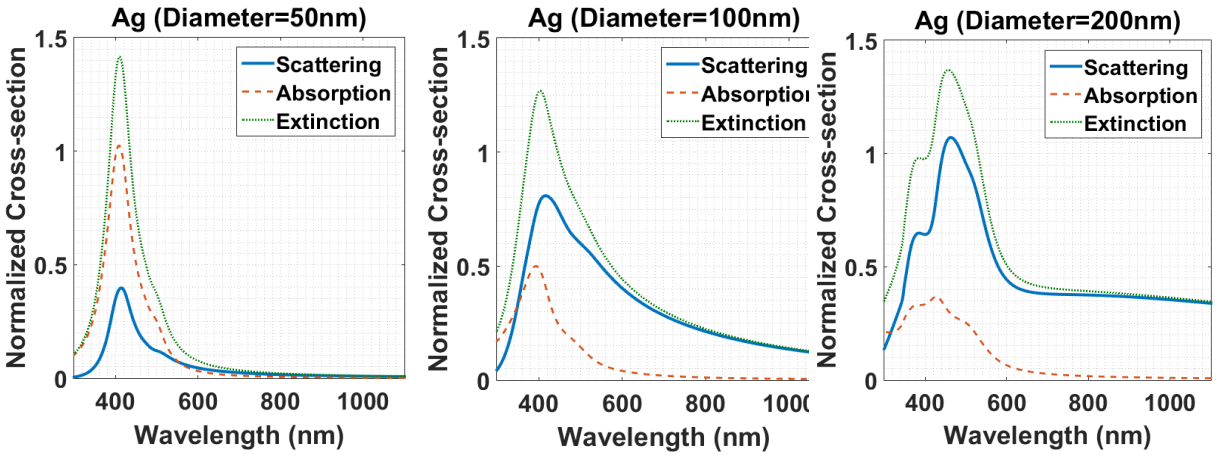

Figure 4. 2 Absorption, scattering and extinction spectra for (a) Ag nanoparticle of D = 50nm, (b) Ag nanoparticle of D = 100nm, and (c) Ag nanoparticle of D = 200nm

a slight red-shift for increasing nanoparticle size), the same cannot be said for the absorption and scattering graphs. It is clearly seen that for higher diameters, the magnitude of the resonant peak of the absorption graph decreases while that of the scattering graph increases. This is in agreement with the results of previous studies [76], [80], [81]. Furthermore, the peak of the extinction, scattering and absorption spectra shifts to towards the higher wavelength side of the spectra for increasing diameter. Overall the peak always lies within the wavelength range of 400nm to 500nm.

4.3 Optical Absorption Enhancement

The next analysis which comes into play is the optical absorption enhancement analysis. This thesis was performed by placing a square array of 100 nm diameter silver(Ag) nanospheres periodically on top of the silicon (Si) ,gallium arsenide (GaAs) and cadmium telluride-cadmium sulfide (CdTe-CdS) substrates and organic (P3HT:PCBM) solar substrate, respectively, and then a plane wave was directed perpendicularly towards the PV cell. The incident plane wave had the electric field oriented along the x-axis and the propagation vector was along the z-axis. The monitors were placed immediately over the metal nanosphere substrate, and 0.5μm below the nanosphere- Si interface, respectively. By subtracting the power values of the upper monitors from the lower monitors, the absorption within the solar cell was calculated. For each of the substrate, the optical enhancement within the cell was analyzed. The diagram for the setup has been shown in Figure 4.3. To analyze the optical enhancement, a quantity (g) was defined that is the optical absorption enhancement factor. The formula for the optical absorption enhancement factor is as follows:

$$g = \frac{Absorption\ across\ the\ substrate\ with\ metal\ nanoparticles}{Absorption\ across\ the\ bare\ substrate} \qquad (4.1)$$

The diameter of the silver (Ag) nanosphere were kept constant at 100 nm while the inter-particle distance or pitch (side-side) was varied (pitch = 10 nm, 20 nm, 50 nm, 80 nm, 100 nm, 120 nm, 150 nm and 200 nm) to generate the optical absorption enhancement graphs of the Si, GaAs, CdTe-CdS and OSC. The wavelength range was set to 400 nm to 1100 nm for silicon and gallium arsenide, whereas for cadmium telluride and OSC the wavelength was from 300nm to 1100nm throughout the simulation.

For silicon, the material was directly selected from the FDTD solver. For gallium arsenide the same method was followed. But for the case of cadmium telluride-cadmium sulfide, the materials were imported into the solver. From the Figure 4.3 (c) it can be seen that for CdTe-CdS substrate, as the name suggests, two types of materials were used- cadmium telluride which is the p-doped absorber layer and cadmium sulfide is the n-doped window layer. These two types of materials were imported using their refractive indices [105].For the OSC, the bulk heterojunction blend, poly-3-hexylthiophene/[6,6]-phenyl-C61-butyric acid methyl ester (P3HT:PCBM) are used as a photoactive layer and aluminum was used as back contact. Figure 4.4 shows the cross-section of OSC structure used for this thesis [106].

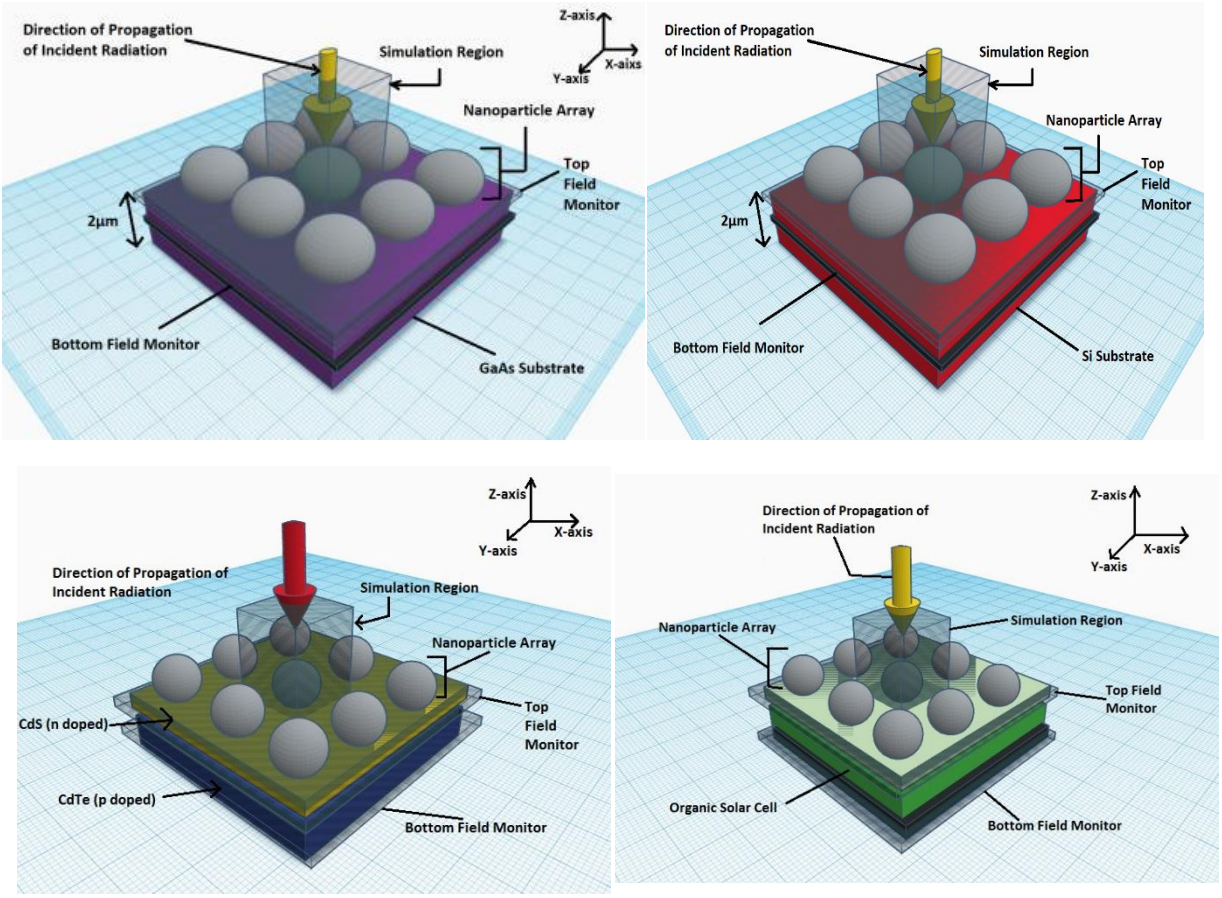

Figure 4. 4 Simulation Setup for the optical absorption enhancement analysis (a) GaAs substrate (b) Silicon substrate (c) CdTe-CdS solar cell (d) organic solar cell

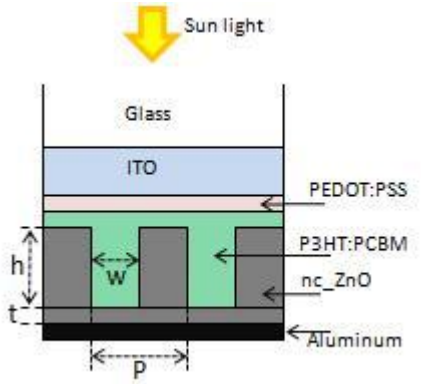

Figure 4. 3 Organic solar cell structure

4.4 Short Circuit Current Density (J_{sc})

It is to be noted that any enhancement in optical absorption might not cause a corresponding proportionate increase in electrical activity of the photovoltaic cell. This may be because of a number of reasons, including the fact that not all incident photons from the sunlight's radiation is able to generate an electron-hole pair as the photon does not have enough energy to cover the band-gap energy. Even if the energy is sufficient, the excess energy provided by the photon to the electron is used to navigate through the substrate, and this energy may not be enough to cover the entire path, and thus may result in the electron recombining with another hole. Although the use of thin-film does significantly reduce this required diffusion length for the electron to travel, the presence of less semiconductor material means that the number of possible electron-hole pairs generated may be lower than that of thick-film solar cells. Thus any analysis of nanostructured solar cells must be accompanied by a current generation analysis to find the extent to which the optical absorption enhancement has translated in to electrical activity improvement.

To that end, short circuit current density (J_{SC}) was chosen to be calculated for each configuration of plasmonic nanoparticle arrays studied. While the solver FDTD Solutions is able to calculate an approximation for J_{SC}, it however provides an overestimation as its calculations are entirely based on the optical data generated, and does not take the minority carrier diffusion length, time and the extent of recombination for amorphous silicon into account. Hence, the J_{SC} data is generated using the DEVICE solver, as it considers all of the above in its calculations, and also takes the presence of the electrodes (contacts) into consideration.

It should also be noted that the CHARGE solver in DEVICE was designed for crystalline semiconductors and it uses a specific type of energy band profile (DOS) to model the semiconductors. The band profile of organic materials are quite different from that of a crystalline material, also the scattering mechanisms are much more complicated which cannot be modeled with the scattering models available in DEVICE. Therefore, unfortunately the J_{SC} calculation could not be done using the DEVICE solver as it was not possible to model electrical transport in organic materials using the CHARGE solver. So, the electrical calculation of the OSC could not be done . For this reason $J_{SC,}$ $V_{OC,}$ output power and fill factor of the OSC could not be calculated.

For each configuration (except OSC) of silver (Ag) nanoparticle array on both the

silicon(Si), gallium arsenide (GaAs) and cadmium telluride-cadmium sulfide (CdTe-CdS) substrates, the electrical enhancement- which is one of the analysis to be made- was then calculated by the short circuit current density (J_{SC}) and compared with the J_{SC} of the bare substrate, respectively.

The following outlines the procedure to generate J_{SC} data:

- In the simulation region of the designed solar cell in FDTD Solutions, place a 'Solar Generation Rate' analysis unit.
- Run the simulation. The solar generation rate analysis unit calculates the number of electron-hole pairs created per photon, and transfers this data to a MATLAB data file.
- Run the simulation, and record the J_{SC} for that specific design. Repeat this for all configurations.
- Open DEVICE, copy the solar cell design over, and import the MATLAB file containing the solar generation rate data.

Figure 4.5 shows the setup for the short circuit current density. For the GaAs and CdTe-

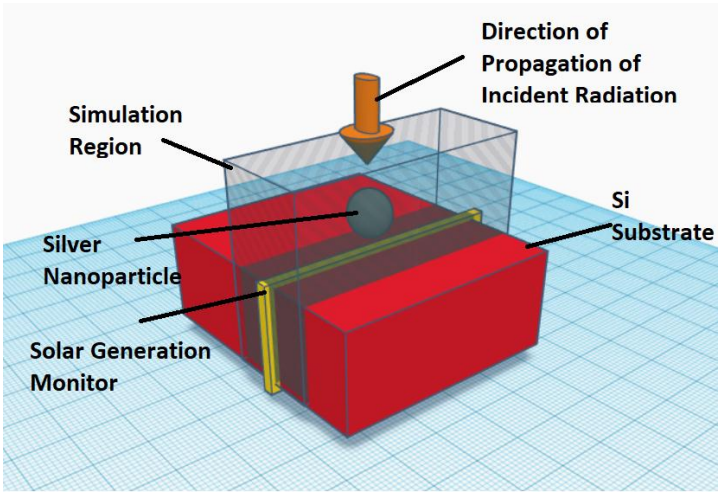

Figure 4. 5 Simulation setup for Jsc calculation (in silicon substrate)

CdS solar cells the same procedure was followed. These cartoon figures were created with Tinkercad [107].

4.5 Open Circuit Voltage (V_{OC})

The open circuit voltage (V_{OC}) was calculated by creating the exact models of the Ag nanoparticles on top of the substrates in the solver CHARGE (DEVICE). It is done by calculating the solar generation rate in the FDTD solver using an analyzing unit. Then this data was fed to the solver CHARGE (DEVICE). A script file was then run which calculates the open circuit voltage (V_{OC}).

4.6 Output Power (P)

After J_{SC} and V_{OC}, the maximum power absorbed by the PV cell was calculated. The formula for power was used in the script file in the CHARGE solver i.e. (*P*) is [37]:

$$P = Jsc \times total\ surface\ area(substrate) \times Voc \tag{4.2}$$

4.7 Fill Factor (FF)

It is a very well-known fact that the open circuit voltage and the short circuit current are considered to be the maximum voltage and current from a solar cell. However at these maximum points the power of the solar cell is zero. Fill Factor or more commonly known as "FF" is a parameter which, in conjunction with V_{OC} and short-circuit current (I_{SC}), determines the maximum power from a solar cell. The FF is defined as the ratio of the maximum power from the solar cell to the product of V_{OC} and I_{SC} [37].

$$FF = \frac{P_{max}}{Jsc \times Voc} \tag{4.3}$$

This is how the ratio of the maximum obtainable power "FF" is calculated.

4.8 Near Field Enhancement

Finally, the near field images of each set up was generated to examine the interaction of incident electromagnetic field with the plasmonic nanoparticles and the surface of the PV cell. This result was obtained by placing an electric field monitor on the vertical cross-section of the model. The near field images allows a correlation to be made of the optical and electrical enhancements with the enhancement in electromagnetic fields in the immediate vicinity of the plasmonic nanoparticles and the PV substrate. First, the approximate wavelength at which the nanoparticles of Ag, displayed surface plasmon resonance had to be identified. This was found to be wavelengths of approximately $\lambda \sim 460$nm for Ag.

In order to generate these images, a field monitor was placed along the x-z plane cross-section of one unit of the cell, i.e. the substrate with one plasmonic nanoparticle placed on top, as shown in Figure. The data from the monitor was then pinched to remove all the singleton dimensions out, and then transferred to a MATLAB data file for post-processing. In MATLAB, the data file was then used to generate the respective images.

For the enhancement image, the color scale is in the log scale, and hence the areas which are dark red in color have an enhancement of over 1 in the log scale that corresponds to near-field enhancement of over ×10 (over 10 fold). For each set of the optical near-field images for the different nanoparticle configurations generated and illustrated below, an appropriate set of images have been provided to allow for proper analysis of each structure.

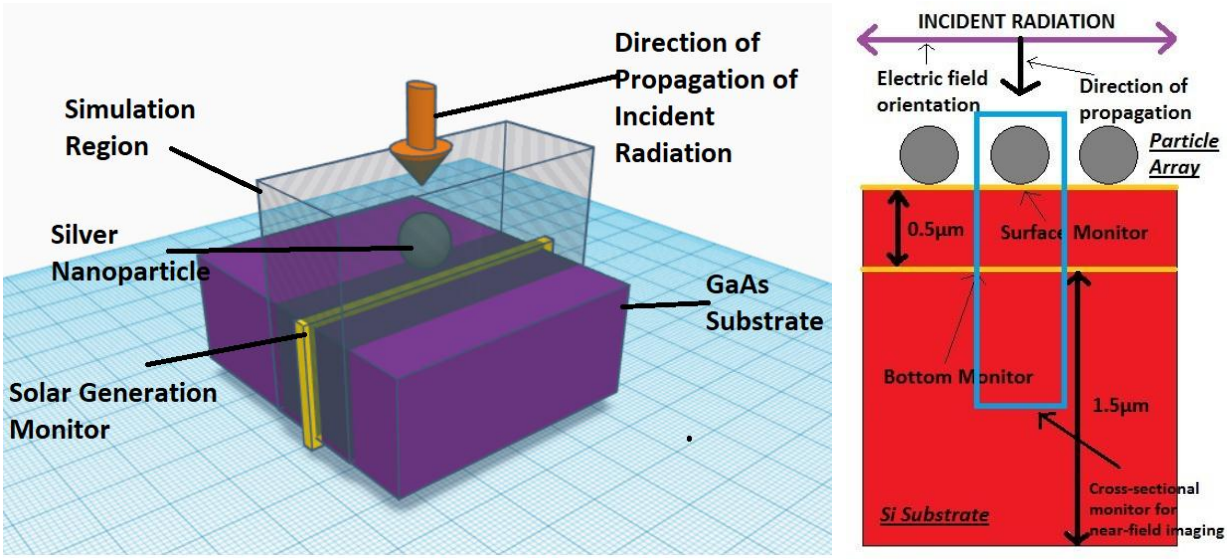

Figure 4. 6 Setup for near-field enhancement analysis (a) in gallium arsenide substrate (b) cross section of the setup

The interaction between the plasmonic metal nanoparticles and silicon (Si), gallium arsenide (GaAs), cadmium telluride-cadmium sulfide (CdTe-CdS) and organic solar substrates can also be seen using the NF images. The same setup was used for each of the solar cell substrates. The images have been shown and analyzed in the results and discussions chapter.

CHAPTER 5

RESULTS AND DISCUSSION

5.1 Optical Absorption Enhancement Analysis

For the optical absorption enhancement analysis, the simulation was setup as was previously shown. In order to ensure that the effect of the change in one parameter does not distort the data obtained for the observed variation in another parameter, only one parameter was changed at a time while the others were kept constant. This will allow the obtained results to be more rigid and precise, and that in turn should make the final conclusions more credible.

The metal is kept constant with a diameter of 100nm while the pitch (side-side distance between spheres) of the nanoparticles periodically dispersed on top are varied, and the optical absorption enhancement factor (g) for each configuration is calculated across their respective incident radiation spectra. This is repeated for all four of the substrates.

The obtained optical absorption enhancement data is then extracted as a MATLAB data file for post- processing. All of the graphs were generated using MATLAB. In each of the graph, 8 curves of different pitch values are illustrated. The results are shown in the following pages. The highest values of total optical absorption enhancement factor have been highlighted in bold font.

Table 5. 1 Total Optical absorption enhancement Factor

	Ag(λ=400nm-1100nm)		Ag(λ=300nm-1100nm)	
Pitch	Si Substrate	GaAs Substrate	CdTe-CdS Substrate	Organic Substrate
10nm	100.91	99.03	49.9	**166.39**
20nm	147.36	144.83	72.96	160.20
50nm	187.45	184.54	101.33	154.47
80nm	**192.69**	**190.48**	113.49	152.76
100nm	191.77	190.17	119.37	152.22

120nm	189.79	188.80	124.37	151.93
150nm	186.33	186.09	130.58	151.73
200nm	180.9	181.49	**138.26**	151.62

The setup for the optical absorption enhancement was shown in Figure 3.3. Silver (Ag) nanosphere of 100nm diameter was used throughout the analyses. The variable was the pitch length i. e is the side to side distance between the particles. Pitch values of 10nm, 20 nm, 50 nm, 80 nm, 100 nm, 150 nm and 200 nm were used. The optical absorption enhancement factor (g) for each configuration of the solar cells is calculated in the wide radiation spectra (400 nm - 1100 nm) for silicon and gallium arsenide solar cells and (300 nm - 1100 nm) for the cadmium telluride-cadmium sulfide and OSCs. The graphs for the wavelength-resolved

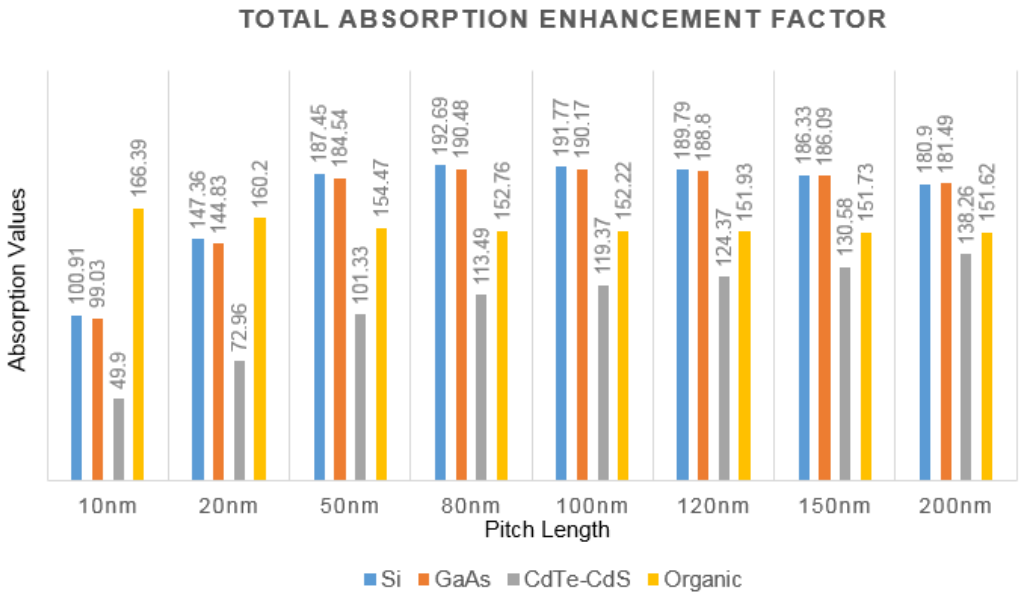

Figure 5. 1 Excel plot for Total Absorption Enhancement Factor

optical absorption enhancement for each of the substrates are shown in Figure 4.1-4.4, and the total optical absorption enhancement factor (sum of the individual g values at each wavelength sampled from 300-1100nm) are shown in Table 5.1. The data are also plotted in Figure 5.1.

In the case of silicon, from the table it can be seen that there is an increasing trend in the total optical absorption enhancement factor (g) from 10 nm pitch to 80 nm pitch such as the gallium arsenide values. There is a peak value 192.69 at 80 nm pitch and after 80 nm pitch, the g values have decreasing trend. The peak value shows the absorption is approximately 193 times greater when the nanoparticles are placed on top of the silicon, than that of the bare Si wafer. For 200 nm pitch the optical absorption enhancement value is approximately 180 times more than the bare silicon. From the graph, it can be observed that the highest g value is around λ= 450nm for the pitch value 80nm which follows the same trend as the total optical absorption enhancement as described earlier.

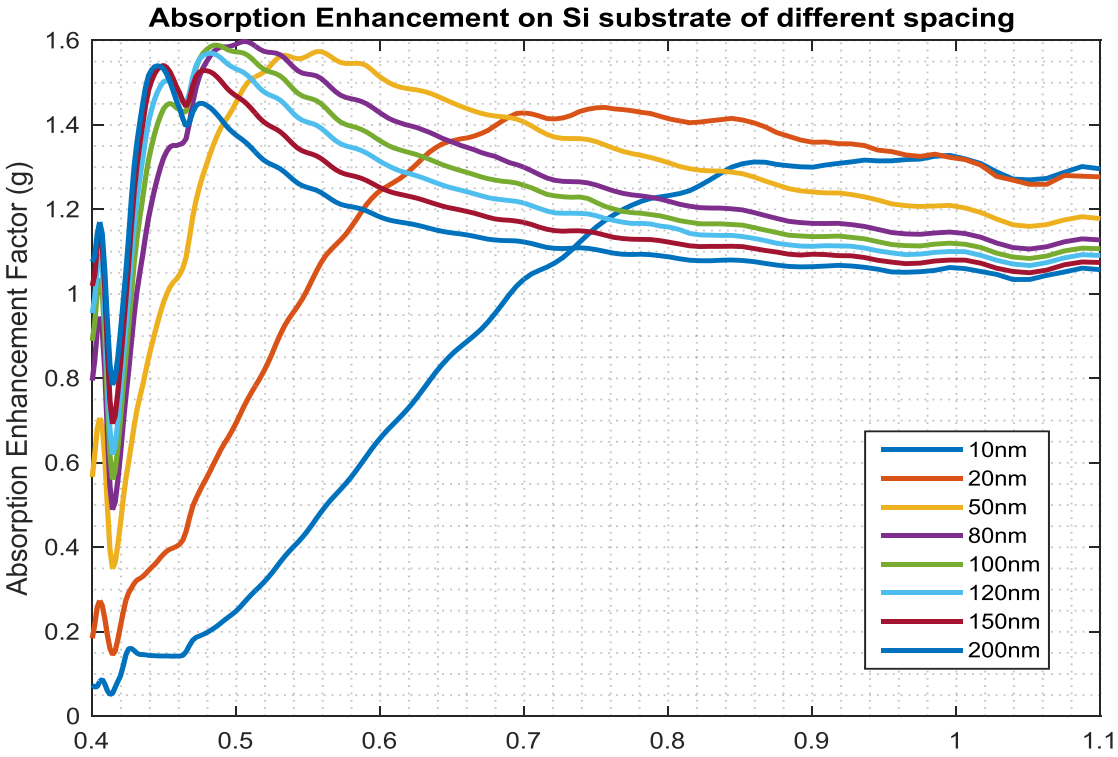

Figure 5. 2 Wavelength-resolved optical absorption enhancement for Silicon plasmonic solar cells (λ= 0.4um-1.1um)

For gallium arsenide, the total optical absorption enhancement factor has a trend of increasing up to 80nm pitch value and then decreasing from there. A pattern which is similar to a ring-bell curve having a maximum value in the curve in relation to the pitch value. The values from the table also show that the lowest value 99.03 is for 10nm pitch value. When it comes to the graphical representation, the highest g value is for 200nm pitch at around λ= 440nm. But in the contrary the total absorption value is less for 200nm pitch which means that the individual g values were not more than 80nm pitch.

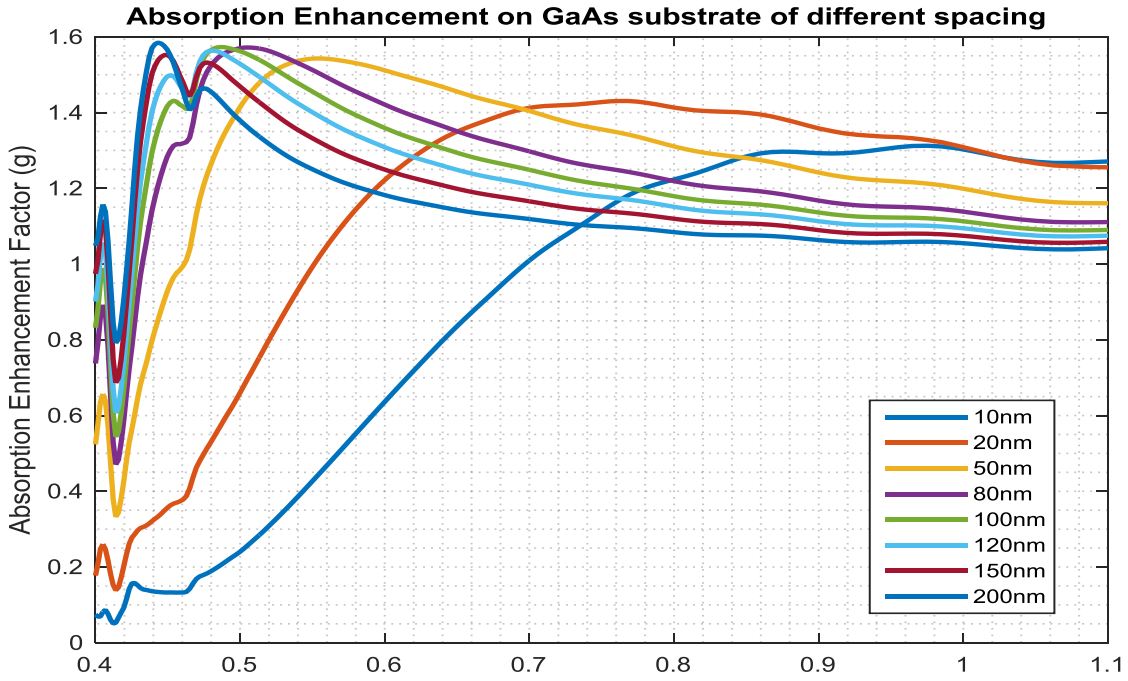

Figure 5. 3 Wavelength (um)-resolved optical absorption enhancement for gallium arsenide plasmonic solar cells (λ= 0.4um-1.1um)

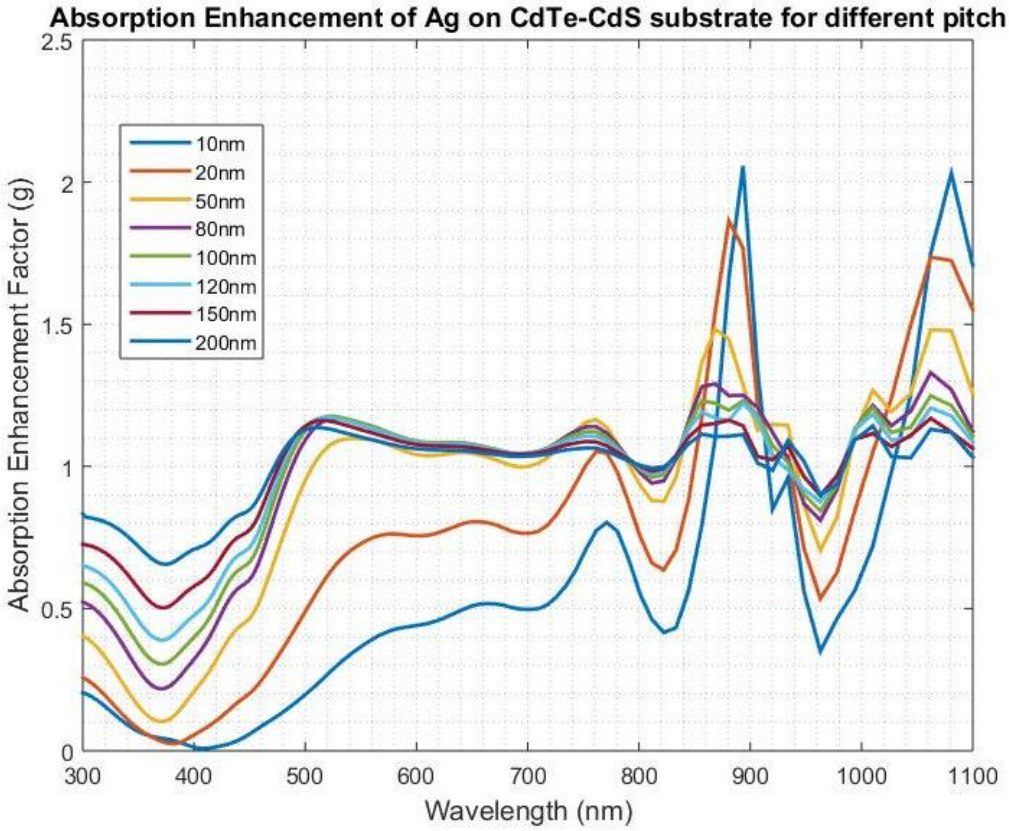

Figure 5. 4 Wavelength (nm)-resolved optical absorption enhancement for cadmium telluride-cadmium sulfide plasmonic solar cells (λ= 300nm-1100nm)

Cadmium telluride-cadmium sulfide is a heterojunction solar cell. For the optical absorption enhancement results, nanoparticles were deposited on top of this solar cell. Unlike the previous two types of solar cells, this one shows only an increasing trend in the g values for 10nm to 200nm pitch values. The lowest is 49.9 for 10nm pitch and the highest 138.26 for 200nm. The graphs for the optical absorption enhancement factor also show an increasing trend in the g values as the pitch length increases. For all the pitch lengths there were sharp spikes of g values near the λ= 890nm and 1080nm region. The graphical values coincide with the values of the total absorption values from the table. As the goal of this thesis is to enhance the absorption factor so as to increase the optical efficiency, this solar cell meets the requirement in the optical analysis. It should be noted that the individual g values at the peaks are more than silicon and gallium arsenide.

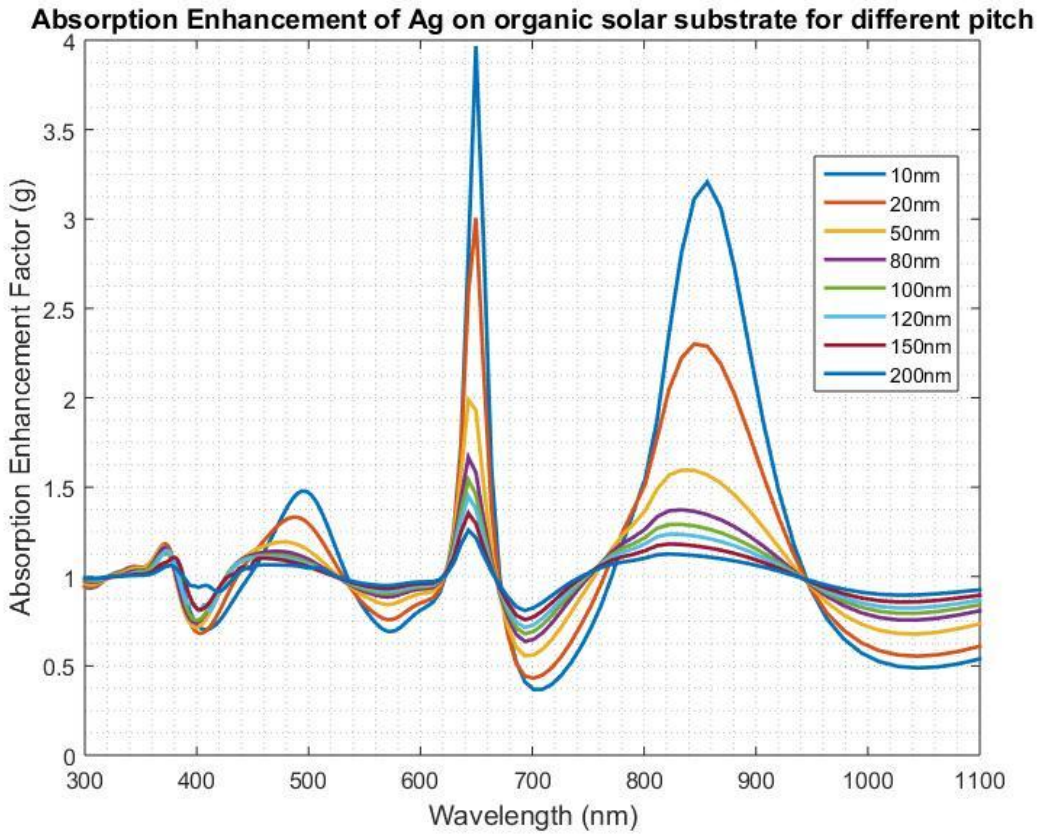

Figure 5. 5 Wavelength (nm)-resolved optical absorption enhancement for plasmonic solar cell with organic substrate (λ= 300nm-1100nm)

Unlike the other solar cells, OSCs showed some interesting result both in the individual absorption value and the total optical absorption enhancement values. From the Table 5.1, for 10nm pitch value between the nanoparticles the total absorption value is 166.39 which is the highest the OSC. On the other hand, the lowest value of total absorption was 151.62 for 200nm pitch. This means that there was a decreasing trend in values. If a closer look is given to the values in the table, it can be observed that although there was a decreasing trend but the values converged to a specific range of values (151.93 to 151.62). Further study on this OSC may give some more insights about the optical analysis.

The conclusion that can be drawn from these optical results is that the plasmonic nature of the nanoparticle involved in these different types of solar cells have an inherent effect on the light coupling efficiency of all the thin-film substrates considered for this study. It is quite evident that for each substrate, placing the plasmonic metal nanoparticles on top of the substrates increases the absorption of the incident radiation into the thin-film solar cells. Previous studies showed that using glass particles (non-plasmon supporting dielectric) were not very effective for increasing the optical absorption enhancement.

Of the four types of solar cells analyzed, the highest total optical absorption enhancement (192.69) was for silicon substrate regardless of the trend in their corresponding values. Both silicon and gallium arsenide showed the ring-bell curve trend i. e increasing up to a peak and then decreasing, in their values in relation to the pitch values. The reason for the decrease of the optical absorption enhancement values can be due to distance which affects the efficiency of the plasmonic coupling between the neighboring particles. Also, it is possible that the nanoparticles, increased scattering of the incident radiation by the Ag nanoparticles may be in a direction away from the Si and GaAs substrates thus leading to decreased absorption by the substrates.

For cadmium telluride-cadmium sulfide there was an increasing trend in the values with the pitch length but in the contrary, for OSC the trend was exactly opposite. OSC showed the least change in values compared to the others. It should also be noted that, if individual absorption value for particular pitch values are considered, OSC gave the highest value of nearly 4 for 10nm pitch.

The above results draw a correlation between the scattering of the plasmonic nanoparticles and optical absorption enhancement in the solar cell substrate and provide insights into how the silver (Ag) nanosphere can influence its plasmonic property to allow more incident radiation to be scattered/absorbed not only into the conventional silicon (Si) substrate but also other solar cells like - gallium arsenide (GaAs) , cadmium telluride-cadmium sulfide (CdTe-CdS) and even OSC (P3HT:PCBM) substrates. There is obviously further opportunities to study the optical properties of these solar cell substrates as well as other types of solar cells.

5.2 Short Circuit Current Density (J_{SC}) Analysis

It is expected that as the optical absorption within the solar-cell substrates increases, the electrical activity will also proportionally be increased [17]–[19]. However, this is not true in actual cases as electricity generation depends on a number of factors [20]. Hence to identify the extent to which the optical absorption enhancement of the substrates in the presence of silver (Ag) nanoparticles increases the electricity generation of the cells, the short circuit current density (JSC) of the cell for each configuration was calculated. While the solver FDTD Solutions is able to calculate an approximation for J_{SC}, it however provides an overestimation as its calculations are entirely based on the optical data generated, and does not take the minority carrier diffusion length, time and the extent of recombination for amorphous silicon into account. Hence, the J_{SC} data is generated using the DEVICE solver, as it considers all of the above in its calculations, and also takes the presence of the electrodes (contacts) into consideration. The generation files were imported and fed into the DEVICE solver. After that, the J_{SC} values were calculated using the model created and running the script command in the DEVICE solver.

As mentioned in the research methodology section, it was not possible to model electrical transport in organic materials using the CHARGE solver. So, the electrical calculation of the OSC could not be done. For this reason $J_{SC,}$ $V_{OC,}$ output power and fill factor of the OSC could not be calculated.

That being said, the short circuit current density (J_{SC}) for each solar cell except OSC with plasmonic nanostructures with varying the pitch values (10nm, 20nm, 50, 80nm, 100, 120, 150 and 200nm) is calculated for the entire spectrum, and illustrated in tabular form in Table 5.2. The highest values and highest increases in J_{SC} have been highlighted in bold font. Also, excel plot has been added for the Jsc results.

Table 5.2 J_{SC} of the Ag nanoparticle array based solar cells for the entire solar spectrum

	Ag(λ=400nm-1100nm)				Ag(λ=300nm-1100nm)	
	Si Substrate		GaAs Substrate		CdTe-CdS Substrate	
Pitch	J_{SC} (mA/cm^2)	% change	J_{SC} (mA/cm^2)	% change	J_{SC} (mA/cm^2)	% change
No Particle	7.646	0	19.854	0	23.95	0
10nm	4.098	-46.41	16.25	-18.15	10.1	-57.83
20nm	6.988	-8.61	22.831	14.99	16.3	-31.94
50nm	9.854	28.87	**26.383**	**32.88**	22.6	-5.64
80nm	**10.269**	**34.31**	25.907	30.49	24.15	0.84
100nm	10.218	33.64	25.363	27.75	24.81	3.59
120nm	10.09	31.96	24.841	25.12	25.5	6.47
150nm	9.862	28.97	24.161	21.69	26.79	11.86
200nm	9.503	24.29	23.288	17.3	**29.28**	**22.25**

To begin with, the results for the Si substrate shows a direct proportionality with the optical absorption enhancement analysis described earlier, with the pitch 80nm giving the highest J_{SC} value and decreasing as the pitch progressively increases above 80nm. For this peak value the increase in J_{SC} is almost 34% when compared to that of the bare silicon substrate. The same set of analyses was repeated for the gallium arsenide (GaAs) and cadmium telluride-cadmium sulfide (CdTe-CdS) substrates.

For gallium arsenide, it can be seen that the 50nm pitch value gives the highest J_{SC} value of 26.383 mA/cm^2 with around 33% increase compared to the bare gallium arsenide as shown in Table 5.2. Although for this case the pattern is not the same as its optical absorption enhancement analysis, the result of the Jsc calculations for the pitch size of 50nm and 80nm are comparable (33% and 30.5%, respectively). This could be due to the electrical properties of the GaAs solar cell. Thus, for the gallium arsenide solar cell the trend found with its optical absorption enhancement is also observed in the short circuit current density (J_{SC}) analysis but the correlation is not that strong between the two sets of data. So for both Si and GaAs, the J_{SC} results too, followed the same trend as the optical absorption data- increasing up to a certain peak and then decreasing.

Cadmium telluride-cadmium sulfide (CdTe-CdS) solar cells are one of the most efficient and popular solar cells in the solar cell industries. In this thesis, this fact is proven further by analyzing the electrical parameters. For the JSC calculation of CdTe-CdS solar cell, it follows the same trend like its optical absorption enhancement analysis-J_{SC} increasing with the increase of pitch length. The lowest value is 10.1 mA/cm^2 for 10nm pitch and the highest value 29.28 mA/cm^2 is for the 200nm pitch with 22.5% increase in the Jsc value when compared to bare substrate.

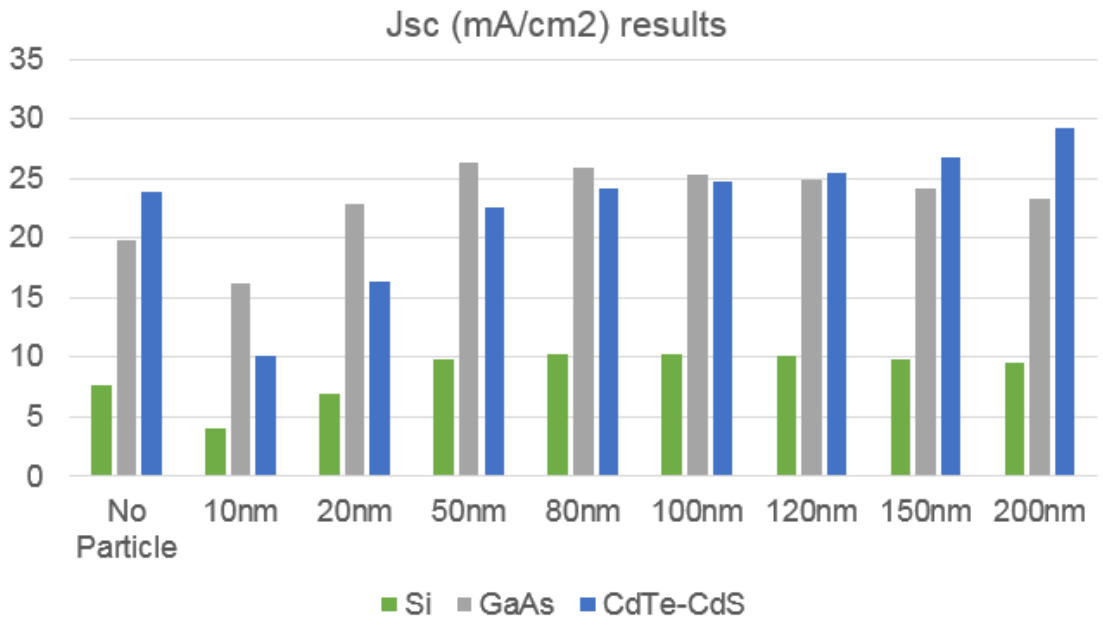

Figure 5. 6 Excel plot for the Jsc results

The above results provide insight into how the silver (Ag) nanosphere can influence its plasmonic property to allow more short circuit current generation for silicon (Si), gallium arsenide (GaAs) and cadmium telluride-cadmium sulfide (CdTe-CdS) solar cells. From the values of J_{SC} it can be inferred that CdTe-CdS solar cell has the highest short circuit current density- 29.28 mA/cm^2, meaning that it generates more electron in a given area of the substrate. The highest increase in percentage change was for silicon – 34.31% for 80nm pitch length. Overall, all three of the solar cells analyzed for J_{SC} calculation, showed promising results with CdTe-CdS being the winner in the race in terms of more current generation.

5.3 Open Circuit Voltage (V_{OC}) Analysis

Open circuit voltage indicates the maximum voltage available for the solar cells when the current in that particular solar cell is zero. The open circuit voltage (V_{OC}) for all the different configurations studied is calculated and shown in tabular form in Table 5.3. The highest values have been highlighted in bold font. The data from the table has been plotted and shown in Figure 5.7.

Table 5. 3 Open Circuit Voltage (V_{OC})

Pitch	Ag(λ=400nm-1100nm)				Ag(λ=300nm-1100nm)	
	Si Substrate		GaAs Substrate		CdTe-CdS Substrate	
	V_{OC}(mV)	% change	V_{OC}(mV)	% change	V_{OC}(mV)	% change
No Particle	400.13	0	815.62	0	934.2	0
10nm	400.23	0.03	800.61	-1.84	934.6	0.04
20nm	401.82	0.42	804.20	-1.4	940.7	0.7
50nm	401.82	0.42	809.61	-0.74	946.4	1.31
80nm	407.27	1.79	813.21	-0.29	**968.6**	**3.68**
100nm	410.91	2.69	815.62	0	949.7	1.66
120nm	414.55	3.6	818.02	0.29	950.8	1.78
150nm	420.13	5	821.62	0.74	952.8	1.99
200nm	**423.64**	**5.87**	**827.63**	**1.47**	956.3	2.37

For silicon substrate, the largest increase in V_{OC} can be seen for a pitch of 200nm which is a 5.87% increase. As the pitch lengths are increased, the V_{OC} values also increases proportionally. Additionally, for the GaAs substrate, the largest increase in V_{OC} is again found to be for the pitch of 200nm with a 1.47% increase. Same trend is followed by GaAs as well; as the pitch value increases V_{OC} increases too. From the table it can be observed that the V_{OC} values for the GaAs and CdTe-CdS substrates are significantly higher than that of the V_{OC} values of Si Substrate.

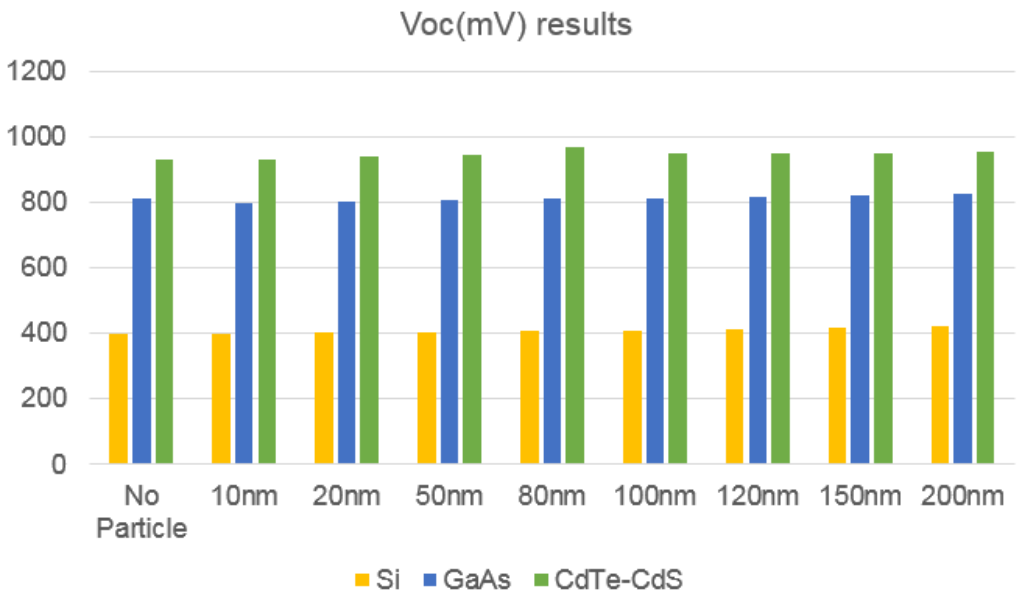

Figure 5. 7 Excel lot for the Voc results

Therefore, also in this case-V_{OC}, the results give an indication about how the silver (Ag) nanosphere can have an impact on the open circuit voltage of silicon (Si), gallium arsenide (GaAs) and cadmium telluride-cadmium sulfide (CdTe-CdS) solar cells through its plasmonic property similar to the short circuit current density.

5.4 Output Power (P) Analysis

Output power is one of the important electrical parameters for solar cells. Analyzing the power for the three substrates-silicon (Si), gallium arsenide (GaAs) and cadmium telluride-cadmium sulfide (CdTe-CdS) helped to shed some light as to which configuration is better working for practical usage. To this end, the output power of each solar cell (except the organic one) of different pitch lengths of silver nanoparticles were calculated by using the formula mentioned in the research methodology section. The results of the output power are shown in Table 5.4. The highest values have been highlighted in bold font. Also, the excel plot has also been added for ease of understanding.

Table 5. 4 Output Power

Pitch	Ag(λ=400nm-1100nm)				Ag(λ=300nm-1100nm)	
	Si Substrate		GaAs Substrate		CdTe-CdS Substrate	
	Power (nW)	% change	Power (nW)	% change	Power (nW)	% change
No Particle	0.122	0	0.648	0	0.895	0
10nm	0.066	-45.90	0.52	-19.75	0.378	-57.77
20nm	0.112	-8.20	0.734	13.27	0.613	-31.51
50nm	0.158	29.51	0.854	31.79	0.856	-4.36
80nm	0.167	36.89	**0.843**	**30.09**	0.936	4.58
100nm	**0.168**	**37.70**	0.827	27.62	0.942	5.25
120nm	0.167	36.89	0.813	25.46	0.970	8.38
150nm	0.166	36.07	0.794	22.53	1.021	14.08
200nm	0.161	31.97	0.771	18.98	**1.12**	**25.14**

For the Si substrate, the highest increase in power is seen for the pitch of 100nm which is almost 38% increase compared to the power of the Si substrate with no particle. As for the GaAs substrate, the power table shows that the highest power generated is for a pitch of 50nm which is approximately 32% increase compared to the bare GaAs substrate. For the Cdte-CdS substrate, the highest value is 1.12nW with an increase of 25.14%. This value is also the highest among all three substrates. Both silicon and gallium arsenide substrates have similar pattern like its optical absorption values. The output power values for both the substrates increases up to a peak and then decreases. Conversely, the output power values for

cadmium telluride-cadmium sulfide increases with the increase in pitch length.

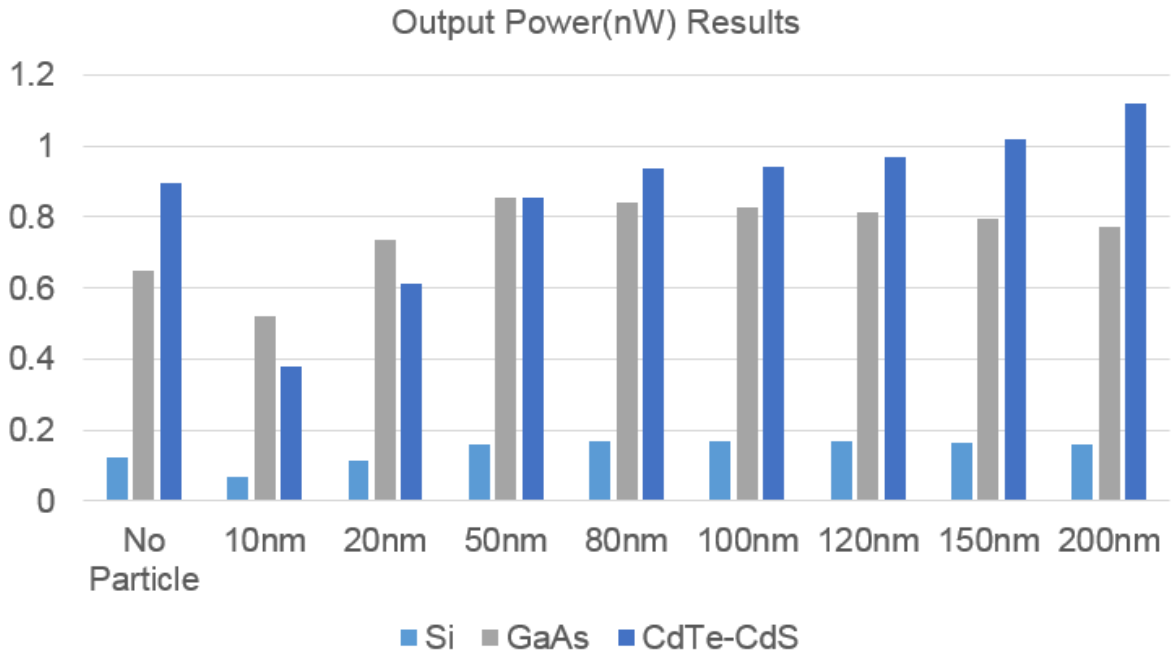

Figure 5. 8 Excel plot for the output power results

This observation suggests that even though for Si and GaAs substrates have the highest optical enhancement its electrical parameters are not higher when compared with CdTe-CdS substrate. The latter has the highest short circuit current density and open circuit voltage and eventually leading to the highest output power value. CdTe-CdS solar substrate had an increasing trend of optical absorption and for electrical analysis too, the trend is retained. Although the power is in nano-Watt, this thesis is concerned with the change in percentage increase of optoelectronic performance compared to the substrates when there are no plasmonic particles.

5.5 Efficiency Calculation

Efficiency was also calculated to further analyze the data. It should be noted that, only part of the solar cell was simulated for this thesis which in turn gave a low output power and efficiency. However, when a full solar panel will be integrated and simulated, the values will increase.

Table 5. 5 Efficiency Calculation

Pitch	Ag(λ=400nm-1100nm)				Ag(λ=300nm-1100nm)	
	Si Substrate		GaAs Substrate		CdTe-CdS Substrate	
	Efficiency (in %)	% change	Efficiency (in %)	% change	Efficiency (in %)	% change
No Particle	0.0031	0.0000	0.0162	0.0000	0.0224	0.0000
10nm	0.0017	-45.9016	0.0130	-19.7531	0.0095	-57.7654
20nm	0.0028	-8.1967	0.0184	13.2716	0.0153	-31.5084
50nm	0.0040	29.5082	0.0214	31.7901	0.0214	-4.3575
80nm	0.0042	36.8852	0.0211	30.0926	0.0234	4.5810
100nm	0.0042	37.7049	0.0207	27.6235	0.0236	5.2514
120nm	0.0042	36.8852	0.0203	25.4630	0.0243	8.3799
150nm	0.0042	36.0656	0.0199	22.5309	0.0255	14.0782
200nm	0.0040	31.9672	0.0193	18.9815	0.0280	25.1397

The efficiency values show the corresponding values of the solar cells as well their percentage change in the efficiency. The values resemble with the values of the output data as efficiency is related to the output and input power.

5.6 Fill Factor (FF) Analysis

Fill factor is a unit less ratio that measures the quality of the solar cell. It determines the maximum power from a solar cell. The FF is defined as the ratio of the maximum power from the solar cell to the product of V_{OC} and I_{SC}. So to determine the quality of the three substrates studied, the fill factor is calculated and the results are presented in Table 5.5. The highest values are highlighted in bold font.

Table 5. 6 Fill Factor

Pitch	Ag(λ=400nm-1100nm)				Ag(λ=300nm-1100nm)	
	Si Substrate		GaAs Substrate		CdTe-CdS Substrate	
	Fill Factor	% change	Fill Factor	% change	Fill Factor	% change
No Particle	0.770	0	0.8625	0	0.7952	0
10nm	0.770	0	0.8605	-0.232	0.7825	-1.6
20nm	0.771	0.091	0.861	-0.174	0.7896	-0.7
50nm	0.771	0.091	0.8617	-0.093	0.7993	0.52
80nm	0.773	0.364	0.8621	-0.046	0.8047	1.19
100nm	0.774	0.545	0.8625	0	0.8092	1.76
120nm	0.776	0.727	0.8628	0.034	0.813	2.24
150nm	0.778	0.987	0.8632	0.081	0.8184	2.92
200nm	**0.779**	**1.156**	**0.864**	**0.174**	**0.8237**	**3.58**

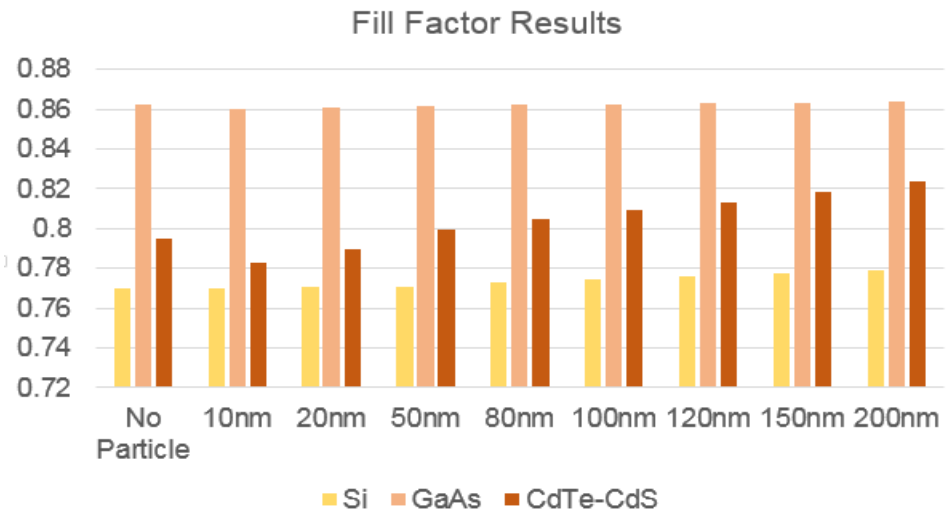

Figure 5. 9 Excel plot for the fill factor results

For the three substrates, the highest Fill Factor value is at pitch length of 200nm and shows an increasing pattern of FF as the pitch length increases. Among the three substrates, GaAs has the highest fill factor of 0.864 which supports the previously studied result of GaAs thin film cell [108]. The highest percentage increase was for CdTe-CdS cell- 3.58% change increase.

5.7 Optical Near-Field Enhancement Analysis

In order to observe and analyze the transmission of electric fields within the solar cells themselves, we opted to generate optical near-field enhancement images of the structures in question. This would allow to relate the optical and electrical enhancement of the cell due to the presence of the plasmonic metal nanoparticles with the interaction of the structure with the fields. The near field images are generated help understand the relationship between the distribution of the electric field within/around the nanoparticles and around/within the semiconductor substrates at the resonant wavelength of the nanoparticle [15]–[17].

These images were generated to understand the electromagnetic interaction of the nanoparticles and the semiconductor substrates. This allows the creation of a plausible connection between the physical parameters of the Ag nanoparticles and the improvement in electrical activity of the plasmonic solar cells [20]. The optical near-field images also show the amount of plasmonic coupling that occurs between neighboring metal nanoparticles.

First, the wavelength at which Ag nanoparticle displays plasmonic resonance for corresponding substrate is found at around λ=450nm. Twelve near field images were generated with different configurations for Si, GaAs, CdTe-CdS and organic substrates.

Figure 4.10 shows the near field images bare (a) silicon; (b) gallium arsenide; (c) cadmium telluride-cadmium sulfide; and (d) organic substrate. The near field images were generated at the respective resonance wavelength for each configuration as described previously [15]–[17]. The near field images with no particle show quite similar form for the four substrates.

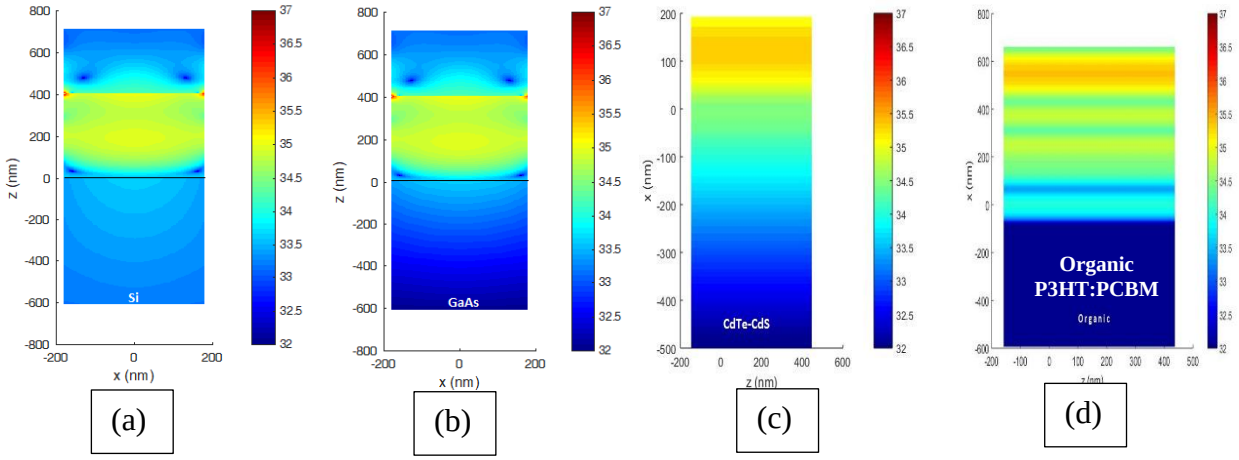

Figure 5. 10 Near-field images at λ=460nm of bare (with no particles) (a) Si, (b) GaAs, (c) CdTe-CdS and (d) organic (P3HT: PCBM) solar substrates

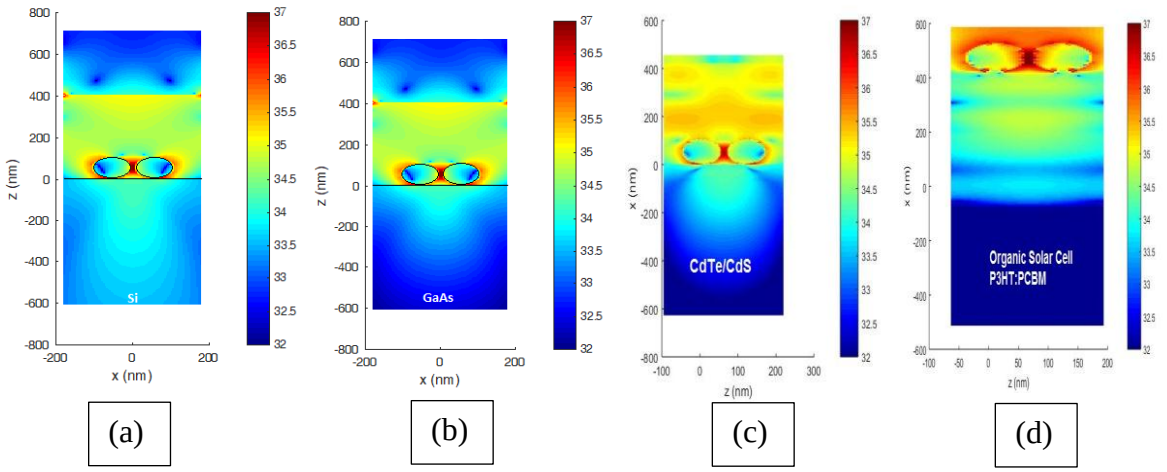

Figure 5. 11 Near-field raw(unenhanced) images at λ=460nm, Pitch length 10nm of Ag nanoparticles on top of (a) Si, (b) GaAs, (c) CdTe-CdS and (d) organic solar substrates

It should be noted that the optical near-field enhancement images shown in Figure 4.11(a-d) are presented in the base 10 logarithmic scale. As a result, areas in the image which are dark red in color and correspond to an enhancement value of "1" or greater corresponds to enhancement values of 10-fold or greater, which is quite significant.

From the optical near-field images it can be clearly seen that there is a variation in the interaction of the substrates due to the presence of Ag nanoparticles compared to the bare substrate. The significant enhancement in the optical near-fields occur in the region surrounding the metal nanoparticles due to the interaction with the incident electromagnetic radiation. These regions are shown in dark red in the optical near-field enhancement images. More importantly, it can be clearly seen that the enhanced electromagnetic fields penetrate quite significantly within the respective Si, GaAs, CdTe-CdS and organic substrates. Moreover, the enhancement images indicate a notable amount of the resonance scattering of the radiation caused by the nanoparticles is directed toward both inside the semiconductor substrates and also on top of the substrates.

The optical near-field images indicate a positive correlation between the interaction of the plasmonic nanoparticle with the incident light and the semiconductor substrate. Thus, the optical near-field images show that the use of plasmonic metal nanoparticles has an impact on the optical and electrical performance of thin-film solar cells (in this case Si, GaAs, CdTe-CdS and organic). It is difficult to make a direct correlation between the optical near-field enhancement images and that of the optical absorption enhancements and electrical activity

of the plasmonic solar cells (Jsc, Voc, power, fill factor) because the optical near-field images are obtained from only a plane that slices through the metal nanoparticles and the semiconductor substrate underneath (x-z plane). Nonetheless, from the near field images it can be clearly seen that both silicon and gallium arsenide have similar interaction as seen in the near filed images which resemble with their optical and electrical analysis as well. In the case of CdTe-CdS, the interaction is more significant as the pitch length between the particle increases. This is similar to its absorption and electrical values. For the OSC, there were significant interaction which can be observed in the picture.

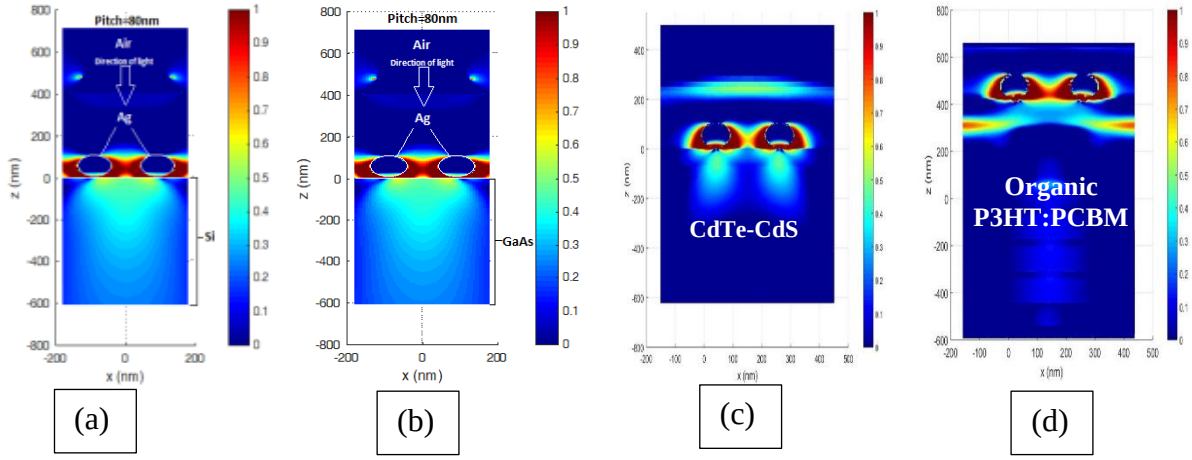

Figure 5. 13 Near-field enhancement images λ=460nm, Pitch length 80nm of Ag nanoparticles on top of (a) Si, (b) GaAs, (c) CdTe-CdS and (d) organic solar substrates

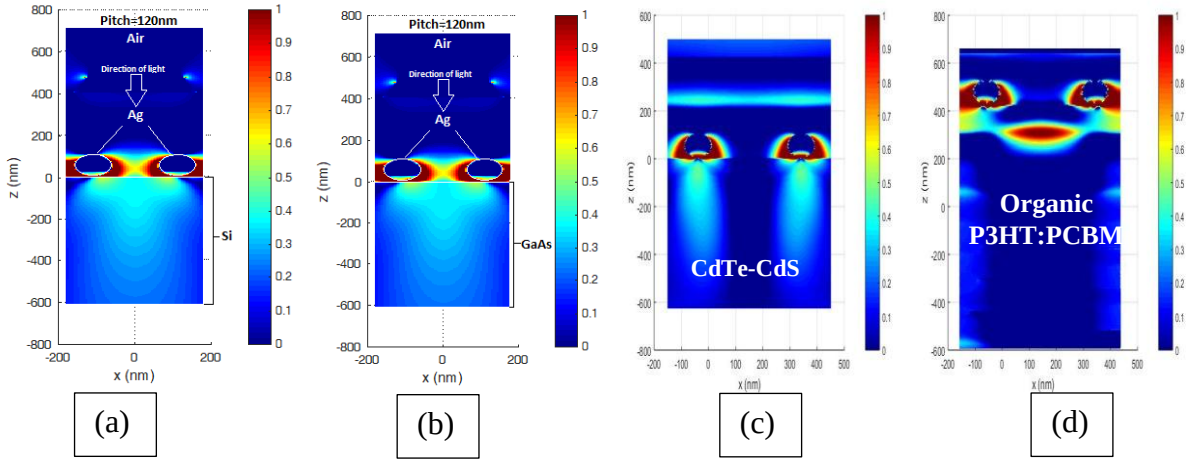

Figure 5. 12 Near-field enhancement images λ=460nm, Pitch length 120nm of Ag nanoparticles on top of (a) Si, (b) GaAs, (c) CdTe-CdS and (d) organic solar substrates

This is however, not the complete picture as the plasmonic interaction of the metal nanoparticles with each other, the semiconductor substrate and the incident light occurs in three dimensions (3D). Hence, the 2-D planar optical near-field images shown in Figure 5.10-5.13 can only provide a qualitative understanding and appreciation of such a complex optical interaction.

CHAPTER 6
CONCLUSION & FUTURE WORK

This comparative study investigates the effect of plasmonic metal nanoparticles to enhance the opto-electronic efficiency of three commonly used thin-film solar cells - silicon (Si), gallium arsenide (GaAs), cadmium telluride-cadmium sulfide (CdTe-CdS) and the emerging organic solar cell. Plasmonic metal nanoparticles were deposited on the thin-film substrates in a periodic array keeping the diameter of the nanoparticles fixed at 100 nm and the type of the material used was silver (Ag). By making the pitch length (side to side distance between the neighboring metallic nanoparticles) as the variable, the optical absorption enhancement of all four substrates and electrical parameters (except for the organic solar substrate) were investigated for the thin-film solar cells. The pitch lengths were: 10 nm, 20 nm, 50 nm, 80 nm, 100 nm, 120 nm, 150 nm and 200 nm.

Through extensive analysis it was found that both the silicon (Si) and the gallium arsenide (GaAs) substrate have the highest optical absorption enhancement (g) at 80 nm pitch and maintain a reverse parabolic (increasing up to a peak value from 0-80 nm pitch and then decreasing in value from 80-200nm pitch) trend for the different pitch values ranging from 10 nm to 200 nm. One reason behind this trend can be due to shading effect, where the closer the nanoparticles are, the more the incident light is prevented from reaching the semiconductor substrate underneath as it is being absorbed/scattered by the metal nanoparticles. For lower pitch values, the shading effect (a potential future scope for study) is more significant as more of the light incidents on the particles rather than the substrate itself. Also for lower pitch values, the neighboring nanoparticles are closer to one another and thus shades the semiconductor substrate underneath from the incident light. Additionally, for the higher pitch values the distance between the particles is not close enough to have significant plasmonic coupling between neighboring nanoparticles (which could then increase the light absorption into the substrate). It was also observed that the corresponding values of the optical absorption enhancement were similar for both the substrates.

In the case of CdTe-CdS and organic substrate it was found that it has an increasing trend of absorption value whereas the opposite was found for the organic solar substrate. For CdTe-CdS cell, the increasing trend maybe owing to its semiconductor properties. It is quite efficient nowadays in the solar cell industry. For the OSC, although there was a decreasing trend as the pitch length increase, the total absorption values were quite significant in their values.

From the optical data, the results indicate that the effect of plasmonic nanoparticles is not only valid for silicon solar cells but also for other common semiconductor substrates that are widely in use such as - gallium arsenide (GaAs) and cadmium telluride- cadmium sulfide solar cell. Also, the distance between the neighboring metal nanoparticles- pitch- has a significant effect on the contribution as well.

To determine the degree to which the optical absorption enhancement affects the electrical generation, the short circuit current density (Jsc) analysis along with three other electrical parameters- open circuit voltage (Voc), fill factor(FF) and power(P) - were studied. Similar to the optical absorption enhancement result, a significant rise (~35% increase for Si, ~33% increase for GaAs and ~22% increase for CdTe-CdS) in the Jsc was seen for Si, GaAs and CdTe-CdS at 80nm pitch, 50 nm pitch and 200nm pitch length, respectively. It is likely that increased number of electron-hole pairs are produced as more photons are absorbed by the substrate and /or scattered into the substrates, which leads to the generation of more short circuit current. However, as mentioned earlier, the shading effect can potentially cause less absorption of light into the substrate when the particles have a lower pitch (closer together); which in turn can cause the Jsc values to be smaller. For higher pitch values (larger inter-particle spacing), one reason why the Jsc values keeps declining (for Si and GaAs) can be due to the lower optical absorption enhancement. For these two substrates, the same trend of results is also seen in the values of Voc, power and fill factor. Adding to that, the increasing trend in Jsc for CdTe-CdS solar substrate may be due to its high absorption values. This solar substrate had the highest absorption, highest Jsc, highest power and highest fill factor all at 200nm pitch length. This means that optical absorption has a strong correlation with the electrical parameters of a solar cell.

Furthermore, to further clarify the results, the optical near-field enhancement images were analyzed which demonstrates the enhancement in the electromagnetic intensity due to the presence of plasmonic metal nanoparticles. The optical near-field images showed that a large

amount of enhancement occurs in the presence of the nanoparticles when compared to the bare substrates. It can be inferred that- although the degree of optical enhancement of the silicon(Si) based solar cells is larger compared to gallium arsenide (GaAs) substrate, the electrical activity(which includes the Jsc, Voc and power analysis) of the GaAs substrate is higher owing to its internal property (inherent physical nature). Same goes for the CdTe-CdS substrate, its electrical results are quite higher than that of the silicon and also gallium arsenide substrate. Moreover, this thesis shows the effect of plasmonic metal nanoparticles to increase the optical and electrical performance of thin-film solar cells is not limited to Si substrates but also can be extended to other commonly used semiconductor substrates (in this case gallium arsenide – GaAs cadmium telluride-cadmium sulfide- CdTe-CdS).

To conclude, it must be noted that, further analysis of the electrical activity such as the electrical efficiency needs to be done as well as the effect of shading (as mentioned earlier) of the plasmonic metal nanoparticles on the optical and electrical enhancement of the substrates' performance needs to be thoroughly studied. Adding to that, the use of different types of OSCs can also be used for further analysis in this field in order to establish a more robust understanding of these relationships. Future work shall include the modeling, calculations and analysis of these additional parameters mentioned to get a clearer understanding on how the various properties of the plasmonic metal nanoparticles can have an impact in improving the efficiency of thin-film solar cells. Future work also includes the hardware implementation of the plasmonic solar cells to prove the results of the simulation.

These results indicate that for certain high-end applications where the initial costs of installation of the solar cells is not a limiting factor, plasmonic thin-film solar cells can be effective platforms to give high-quality performance. Also, in other regular applications after doing the cost-benefit analysis of certain types of solar cells, application of plasmonic structure onto these solar cells can be used as a suitable alternative to generate the required output electrical power at economically feasible costs compared to the conventional thin film cells.

REFERENCES

[1] Worldometers.info, "World Population." [Online]. Available: https://www.worldometers.info/world-population/. [Accessed: 20-Jul-2019].

[2] Wikipedia contributors, "World energy consumption," *Wikipedia, The Free Encyclopedia.* [Online]. Available: https://en.wikipedia.org/w/index.php?title=World_energy_consumption&oldid=905349276. [Accessed: 18-Jul-2019].

[3] N. Martin Chivelet, J. Carlos Gutiérrez, M. Alonso Abella, F. Chenlo, and J. Cuenca, "Building Retrofit with Photovoltaics: Construction and Performance of a BIPV Ventilated Façade," *Energies*, vol. 11, Jul. 2018.

[4] J. Nelson, *The Physics of Solar Cells*. PUBLISHED BY IMPERIAL COLLEGE PRESS AND DISTRIBUTED BY WORLD SCIENTIFIC PUBLISHING CO., 2003.

[5] P. Würfel and U. Würfel, *Physics of solar cells: From basic principles to advanced concepts, second updated and expanded edition*. 2009.

[6] A. Riverola, A. Vossier, and D. Chemisana, "Fundamentals of solar cells," *Nanomater. Sol. Cell Appl.*, pp. 3–33, Jan. 2019.

[7] M. A. Green, "Lambertian light trapping in textured solar cells and light-emitting diodes: analytical solutions," *Prog. Photovoltaics Res. Appl.*, vol. 10, no. 4, pp. 235–241, Jun. 2002.

[8] J. Müller, B. Rech, J. Springer, and M. Vanecek, "TCO and light trapping in silicon thin film solar cells," *Sol. Energy*, 2004.

[9] J. Meier *et al.*, *Microcrystalline Silicon and the Impact on Micromorph Tandem Solar Cells*, vol. 74. 2002.

[10] W. L. Barnes, A. Dereux, and T. W. Ebbesen, "Surface plasmon subwavelength optics," *Nature*, vol. 424, no. 6950, pp. 824–830, 2003.

[11] U. Eicker, E. Demir, and D. Gürlich, "Strategies for cost efficient refurbishment and solar energy integration in European Case Study buildings," *Energy Build.*, 2015.

[12] P. Würfel, *Physics of Solar Cells: From Principles to New Concepts*. 2007.

[13] M. C. Beard, J. M. Luther, and A. J. Nozik, "The promise and challenge of nanostructured solar cells," *Nat. Nanotechnol.*, vol. 9, p. 951, Dec. 2014.

[14] T. Soga, *Nanostructured Materials for Solar Energy Conversion*. 2006.

[15] S. A. Choudhury, "The Promise and Challenges of Enhancing Solar Cell Efficiency

Using Patterned Nanostructures," in *1st International Conference on Advanced Information and Communication Technology*, 2016.

[16] S. A. Choudhury and M. H. Chowdhury, "Optimizing the parameters of plasmonic metal nanoparticles to maximize the energy conversion efficiency of thin-film solar cells," *2016 3rd Int. Conf. Electr. Eng. Inf. Commun. Technol. iCEEiCT 2016*, 2017.

[17] S. A. Choudhury and M. H. Chowdhury, "Use of plasmonic metal nanoparticles to increase the light absorption efficiency of thin-film solar cells," in *2016 IEEE International Conference on Sustainable Energy Technologies (ICSET)*, 2016, pp. 196–201.

[18] S. A. Choudhury, M. S. Munir, N. Nawshin, and M. H. Chowdhury, "Effect of varying the row and column size of periodic arrays of plasmonic nanoparticles on the energy conversion efficiency of thin-film solar cells," in *ECCE 2017 - International Conference on Electrical, Computer and Communication Engineering*, 2017, pp. 44–49.

[19] S. A. Choudhury, N. Nawshin, and M. H. Chowdhury, "Influence of particle shape on the efficacy of plasmonic metal nanoparticles to enhance the energy conversion efficiency of thin-film solar cells," in *IEEE Region 10 Annual International Conference, Proceedings/TENCON*, 2017, vol. 2017-Decem, pp. 2393–2398.

[20] S. A. Choudhury, R. A. Rifat, F. Fairooz, W. Mahdi, and M. H. Chowdhury, "On the possibility of using plasmonic metal nanoparticles embedded within the silicon substrate to enhance the energy conversion efficiency of silicon thin-film solar cells," in *5th IEEE Region 10 Humanitarian Technology Conference 2017, R10-HTC 2017*, 2018, vol. 2018-Janua, pp. 584–589.

[21] R. A. Rifat, N. Ibn Ashraf, S. A. Chowdhury, and M. H. Chowdhury, "The Use of Plasmonic Metal Nanoparticles to Enhance the Efficiency of Thin-Film Silicon (Si) and Gallium Arsenide (GaAs) Solar Cells - A Comparative Study," in *Proceedings of the Conference on the Industrial and Commercial Use of Energy, ICUE*, 2019, vol. 2018-Octob.

[22] M. M. Shaky, N. I. Ashraf, R. A. Rifat, and M. H. Chowdhury, "Use of Hybrid Bow-Tie Based Plasmonic Nanostructures to Enhance the Opto-Electronic Efficiency of Thin-Film Solar Cells," in *2nd International Conference on Electrical, Computer and Communication Engineering, ECCE 2019*, 2019, pp. 7–9.

[23] F. Fairooz, S. A. Choudhury, N. I. Ashraf, W. Mahdi, and M. H. Chowdhury, "Use of Bimetallic Plasmonic Nanoparticle Complexes for Enhancing Thin-Film Solar Cell

Efficiency," in *2nd International Conference on Electrical, Computer and Communication Engineering, ECCE 2019*, 2019.

[24] N. I. Ashraf, "Use of Plasmonic Metal Core-Dielectric Shell Composite Nanoparticles Embedded within the Absorbing Layer to Enhance the Efficiency of Thin- Film Solar Cells," in *IEEE Region 10 Symposium, TENSYMP 2019*, 2019.

[25] D. M. Schaadt, B. Feng, and E. T. Yu, "Enhanced semiconductor optical absorption via surface plasmon excitation in metal nanoparticles," *Appl. Phys. Lett.*, 2005.

[26] S. Pillai, K. R. Catchpole, T. Trupke, and M. A. Green, "Surface plasmon enhanced silicon solar cells," in *Journal of Applied Physics*, 2007.

[27] R. A. Pala, J. White, E. Barnard, J. Liu, and M. L. Brongersma, "Design of plasmonic thin-film solar cells with broadband absorption enhancements," *Adv. Mater.*, 2009.

[28] D. Derkacs, S. H. Lim, P. Matheu, W. Mar, and E. T. Yu, "Improved performance of amorphous silicon solar cells via scattering from surface plasmon polaritons in nearby metallic nanoparticles," *Appl. Phys. Lett.*, 2006.

[29] X. Chen *et al.*, "Broadband enhancement in thin-film amorphous silicon solar cells enabled by nucleated silver nanoparticles," *Nano Lett.*, 2012.

[30] Z.-Y. Yang and K.-P. Chen, "Effective absorption enhancement in dielectric thin-films with embedded paired-strips gold nanoantennas," *Opt. Express*, 2014.

[31] Y. Zhang, B. Jia, and M. Gu, "Biomimetic and plasmonic hybrid light trapping for highly efficient ultrathin crystalline silicon solar cells," *Opt. Express*, vol. 24, no. 6, pp. A506--A514, Mar. 2016.

[32] A. Kumar, "Predicting efficiency of solar cells based on transparent conducting electrodes," *J. Appl. Phys.*, vol. 121, no. 1, 2017.

[33] W. Shockley and H. J. Queisser, "Detailed balance limit of efficiency of p-n junction solar cells," *J. Appl. Phys.*, vol. 32, no. 3, pp. 510–519, 1961.

[34] R. A. Kerr, "Sun's Role in Warming Is Discounted," *Science (80-.).*, vol. 268, 1995.

[35] J. Hansen, "Global temperature change," *Proc. Natl. Acad. Sci.*, vol. 103, pp. 14288–14293, 2006.

[36] A. W. Blakers, M. A. Green, T. Leo, H. Outhred, and B. Robins, *The Role of Photovoltaics in Reducing Greenhouse Gas Emissions*. Canberra: Australian Government Publishing Service, 1991.

[37] S.G.Bowden; C.B.Honsberg, "Photovoltaics Education Website," 2019. [Online]. Available: https://www.pveducation.org.

[38] M. Planck, "Distribution of energy in the spectrum," *Ann. Phys.*, vol. 4, pp. 553–563,

1901.

[39] A. Einstein, “Generation and transformation of light,” *Ann. Phys.*, vol. 17, 1905.

[40] G. N. Lewis, *A Revision of the Fundamental Laws of Matter and Energy*. Taylor & Francis, 1908.

[41] M. M. Capria, *Physics Before and After Einstein*. IOS Press, 2005.

[42] A. Einstein and L. Infeld, *The evolution of physics: the growth of ideas from early concepts to relativity and quanta*. Simon and Schuster, 1938.

[43] J. A. CROWTHER, “The Evolution of Physics,” *Nature*, vol. 141, no. 3577, pp. 891–892, 1938.

[44] A. Einstein, “Über einen die Erzeugung und Verwandlung des Lichtes betreffenden heuristischen Gesichtspunkt,” *Ann. Phys.*, vol. 322, no. 6, pp. 132–148, Jan. 1905.

[45] David Herring, “Power to the People - NASA Earth Observatory,” *The Earth Observatory*, 2001. [Online]. Available: https://earthobservatory.nasa.gov/features/RenewableEnergy.

[46] F. Kasten and A. T. Young, “Revised optical air mass tables and approximation formula,” *Appl. Opt.*, vol. 28, no. 22, p. 4735, 1989.

[47] R. P. Feynman, R. B. Leighton, and M. Sands, *The Feynman Lectures on Physics, Vol. II: The New Millennium Edition: Mainly Electromagnetism and Matter*. Basic Books, 2011.

[48] I. Langmuir, “THE ARRANGEMENT OF ELECTRONS IN ATOMS AND MOLECULES.,” *J. Am. Chem. Soc.*, vol. 41, no. 6, pp. 868–934, Jun. 1919.

[49] G. N. Lewis, “THE ATOM AND THE MOLECULE.,” *J. Am. Chem. Soc.*, vol. 38, no. 4, pp. 762–785, Apr. 1916.

[50] P. Atkins and J. de Paula, *Atkins’ Physical Chemistry*. OUP Oxford, 2010.

[51] B. G. Streetman and S. Banerjee, *Solid State Electronic Devices*. Pearson Prentice Hall, 2006.

[52] D. Neamen, *Semiconductor Physics And Devices*. McGraw-Hill Education, 2003.

[53] A. Augusto, S. Y. Herasimenka, R. R. King, S. G. Bowden, and C. Honsberg, “Analysis of the recombination mechanisms of a silicon solar cell with low bandgap-voltage offset,” *J. Appl. Phys.*, 2017.

[54] R. A. Sinton and A. Cuevas, “Contactless determination of current-voltage characteristics and minority-carrier lifetimes in semiconductors from quasi-steady-state photoconductance data,” *Appl. Phys. Lett.*, 1996.

[55] F. A. Lindholm, J. G. Fossum, and E. L. Burgess, “Application of the superposition

principle to solar-cell analysis," *IEEE Trans. Electron Devices*, vol. 26, no. 3, p. 165{\textendash}171, 1979.

[56] Daniel Burgess, "Thin-film solar cell," *Encyclopædia Britannica, inc.* .

[57] Adams and R. E. Day, "The Action of Light on Selenium," *Proc. R. Soc. London*, vol. A25, 1877.

[58] Fritts, "On a New Form of Selenium Photocell," *Am. J. Sci.*, vol. 26, 1883.

[59] L. O. Grondahl, "The Copper-Cuprous-Oxide Rectifier and Photoelectric Cell," *Rev. Mod. Phys.*, vol. 5, no. 2, pp. 141–168, 1933.

[60] Nix and A. W. Treptwo, "A Thallous Sulphide Photo EMF Cell," *J. Opt. Soc. Am.*, vol. 29, 1939.

[61] D. M. Chapin, C. S. Fuller, and G. L. Pearson, "A new silicon p-n junction photocell for converting solar radiation into electrical power [3]," *Journal of Applied Physics*. 1954.

[62] Kingsbury and R. S. Ohl, "Photoelectric Properties of Tonically Bombarded Silicon," *Bell Syst. Tech. J.*, vol. 31, 1952.

[63] Ohl, "Light-Sensitive Electric Device," *U.S. Pat.*, vol. 2, 1941.

[64] M. A. Green *et al.*, "Solar cell efficiency tables (Version 53)," *Prog. Photovoltaics Res. Appl.*, vol. 27, no. 1, pp. 3–12, Jan. 2019.

[65] J. M. Ball *et al.*, "Optical properties and limiting photocurrent of thin-film perovskite solar cells," *Energy Environ. Sci.*, vol. 8, no. 2, pp. 602–609, 2015.

[66] S. H. Park, I. Shin, K. H. Kim, R. Street, A. Roy, and A. J. Heeger, "Tandem solar cells made from amorphous silicon and polymer bulk heterojunction sub-cells," *Adv. Mater.*, vol. 27, no. 2, pp. 298–302, 2015.

[67] M. Askari, V. Mirzaei Mahmoud Abadi, and M. Mirhabibi, "Types of Solar Cells and Application," *Am. J. Opt. Photonics*, vol. 3, p. 2015, Aug. 2015.

[68] W. Xufeng, M. Rezwan Khan, J. Gray, M. Ashraful Alam, and M. . Lundstrom, "Design of GaAs Solar Cells Operating Close to the Shockley–Queisser Limit," *Photovoltaics, IEEE J.*, vol. 3, pp. 737–744, Apr. 2013.

[69] Lars Engvik, "Photovoltaic energy generation," *energyfaculty.com*. [Online]. Available: https://energyfaculty.com/photovoltaic-energy-generation/.

[70] R. Hulstrom, R. Bird, and C. Riordan, "Spectral solar irradiance data sets for selected terrestrial conditions," *Sol. Cells*, 1985.

[71] S. Pillai and M. Green, "Plasmonics for photovoltaic applications," *Sol. Energy Mater. Sol. Cells*, vol. 94, pp. 1481–1486, 2010.

[72] Z. Zhou, S. Pang, Z. Liu, H. Xu, and G. Cui, “Interface engineering for high-performance perovskite hybrid solar cells,” *Journal of Materials Chemistry A*. 2015.

[73] J. P. Kottmann, O. J. F. Martin, D. R. Smith, and S. Schultz, “Spectral response of plasmon resonant nanoparticles with a non-regular shape,” *Opt. Express*, 2000.

[74] J. Li, S. K. Cushing, F. Meng, T. R. Senty, A. D. Bristow, and N. Wu, “Plasmon-induced resonance energy transfer for solar energy conversion,” *Nat. Photonics*, 2015.

[75] S. H. Lim, W. Mar, P. Matheu, D. Derkacs, and E. T. Yu, “Photocurrent spectroscopy of optical absorption enhancement in silicon photodiodes via scattering from surface plasmon polaritons in gold nanoparticles,” *J. Appl. Phys.*, 2007.

[76] M. S. Tame, K. R. McEnery, Ş. K. Özdemir, J. Lee, S. A. Maier, and M. S. Kim, “Quantum plasmonics,” *Nat. Phys.*, vol. 9, p. 329, Jun. 2013.

[77] K. L. Kelly, E. Coronado, L. L. Zhao, and G. C. Schatz, “The optical properties of metal nanoparticles: The influence of size, shape, and dielectric environment,” *J. Phys. Chem. B*, 2003.

[78] M. A. Green and S. Pillai, “Harnessing plasmonics for solar cells,” *Nature Photonics*. 2012.

[79] J.-D. Chen *et al.*, “Single-junction polymer solar cells exceeding 10% power conversion efficiency.,” *Adv. Mater.*, vol. 27, no. 6, pp. 1035–41, Feb. 2015.

[80] T. Kawawaki *et al.*, “Efficiency Enhancement of PbS Quantum Dot/ZnO Nanowire Bulk-Heterojunction Solar Cells by Plasmonic Silver Nanocubes,” *ACS Nano*, vol. 9, no. 4, pp. 4165–4172, Apr. 2015.

[81] J. D. Winans, C. Hungerford, K. Shome, L. J. Rothberg, and P. M. Fauchet, “Plasmonic effects in ultrathin amorphous silicon solar cells: performance improvements with Ag nanoparticles on the front, the back, and both,” *Opt. Express*, vol. 23, no. 3, pp. A92--A105, Feb. 2015.

[82] Wikimedia Commons contributors, “File:Sketch of surface plasmon.png,” *Wikimedia Commons, the free media repository*. [Online]. Available: https://commons.wikimedia.org/w/index.php?title=File:Sketch_of_surface_plasmon.png&oldid=234409283. [Accessed: 06-Aug-2019].

[83] N. P. Hylton *et al.*, “Loss mitigation in plasmonic solar cells: Aluminium nanoparticles for broadband photocurrent enhancements in gaas photodiodes,” *Sci. Rep.*, 2013.

[84] M. J. Mendes *et al.*, “Broadband light trapping in thin film solar cells with self-organized plasmonic nanocolloids,” *Nanotechnology*, 2015.

[85] C. F. Bohren and D. R. Huffman, *Absorption and scattering of light by small particles*.

Wiley, 2004.

[86] M. Green, K. Emery, Y. Hishikawa, W. Warta, and E. Dunlop, "Solar cell efficiency tables (Version 45)," *Prog. Photovoltaics Res. Appl.*, vol. 22, p. 1, 2014.

[87] M. D. Archer and M. A. Green, *Clean Electricity from Photovoltaics*, 2nd ed. IMPERIAL COLLEGE PRESS, 2014.

[88] X. Li, W. C. H. Choy, H. Lu, W. E. I. Sha, and A. H. P. Ho, "Efficiency enhancement of organic solar cells by using shape-dependent broadband plasmonic absorption in metallic nanoparticles," *Adv. Funct. Mater.*, 2013.

[89] N. Zhou, V. Lopez, Q. Wang, P. Lakshminarayana, I. Pastoriza-Santos, and Q.-H. Xu, "Plasmon-enhanced light harvesting: Applications in enhanced photocatalysis, photodynamic therapy and photovoltaics," *RSC Adv.*, vol. 5, pp. 29076–29097, 2015.

[90] E. T. Yu, D. Derkacs, P. Matheu, and D. M. Schaadt, "Plasmonic nanoparticle scattering for enhanced performance of photovoltaic and photodetector devices," in *Plasmonics: Nanoimaging, Nanofabrication, and Their Applications IV*, 2008.

[91] J. E. Roy, "Modeling Lumped Sources in the Finite-Difference Time-Domain Method of the Scattered-Field Formulation," *IEEE Trans. Microw. Theory Tech.*, vol. 64, no. 8, pp. 2383–2391, 2016.

[92] K. Yee, "Numerical solution of initial boundary value problems involving maxwell's equations in isotropic media," *IEEE Trans. Antennas Propag.*, vol. 14, no. 3, pp. 302–307, 1966.

[93] J. VonNeumann and R. D. Richtmyer, "A Method for the Numerical Calculation of Hydrodynamic Shocks," *J. Appl. Phys.*, vol. 21, no. 3, pp. 232–237, Mar. 1950.

[94] A. Taflove, "Application of the Finite-Difference Time-Domain Method to Sinusoidal Steady-State Electromagnetic-Penetration Problems," *IEEE Trans. Electromagn. Compat.*, vol. EMC-22, no. 3, pp. 191–202, 1980.

[95] A. Taflove and S. C. Hagness, *Computational Electrodynamics: The Finite-Difference Time-Domain Method, 3rd edition.*, vol. 2062. 2005.

[96] Lumerical Inc., "FDTD." [Online]. Available: https://kb.lumerical.com/solvers_finite_difference_time_domain.html.

[97] EASTERN MEDITERRANEAN UNIVERSITY OPEN COURSEWARES, "FINITE DIFFERENCE TIME DOMAIN METHOD (FDTD)." [Online]. Available: http://opencourses.emu.edu.tr/.

[98] A. Taflove and M. E. Brodwin, "Numerical Solution of Steady-State Electromagnetic Scattering Problems Using the Time-Dependent Maxwell's Equations," *IEEE Trans.*

Microw. Theory Tech., vol. 23, no. 8, pp. 623–630, 1975.

[99] University of Delaware, "Computational Electromagnetics." [Online]. Available: https://www.eecis.udel.edu/.../ELEG867_FINITE_DIFFERENCE_ LECTURES.ppt.

[100] D. Gallagher and P. Design, "Photonic CAD matures."

[101] J.-P. Berenger, "A perfectly matched layer for the absorption of electromagnetic waves," *J. Comput. Phys.*, vol. 114, no. 2, pp. 185–200, 1994.

[102] S. D. Gedney, "An anisotropic perfectly matched layer-absorbing medium for the truncation of FDTD lattices," *IEEE Trans. Antennas Propag.*, vol. 44, no. 12, pp. 1630–1639, 1996.

[103] Lumerical Inc., "FDTD Solutions: 3D Electromagnetic Simulator." 2019.

[104] Lumerical Inc., "DEVICE- CHARGE Solver: 3D Charge Transport Simulator." 2019.

[105] M. N. Polyanskiy, "Refractive index database," 2019.

[106] C. Lundgren, R. Lopez, J. Redwing, and K. Melde, "FDTD modeling of solar energy absorption in silicon branched nanowires," *Opt. Express*, vol. 21, no. S3, pp. A392--A400, May 2013.

[107] "Tinkercad." 2010.

[108] M. A. Green, E. D. Dunlop, D. H. Levi, J. Hohl-Ebinger, M. Yoshita, and A. W. Y. Ho-Baillie, "Solar cell efficiency tables (version 54)," *Prog. Photovoltaics Res. Appl.*, vol. 27, no. 7, pp. 565–575, 2019.